Institute of Aircraft Design
Lehrstuhl für Luftfahrtsysteme

Synthesis of Compliant Mechanisms for Morphing Wings with Nonlinear Topology Optimization

Master Thesis

Submitted in partial fulfillment of the requirements for the degree
M.Sc. Mechanical Engineering at the Department of Mechanical Engineering
of the Technical University of Munich.

Supervised by Prof. Dr.-Ing. Mirko Hornung
Dipl.-Ing. Johannes Achleitner
Institute of Aircraft Design

Submitted by Joseph Reinisch
Student ID: 3642448

Submitted on December 14, 2018

Sequential number LS-MA 18/20

Abstract

In this work, synthesis of compliant mechanisms for a variable-geometry forward section wing concept based on geometric nonlinear FEM is presented. The path-generation objective function formulation for topology optimization of compliant mechanisms is implemented in a custom optimization code. Moreover, the code is extended with other existing topology optimization methods, such as a multiresolution topology optimization scheme and partial differential equation based filtering techniques. The implementation is tested with generic example problems. A new stacked compliant mechanism rib concept is introduced for the morphing wing application. For this concept, compliant mechanisms are designed under consideration of stress constraints.

Keywords: Topology optimization, Compliant mechanisms, Path generation, MMA, Geometric nonlinear FEM, Stress constraints, Morphing wing

Contents

List of Figures

List of Tables

Nomenclature

Acronyms

DOF	Degree of freedom
FE	Finite element
FEA	Finite element analysis
FEM	Finite element method
MMA	Method of moving asymptotes
MTOP	Multiresolution topology optimization scheme
PDE	Partial differential equation
PEEK	Polyether ether ketone

Greek Symbols

α	Load case weighting factor
β	Curve parameter of the Heaviside function approximation the for projection methods
β_1	Curve parameter of the Heaviside step approximation in the energy interpolation scheme
β_{start}	Initial β value for the application of external design variable move limits
$\boldsymbol{\sigma}_e$	Element stress vector
η	Threshold value of the Heaviside function approximation for the projection methods
Γ	Boundary of the design space
γ_e	Energy interpolation parameter
λ	Load incrementation parameter
ν	Poisson ratio
Ω	Design space
$\overline{\tilde{\rho}}$	Filtered and projected density
Φ	Path-generation objective function
ϕ	General strain energy density
$\boldsymbol{\lambda}_{adj}$	Arbitrary adjoint vector
$\boldsymbol{\sigma}_{PK,e}$	Vector of the element second Piola-Kirchhoff stresses
Ψ	Continuous representation of the density
ψ	Arbitrary function
ρ	Density
ρ_1	Threshold parameter of the Heaviside step approximation for the energy interpolation scheme

σ^* ..... Stress constraint limit value
σ_{PN} ..... p-norm stress
σ_{sum} ..... Intermediate solution stresses of the p-norm
σ_{vm} ..... Von Mises stress
τ ..... β continuation scheme control parameter
$\tilde{\rho}$ ..... Filtered density
$\tilde{\sigma}_{PN}$ ..... Normalized p-norm stress

Indices

0 ..... Basis value or base material property value
adj ..... Adjoint
e ..... Element numbering index
F ..... Filter
gp ..... Gauss point numbering index
i ..... Load case numbering index
in ..... Input
j ..... General counting index
k ..... General counting index
m ..... Precision point numbering index
max ..... Maximum value
min ..... Minimum value
N ..... Nodal
out ..... Output
$phys$ ..... Index denoting physical properties
s ..... Solid / Stress
$start$ ..... Start value
v ..... Void / Volume

Latin Symbols

$\boldsymbol{B}_L$ ..... FE operator matrix
$\boldsymbol{C}_{VK}$ ..... St. Venant-Kirchhoff constitutive matrix
$\boldsymbol{F}$ ..... Global external load vector
$\boldsymbol{f}$ ..... Local external load vector
$\boldsymbol{K}$ ..... Global stiffness matrix
$\boldsymbol{K}_T$ ..... Tangent stiffness matrix
$\boldsymbol{K}_{e0}$ ..... Element stiffness matrix for normalized Young's modulus ($E = 1$)
$\boldsymbol{K}_e$ ..... Element stiffness matrix
$\boldsymbol{L}$ ..... Objective function definition vector

$\boldsymbol{n}$	Normal vector
$\boldsymbol{R}$	Residual vector
$\boldsymbol{S}$	General set of allowable designs
$\boldsymbol{T}$	Transformation matrix
$\boldsymbol{U}$	Global displacement vector
$\boldsymbol{u}$	Local displacement vector
$\boldsymbol{V}$	Operator matrix for von Mises stress calculation
$\boldsymbol{x}$	General design variable vector
$\hat{U}_c$	Prescribed displacement step
$\overline{\boldsymbol{F}}$	Matrix formulation of the deformation gradient
c	Stress normalization parameter
C_L	Coefficient of lift
C_p	Pressure distribution coefficient
$chord$	Chord length
E	Young's modulus
f	Control function for displacement-controlled nonlinear FEA
g	General inequality constraint
h	General equality constraint
H_{ei}	Weighting factors for density filter
$iter$	Number of iterations
k	Penalty term for the SIMP approach
$offset$	Offset parameter of the Heaviside step approximation for the energy interpolation scheme
p	Stress p-norm parameter
q	Stress relaxation parameter
r	Filter radius
Re	Reynolds number
T	Thickness
V	Volume
v	Element volume
V_Ω	Volume of the design space
v_{frac}	Volume fraction constraint threshold
z	General objective function

1 Motivation

In aircraft design, rigid airfoils must meet a vast variety of different and often conflicting requirements. Profiles for example need to provide high amounts of lift during takeoff, landing and climb, whereas during cruise flight only relatively low lift levels are required. To adapt airfoils to these different operational regimes, many existing forms of wings with moving devices can be used. Most of them change the profiles camber by varying the airfoil's front or rear section geometry. As a result, the coefficients of lift and drag can be changed. In high-performance sailplane design, trailing edge flaps are the state of the art solution. This design is well developed and only marginal further improvement is possible.

Research by Wiessmeier (2011) at TUM shows high potential in a novel sailplane design concept, combining trailing edge flaps with an adaptive droop nose. With this design around 20% higher coefficients of lift appear to be feasible, allowing a higher aspect ratio wing and higher possible wing loading. As a result not only the glide ratios can be increased significantly, but also the speed of best glide.

Figure 1.1: Laminar airfoil with droop nose and trailing edge flap (Wiessmeier 2011)

Figure 1.1 illustrates Wiessmeier's concept, in which the dashed line represents the morphed high lift slow-flight airfoil. The solid line represents the high-speed profile. Shape morphing allows to choose between these two optimized airfoil geometries in flight.

Existing droop nose solutions are not suited for application on sailplane wings. Most of these concepts open large gaps, which would disturb the laminar flow and lead to a substantial performance decrease of the laminar profiles used. Achleitner & Baier (2016) built upon Wiessmeier's work and proposed the new droop nose wing concept shown in figure 1.2. Research on this concept is carried out in the project MILAN at the Institute of Aircraft Design at TUM.

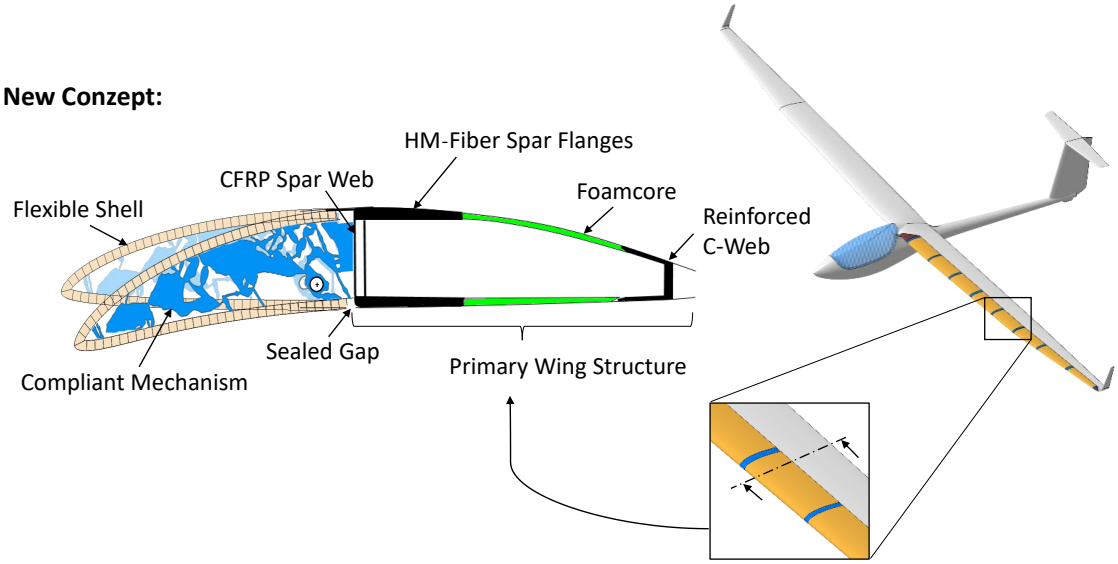

Figure 1.2: Adaptive droop nose concept of the project-MILAN (Achleitner & Baier 2016)

The adaptive droop nose concept in figure 1.2 consists of an anisotropic flexible shell (depicted in yellow) in the wings nose section, which is supported by deformable ribs (shown in blue). The primary structure is located in the rear part of the wing. The profile nose can be morphed by actuation of the ribs, which consist of compliant mechanisms.

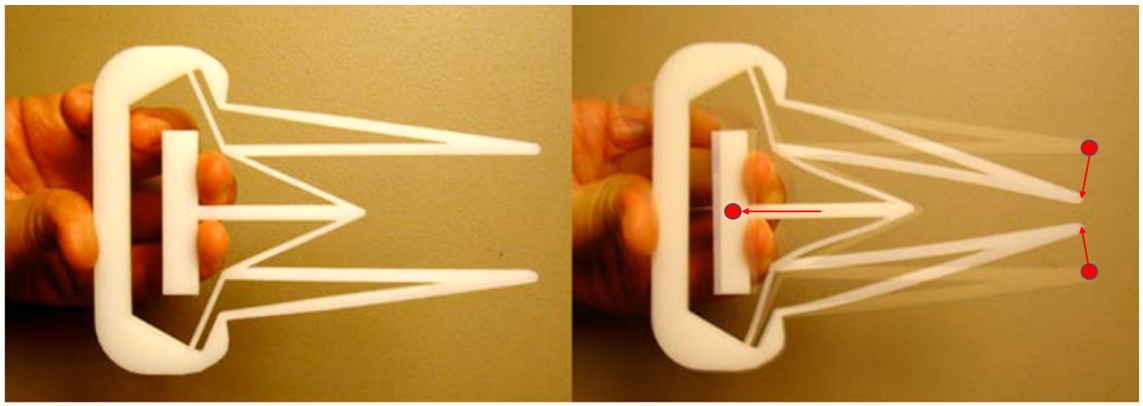

Figure 1.3: Compliant mechanism gripping tool (Kota et al. 2005)

Compliant mechanisms are kinematic mechanisms without conventional hinges. They gain their mobility by elastic deformation of their members (Sigmund 1997). A typical example for a compliant mechanism is the compliant gripping tool shown in figure 1.3. By pulling at the handle, the gripper closes. After releasing, the mechanism returns to its undeformed state. It is seen that the motion is allowed by deformation of thin elastic structures. Some

advantages of such compliant mechanisms are their small part count, no need of lubrication or maintenance and their self-restoring force (Sigmund 1997). Compliant mechanisms can be manufactured by additive manufacturing techniques. One method for the synthesis of compliant mechanisms is topology optimization.

First compliant mechanism ribs for the droop nose concept in figure 1.2 have already been designed by topology optimization in a prior work by Salehar (2015). Here, linear finite element methods (FEM) within the commercial software *Optistruct* were used. Based on the results obtained, first demonstrators for the MILAN project were built. One of them is illustrated in figure 1.4, where in the upper picture its undeformed state and in the lower picture its morphed state is shown. Looking at the deformed rib, kinks on the outer profile contour can be observed, moreover cracks in the hinge regions of the demonstrator appeared after a few actuations. These defects make clear, that further improvement of the mechanisms with respect to shape adherence and fatigue is necessary for real-world application.

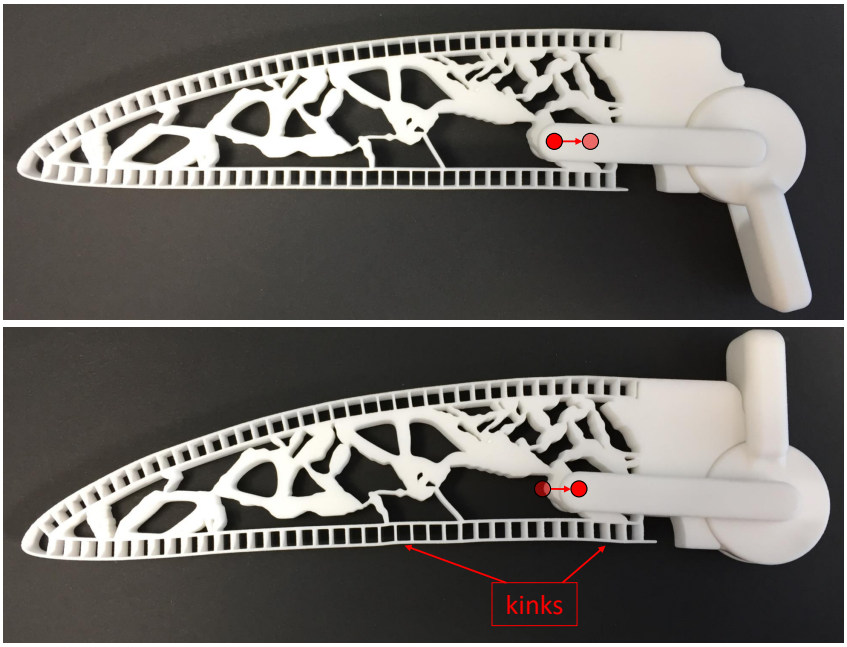

Figure 1.4: Laser sintered demonstrator of an integral compliant mechanism rib based on results by Salehar (2015)

A subsequent work by Salehar (2017) investigated possible improvements by the application of topology optimization with geometric nonlinear finite element modeling in *Optistruct*. The outcome was, that due to limited access possibilities to the optimization parameters and the highly sensitive behavior of nonlinear analysis in topology optimization, no satisfactory results

could be reached.

Another groundwork by the author (Reinisch 2017) consisted in the development of a *MATLAB* code for compliant mechanism topology optimization. The resulting *mechtop* code allows to optimize simple compliant mechanisms in 2D with regular finite element (FE) meshes. Methods for linear and for geometric nonlinear finite element analysis (FEA) are implemented. Moreover, a novel stress constraint formulation for nonlinear mechanism synthesis is introduced. The code was tested on the widely used compliant inverter benchmark problem.

The goal of this thesis is the further development of the *mechtop* code and the synthesis of compliant mechanism ribs for the project MILAN based on geometric nonlinear FEM. Therefore, the FE solver has to be adapted for non-regular mesh modeling. Moreover, the objective function formulation for exact output displacement presented by Pedersen et al. (2001), the so-called path-generation formulation is implemented.

At the beginning of this thesis, a general introduction to topology optimization theory is given. The newly implemented methods are described and an overview over the original state of the *mechtop* code is provided. The implementation is then shortly discussed, with special focus on the testing results obtained for a generic example problem. Furthermore, the new concept of a stacked compliant mechanism rib is introduced, for which rib-shaped mechanisms are designed using topology optimization with geometric nonlinear FEA. The related optimization formulation and the results obtained are discussed.

2 State of the Art

In this chapter the underlying theory of topology optimization is presented. A general introduction to topology optimization of compliant mechanisms is given based on a prior elaboration by the author (Reinisch 2017). Subsequently, the methods implemented in this work are described in detail and a short description of the used optimization algorithm is given. At the end of this section information about the original state of the software implementation at hand is provided.

2.1 Introduction to Topology Optimization

Topology optimization is a form of structural optimization, whereby the spatial material distribution is modified in order to improve a part's performance. The performance is measured by means of an objective function, which is minimized in an optimization loop. For continuum type topology optimization, considered in this thesis, a continuous design space Ω is discretized by finite elements. Through modification of the element stiffness matrices, the material distribution can be simulated. As initial information for the optimization only design space and boundary conditions have to be defined. In contrast to other structural optimization methods in topology optimization, the topology of a given structure is created by the optimization process and not just modified by it. Figure 2.1 shows an exemplary design space definition for an arbitrary topology optimization problem.

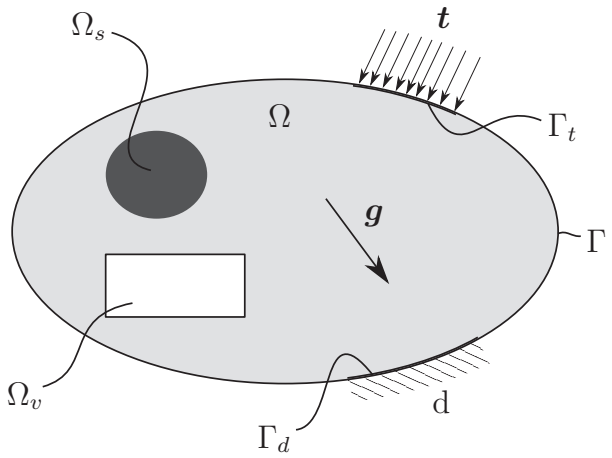

Figure 2.1: General topology optimization design space definition (Salehar 2015)

In figure 2.1 Ω is the design space, Ω_s and Ω_v are regions with prescribed solid or void material, respectively. Γ represents the boundary of the design space. As for the standard FE application, boundary conditions have to be defined. Displacement boundary conditions as

for instance fixed supports act at Γ_d. At Γ_t traction boundary conditions are applied, modeling external loads. g represents body loads which act on the domain Ω.

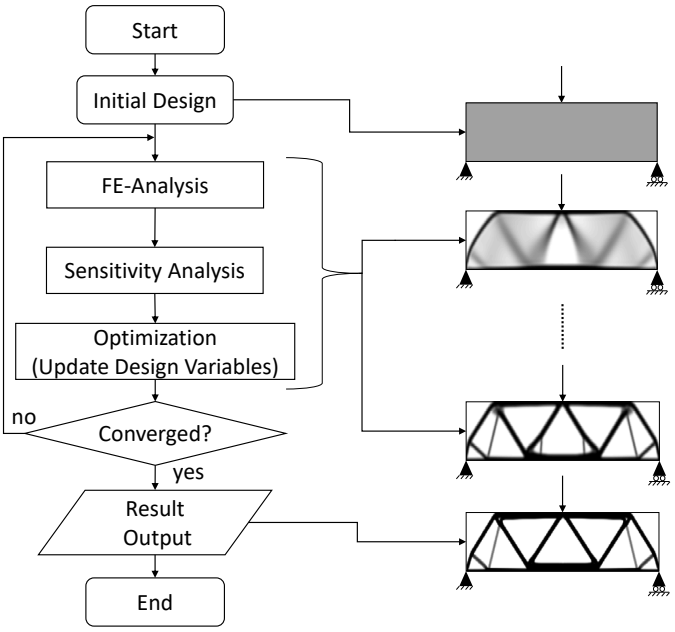

Figure 2.2: Workflow in topology optimization following Bendsøe & Sigmund (2004)

In figure 2.2, a flowchart describes the workflow of gradient-based topology optimization. As an example, the stiffness of a beam structure is maximized, applying the so-called minimum compliance problem formulation. In the upper right of figure 2.2, the initial design with predefined boundary conditions is shown, which consists of evenly distributed semi-dense material. Starting from this design, the material distribution is sequentially updated. For each design update a FE analysis is performed, followed by a sensitivity analysis. This provides the necessary gradient information to the optimization algorithm to calculate a modified material distribution in each iteration. Intermediate results are shown to the middle right. If no further improvement of the objective function can be achieved, the loop is stopped and the results are stored. To the lower right, the resulting truss-like optimal material distribution is illustrated.

Looking at figure 2.2, it becomes evident that in order to avoid trivial solutions a restriction to the amount of material available has to be introduced. Otherwise, the stiffest resulting topology would be a full material beam. This limitation is realised through volume constraints, which are used in most topology optimization problem formulations.

Arbitrary topology optimization problems can be defined using the standard optimization problem formulation in equation (2.1).

$$\begin{aligned} \underset{\boldsymbol{x}}{\text{minimize}} \quad & z(x_1, x_2, ..., x_n) && \boldsymbol{x} \in \boldsymbol{S} \\ \text{subject to:} \quad & g_j(x_1, x_2, ..., x_n) \leq 0 && j = 1, \ldots, p. \\ & h_k(x_1, x_2, ..., x_n) = 0 && k = 1, \ldots, q. \end{aligned} \tag{2.1}$$

In this equation, z is a general objective function, it is minimized by variation of the n design variables x within the range of allowable designs $\boldsymbol{S}$. The inequality constraints g_j and the equality constraints h_k have to be satisfied in order to obtain a feasible solution. The functions listed are related to the so-called system equations, which describe the physical behavior of the underlying problem. In topology optimization they are usually solved numerically by the finite element method. In an FE model the behavior of the elements can be influenced by changing their stiffness matrices. By this means, solid is modelled by using the base materials property parameters for the element stiffness matrix calculation, whereas for void modeling very low material property values are used. Therefore, in topology optimization a mathematical connection between design variables and element stiffness matrices has to be introduced.

Due to the discrete nature of the material distribution problem (only either solid or void exist), the design variables x are also discrete. Hence, the problem at hand is a discrete optimization problem, for which it takes high computational effort to solve. For this reason, the most common approach is to relax the problem, replacing the discrete design variable values with continuous ones (Bendsøe & Sigmund 2004). This also leads to a continuous functional relationship between design variables and element stiffness matrices. Several so-called interpolation methods exist, defining this relationship.

One approach is to use the homogenization method, first implemented by Bendsøe & Kikuchi (1988). It is based on homogenization of a porous medium by the rules of micromechanics and not only results in the material distribution, but also gives information about the orthotropic material properties in each element (Harzheim 2014). However, the most common interpolation method is the so-called SIMP approach based on isotropic material properties. This approach is also used in this work and discussed in the following section.

2.1.1 SIMP Solid Isotropic Material With Penalization

In density-based topology optimization, the normalized densities ρ_e of each finite element are the design variables. These are defined as follows:

$$\rho_e = \frac{\rho_{e,phys}}{\rho_0} \qquad 0 < \rho_e < 1 \tag{2.2}$$

where $\rho_{e,phys}$ is the physical density of the finite element and ρ_0 the density of the base material. The normalization, of the element densities $\rho_{e,phys}$ with respect to ρ_0 results in the design variable values ρ_e. In consequence solid elements are defined by $\rho_e = 1$ and void elements by $\rho_e = 0$. One approach to link the design variables ρ_e to the element stiffness matrices and further to the physical element behavior is the SIMP method.

Due to the underlying isotropic material, FE properties can be modified by changing only one parameter, namely the element's Young's modulus E_e. Therefore, this parameter is continuously linked to the element densities ρ_e by the SIMP relation. For the modeling of solid elements the Young's modulus is set to the base materials value E_0 and for the modeling of void elements very low values E_{min} are chosen. A zero Young's modulus for void elements has to be avoided, because of arising singularities in the stiffness matrices. As a result, the SIMP approach has to satisfy the following boundary conditions:

$$\begin{aligned} E_e = E_{min} \quad &\text{for} \quad \rho_e = 0 \quad , 0 < E_{min} \leq E \leq E_0 \\ E_e = E_0 \quad &\text{for} \quad \rho_e = 1 \end{aligned} \tag{2.3}$$

Whereas the SIMP approach can model the properties of any semi-dense material, in reality nothing in between solid and void material exists. Therefore, a penalty term k is introduced in order to circumvent solution topologies with semi-dense (grey) elements. The original formulation of the SIMP relation can then be written as follows:

$$E_e(\rho_e) = E_0 \rho_e^k \qquad \rho_{e,min} < \rho_e < 1 \tag{2.4}$$

Herein a lower bound of the design variable $\rho_{e,min}$ is introduced to make sure that the condition $E(\rho_{e,min}) = E_{min} > 0$ is satisfied. A modified SIMP formulation is applied in this work, it is

defined as:

$$E_e(\rho_e) = E_{min} + (E_0 - E_{min})\rho_e^k \qquad 0 < \rho_e < 1 \tag{2.5}$$

where the design variables ρ_e have their original 0-1 boundary values. This formulation is particularly suited for the application of special filtering techniques and has the advantage that void properties are not affected by the penalty term (Sigmund 2007).

In the FE model, each element stiffness matrix is first evaluated for the Young's modulus $E = 1$, resulting in K_{e0}. In a second step, this stiffness matrices are linearly modified by the corresponding SIMP terms, as shown in the following equation:

$$\boldsymbol{K}_e = (E_{min} + (E_0 - E_{min})\rho_e^k)\,\boldsymbol{K}_{e0} \tag{2.6}$$

By assembly of the element stiffness matrices K_e, the global stiffness matrix $\boldsymbol{K}$ is obtained.

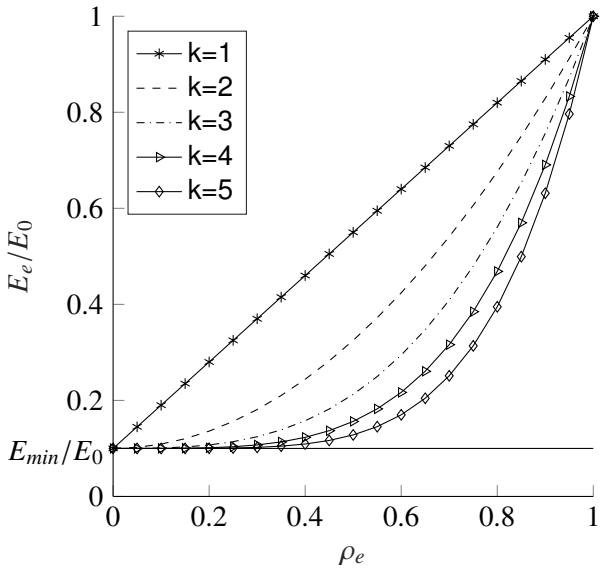

Figure 2.3: Modified SIMP-approach (Reinisch 2017)

Figure 2.3 illustrates the modified SIMP approach defined by equation (2.5). It becomes apparent that increasing penalty terms k penalize intermediate density elements. Starting from E_0 at $\rho_e = 1$ the stiffness values E drop fast towards E_{min} if high values of k are selected. In this way, semi-dense elements are made disadvantageous for the optimization algorithm (Harzheim 2014) . Discrete black and white solutions are the result.

2.1.2 Minimum Output Displacement Objective Function

For this work, the relevant application of topology optimization is the compliant mechanism synthesis, first introduced by Ananthasuresh et al. (1994) and Sigmund (1997). The task at hand consists in finding mechanism topologies, that satisfy a prescribed input-output motion relationship in a preferably energy efficient way. Due to the fact that generally, large displacements occur in compliant mechanisms, nonlinear effects cannot be neglected. Hence, the problem formulations listed in this thesis are all based on geometric nonlinear FEA. A detailed discussion of the linear objective function formulations can be found in (Bendsøe & Sigmund 2004) or (Reinisch 2017).

A simple objective function formulation for compliant mechanism synthesis is the minimization of output displacement at an arbitrary output node. In this section the nonlinear version of this problem formulation, first introduced by Pedersen et al. (2001), is discussed as an introductory example.

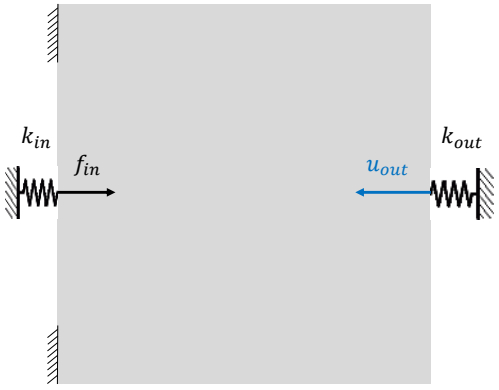

Figure 2.4: Compliant inverter benchmark problem sketch

A sketch of the widely used compliant inverter benchmark problem is shown in figure 2.4. It represents an exemplary application of the output displacement minimization objective function. To the left of figure 2.4 an input force f_{in} is applied at the input node and fixed supports are provided at the left corners of the rectangular design space. The stiffness values k_{in} and k_{out} are externally applied to model the actuator and work-piece behavior. The goal of the problem depicted in figure 2.4 is to find a mechanism, which translates the input force into an output displacement u_{out}, opposed to the input direction. This can be reached by the following

optimization formulation:

$$\begin{aligned} \underset{\boldsymbol{\rho}}{\text{minimize}} \quad & u_{out}(\boldsymbol{\rho}) = \boldsymbol{L}^{\mathbf{T}} \boldsymbol{U} \\ \text{subject to:} \quad & \boldsymbol{R}(\boldsymbol{U}) = \boldsymbol{K}(\boldsymbol{U})\,\boldsymbol{U} - \lambda \boldsymbol{F} = \mathbf{0} \\ & g_v = \frac{V}{v_{frac} V_\Omega} - 1 \leq 0 \\ & \mathbf{0} \leq \boldsymbol{\rho} \leq \mathbf{1} \end{aligned} \tag{2.7}$$

The output displacement u_{out} in equation (2.7) is minimized with respect to the element densities ρ_e, which are the entries of the design variable vector $\boldsymbol{\rho}$. $\boldsymbol{L}$ is an all-zero vector, except for the entry corresponding to the degree of freedom (DOF) of u_{out}. This entry is set to 1 or in case of maximization of the output displacement to -1. Also, a volume constraint is added, limiting the mechanisms volume V to the fraction v_{frac} of the total design space volume V_Ω, with $0 < v_{frac} \leq 1$. The volume is defined as:

$$V = \sum_e \rho_e v_e \tag{2.8}$$

where v_e are the element volumes in the undeformed state.

In equation (2.7) $\boldsymbol{R}(\boldsymbol{U}) = \mathbf{0}$ is the nonlinear system equation describing the structural behavior. This equation imposes that the residual between inner system force vector $\boldsymbol{K}(\boldsymbol{U})\,\boldsymbol{U}$ and external force vector $\lambda \boldsymbol{F}$ has to be zero in the equilibrium state. With λ being the explicit load incrementation factor, which equals to one for the fully converged solution. Moreover, $\boldsymbol{U}$ is the displacement vector and $\boldsymbol{K}(\boldsymbol{U})$ the nonlinear stiffness matrix depending on the deformations.

The representation of $\boldsymbol{R}$ in equation (2.7) is a special formulation of the geometric nonlinear FEM, allowing a simple approach to sensitivity analysis. The nonlinear stiffness matrix is defined in equation (A.11) in Appendix A.3.1. The nonlinear system equation is solved iteratively by the Newton-Raphson algorithm, which requires high computational effort.

2.1.3 Sensitivity Analysis

In gradient-based topology optimization sensitivities of the objective functions and constraints with respect to the design variables have to be calculated in each iteration. This gradient information is needed by the optimization algorithm to sequentially improve the design until an optimum is found. Due to the fact that, in topology optimization problems contain mostly only a few constraint functions, adjoint calculation of the gradient information is prevalently used.

If the functions only depend on ρ analytical gradients can easily be derived. In the case of dependence of other variables, the chain rule has to be applied. In order to avoid the calculation of difficult analytical sensitivities, as for example $\frac{\partial \boldsymbol{U}}{\partial \boldsymbol{\rho}}$, the adjoint method is used. The sensitivity analysis in topology optimization is outlined below, by the derivation of the gradients for the output displacement minimization problem formulation stated in equation (2.7).

The objective function derivatives for equation (2.7) are calculated by the adjoint method. Therefore, the residuum multiplied by an arbitrary vector $\boldsymbol{\lambda}_{adj}$, the so-called adjoint vector, is added to the objective function resulting in:

$$u_{out}(\boldsymbol{\rho}) = \boldsymbol{L}^{\mathbf{T}}\,\boldsymbol{U} + \boldsymbol{\lambda}_{adj}^{\mathbf{T}}\,\underbrace{(\boldsymbol{K}(\boldsymbol{U})\,\boldsymbol{U} - \lambda \boldsymbol{F})}_{\boldsymbol{R}} \tag{2.9}$$

This does not affect the objective function value, because $\boldsymbol{R} = \boldsymbol{0}$ in the equilibrium state. After derivation with respect to the design variable ρ_e the equation writes as follows:

$$\frac{\partial u_{out}}{\partial \rho_e} = \boldsymbol{L}^{\mathbf{T}}\,\frac{\partial \boldsymbol{U}}{\partial \rho_e} + \boldsymbol{\lambda}_{adj}^{\mathbf{T}}\Big(\frac{\partial \boldsymbol{R}}{\partial \boldsymbol{U}}\,\frac{\partial \boldsymbol{U}}{\partial \rho_e} + \frac{\partial \boldsymbol{R}}{\partial \rho_e}\Big) \tag{2.10}$$

where $\frac{\partial \boldsymbol{R}}{\partial \boldsymbol{U}}$ equals the tangent stiffness matrix $\boldsymbol{K}_T$ defined in equation (A.12). Now λ_{adj} is chosen such, that the unwanted term $\frac{\partial \boldsymbol{U}}{\partial \boldsymbol{\rho}}$ disappears from the equation. This is done by solving the so-called adjoint problem:

$$\boldsymbol{K}_T\,\boldsymbol{\lambda}_{adj} = -\boldsymbol{L} \tag{2.11}$$

where the symmetry of the tangent stiffness matrix is used. Computationally this equals to the solution of an additional linear load case. The objective function derivatives in consequence simplify to:

$$\frac{\partial u_{out}}{\partial \rho_e} = \boldsymbol{\lambda}_{adj}^{\mathbf{T}}\,\frac{\partial \boldsymbol{R}}{\partial \rho_e} \tag{2.12}$$

where the term $\frac{\partial \boldsymbol{R}}{\partial \rho_e}$ is further derived analytically to:

$$\frac{\partial \boldsymbol{R}}{\partial \rho_e} = \frac{\partial \boldsymbol{K}(\boldsymbol{U})}{\partial \rho_e}\,\boldsymbol{U} = k\,(E_0 - E_{min})\,\rho_e^{k-1}\,\boldsymbol{K}_{0e}(\boldsymbol{u}_e)\,\boldsymbol{u}_e \tag{2.13}$$

Equation (2.13) is only valid for the case of density independent external forces $\frac{\partial \boldsymbol{F}}{\partial \rho_e} = 0$, which applies for most compliant mechanism synthesis problems. In equation (2.13) k is the SIMP

penalty term, $\boldsymbol{K}_{0e}$ is the nonlinear element stiffness matrix calculated for $E = 1$ and $\boldsymbol{u}_e$ is the element nodal displacement vector.

For the volume constraint function in equation (2.7), which only depends on the design variables, the sensitivities can be directly calculated as follows:

$$\frac{\partial g_v}{\partial \rho_e} = \frac{v_e}{v_{frac} V_\Omega} \tag{2.14}$$

2.1.4 Numerical Complications in Topology Optimization

This section briefly discusses some numerical issues occurring in topology optimization. Namely the mesh dependency of the results, the appearance of so-called checkerboard patterns, one node connected hinges and instabilities due to large deformations in nonlinear FE analysis.

2.1.4.1 Mesh Dependency of the Results

The discrete 0-1 as well as the SIMP formulation of topology optimization problems in general lack of solutions on a continuous design space Ω. By introducing smaller and smaller topology elements into Ω, the solution could always be improved. This means that the set of admissible designs S is not closed. The emerging micro-structures furthermore have orthotropic material behavior and can therefore not be modelled correctly (Bendsøe & Sigmund 2004).

By an FE discretization, the continuous design space is divided into a discrete number of elements, thus a minimum length scale is imposed and a solution for the problem can be found. This means on the other hand, that the resulting topologies depend on the FE mesh selected. As shown in figure 2.5, totally different topologies result for the same problem, if the number of elements is changed. Ideally, this behavior should not occur. Finer FE meshes should result in a more accurate modeling of the same topology and not in different solutions.

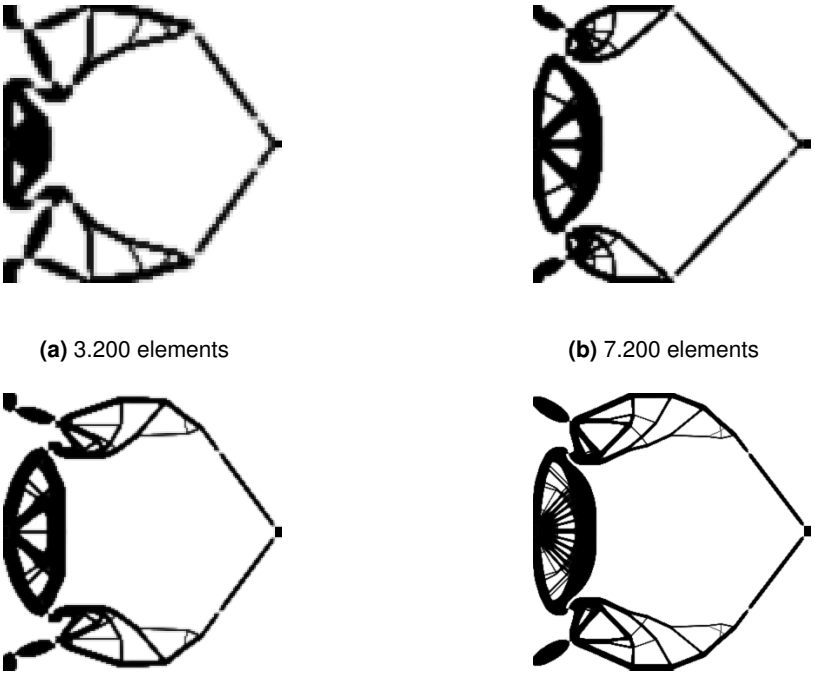

(a) 3.200 elements **(b)** 7.200 elements

(c) 12.280 elements **(d)** 51.200 elements

Figure 2.5: Examples for mesh dependent solutions of the compliant inverter benchmark problem (Reinisch 2017)

There are various methods in order to obtain the wanted mesh independent behavior of the results. They all in some way restrict the space of admissible designs, by limiting the allowed spatial variation of the densities (Bendsøe & Sigmund 2004). More precisely, three different groups of methods exist. The first group consists in adding extra constraints to the optimization problem, the second in directly reducing the parameter space for the designs. The most adopted and easy to implement mesh independency approach is the application of so-called filtering methods, where spatial filtering is applied to sensitivities or design variables in the optimization formulation (Lumpe 2015). These filtering methods are also used in this work and therefore further discussed in section 2.1.5.

2.1.4.2 Checkerboard Patterns

Often checkerboard-like regions appear within the solutions of topology optimization, especially models with bilinear quadrilateral finite elements are affected by this. The checkerboard patterns are sections with a periodical distribution of solid and void elements. Figure 2.6 shows a solution for a beam stiffness maximization problem, containing such checkerboard

patterns.

Figure 2.6: Beam stiffness maximization example result containing checkerboard patterns

The reason for the appearance of this phenomenon is bad numerical modeling by the finite element method, due to which the stiffness of checkerboard patterns is overestimated (Bendsøe & Sigmund 2004). One way to circumvent such bad modeling is to use higher-order elements, which are not subjected by the effect (Bendsøe & Sigmund 2004). Also, the filter methods mentioned in the previous section can be used to avoid checkerboarding. In this work checkerboard free results are obtained by the application of filtering methods.

2.1.4.3 Instabilities in Highly Distorted FE Meshes

When using geometric nonlinear finite element analysis, high displacement values occur in low density elements. These large distortions can lead to overlapping elements and in consequence even to negative element volumes, which further cause singularities of the tangent stiffness matrix. As a result, the analysis is unstable and the equilibrium iterations in the Newton-Raphson method do not converge.

There are three different approaches to face these convergence problems. The first one is to delete void elements from the FE mesh and to reintroduce them later if material is placed to the element (Bruns & Tortorelli 2003). The second method is to neglect all nodes surrounded by void elements in the convergence criterion of the FE analysis (Buhl et al. 2000). This is applicable because void elements do not influence the structural behavior of the topology and hence convergence of the residuum in this element is not necessary. The last approach proposed by Wang et al. (2014) and also used in this work is based on an energy interpolation scheme. The strain energy density terms ϕ, which underly to the finite element theory are interpolated continuously between the linear ϕ_L and nonlinear ϕ_{NL} expressions. This is done in order to obtain linear modeling in void elements and nonlinear modeling for the solid elements. An interpolation function can be defined as (Wang et al. 2014):

$$\phi_e(\boldsymbol{u}_e) = [\phi(\gamma_e \boldsymbol{u}_e) - \phi_L(\gamma_e \boldsymbol{u}_e) + \phi_L(\boldsymbol{u}_e)]E_e \tag{2.15}$$

where E_e is the elements Young's modulus and γ_e the energy interpolation factor. $\gamma_e = 1$ for solid material and $\gamma_e = 0$ for void material. A detailed description of the method is given in Wang et al. (2014). In this work a slightly modified approach is used according to Reinisch (2017). For completeness, the functions defining the interpolation method and the resulting sensitivity analysis scheme are listed in section A.4 in the Appendix. There also three different energy interpolation parameters are introduced as further optimization parameters.

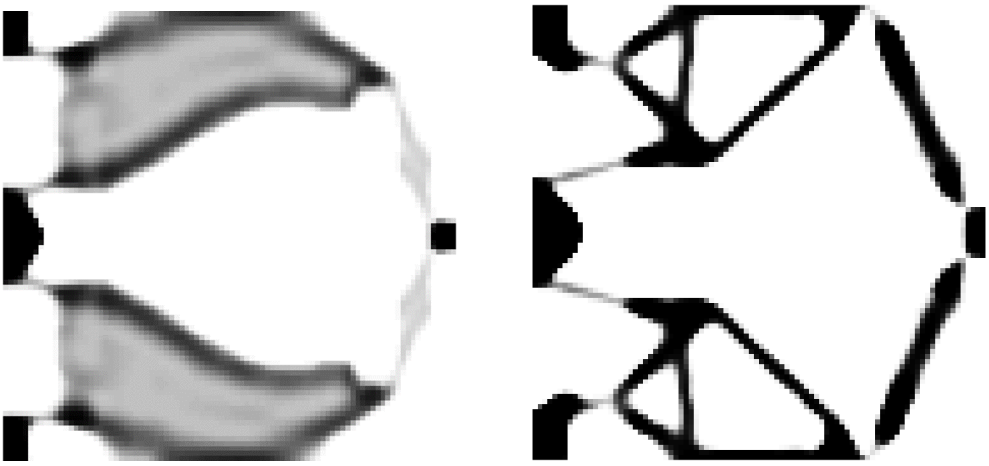

(a) Vast grey areas **(b)** Discrete solid/void design

Figure 2.7: Solutions of the compliant inverter benchmark problem with geometric nonlinear FEA (Reinisch 2017)

Sometimes unwanted effects appear applying the energy interpolation method if parameters are not set properly. By the application of the energy interpolation scheme it is allowed to the optimizer to choose between linear and nonlinear analysis by changing the element densities. In cases where linear analysis has a positive effect on the objective function, semi-dense material is introduced even for high SIMP penalization terms k. This occurs because depending on the interpolation parameters semi-dense elements can be modelled by linear FEM (see fig. A.4). Figure 2.7 shows a solution of the compliant inverter problem, where this occurred in (a). By choosing appropriate interpolation parameters the effect can be prevented as seen in (b) for the same problem.

2.1.4.4 One-Node Connected Hinges

In compliant mechanism synthesis by topology optimization flexible hinge regions within the solutions often reduce to a single point connection. The resulting one-node connected hinges or point flexures are not physically feasible. Similar to conventional hinges almost no moment

is transferred. However, in reality infinitely high stresses would occur in such sharp hinges. An exemplary inverter mechanism with one-node connected hinges can be seen in figure 2.8.

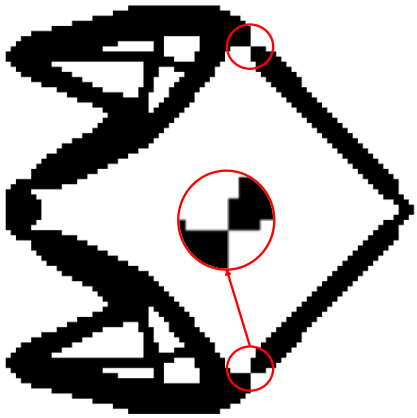

Figure 2.8: Compliant inverter solution with one-node connected hinges

As for the appearance of checkerboard patterns, this effect is caused by bad numerical modeling (Bendsøe & Sigmund 2004). Filtering methods can rarely alleviate the problem. The monotonicity based minimum length scale (MOLE) constraint formulation and the checkerboard (NoHinge) constraint introduced by Poulsen (2002, 2003) successfully prevent one-node connected hinges. Another approach applied in this work is the introduction of stress constraints proposed by De Leon et al. (2015).

2.1.5 Filtering Techniques

Filtering methods are used to alleviate the numerical problems described in section 2.1.4.1 and 2.1.4.2, namely the mesh dependency of results and checkerboard patterns. They impose a minimum length scale to the topology and thus are also often used to ensure manufacturability. The two main filtering techniques are the sensitivity filter (Sigmund 1997, 1994) and the density filter (Bruns & Tortorelli 2001). Both filters can be used together with projection methods (Guest et al. 2004), in order to eliminate grey transition areas from the results.

In this work, the results presented are obtained by the use of the density filtering scheme in combination with a modified projection method. Additionally, a filtering technique based on Helmholtz type partial differential equations (PDE) (Lazarov & Sigmund 2011) is implemented. These methods are introduced in this section. For information about other filtering techniques also implemented in this work, but not applied for the results presented, refer to Sigmund (2007).

2.1.5.1 Density Filter

The main concept of density filtering methods is to smooth the spatial density distribution, in order to get continuous transition areas between solid and void. No sharp transitions between black and white regions are allowed. This is done by weighted averaging of the element densities ρ over a defined element neighbouring region $\mathbb{N}_e$. Mathematically the density filter can be defined as follows:

$$\tilde{\rho}_e = \frac{\sum\limits_{i \in \mathbb{N}_e} H_{ei} v_i \rho_i}{\sum\limits_{i \in \mathbb{N}_e} H_{ei} v_i} \tag{2.16}$$

In equation (2.16) $\tilde{\rho}_e$ is the filtered density. The weighting factor is composed of the element volumes v, which account for different element sizes in non-regular FE meshes, and H_{ei}, which is the spatial weighting factor.

There are different definitions of spatial weighting factors. The most simple one is to weight all the elements within $\mathbb{N}_e$ with $H_{ei} = 1$. Also, a Gaussian distribution function was proposed weighting function (Bruns & Tortorelli 2003). The most widely used weighting function is a linear decaying (cone-shaped) function defined as follows (Sigmund 2007):

$$H_{ei} = \max(0, r_{min} - \|\boldsymbol{x}_i - \boldsymbol{x}_e\|) \tag{2.17}$$

where r_{min} is the filter radius and $\boldsymbol{x}_i$ and $\boldsymbol{x}_e$ are the location vectors of the element centroids.

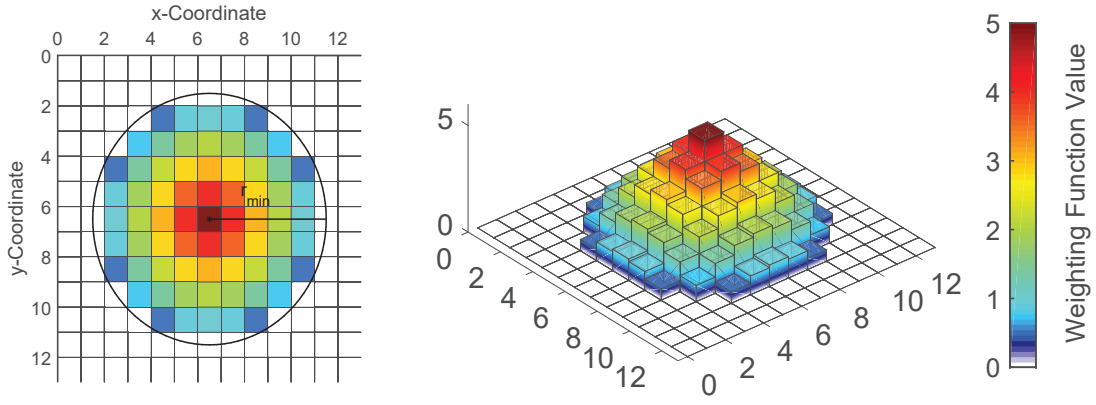

Figure 2.9: Visualization of the linear decaying filter weighting function H_{ei} ($e = 85, r_{min} = 5$)(Reinisch 2017)

Graphically this function is illustrated in figure 2.9, where the cone shape becomes evident.

The weighting function values H_{ei} linearly increase from zero at r_{min} to a maximum value for the central element e.

Applying the density filtering method, it is important to note, that the design variables ρ lose their physical meaning (Sigmund 2007). They are replaced by the filtered design variables $\tilde{\rho}_e$, which now define the structural behavior. Hence, the element stiffness matrices are defined as:

$$\boldsymbol{K}_e(\tilde{\rho_e}) = \left(E_{min} + (E_0 - E_{min})\,\tilde{\rho_e}^{\,k}\right)\boldsymbol{K}_{e0} \qquad 0 \leq \tilde{\rho_e} \leq 1 \tag{2.18}$$

where the SIMP approach according to equation (2.5) is used. The filtering process in the optimization loop takes place before the FE analysis.

Also, the volume constraint function of equation (2.7) has to be replaced by the following equation:

$$\frac{\sum_e \tilde{\rho_e} v_e}{V_\Omega v_{frac}} - 1 \leq 0 \qquad 0 < v_{frac} \leq 1 \tag{2.19}$$

Moreover, the sensitivity analysis is also affected by the filtering procedure. The system equation is no longer directly dependent on the design variable ρ. For this reason the gradients have to be found applying the chain rule. According to Andreassen et al. (2011) equation (2.20) describes this approach, where Ψ is an arbitrary function.

$$\frac{\partial \psi}{\partial \rho_e} = \sum_{j \in \mathbb{N}_e} \frac{\partial \psi}{\partial \tilde{\rho}_j} \frac{\partial \tilde{\rho}_j}{\partial \rho_e} \tag{2.20}$$

2.1.5.2 Heaviside-Projection

The application of density filters effectively prevents checkerboard patterns and creates mesh independent solutions. However, the resulting topologies often have grey transition areas from solid to void elements, depending on the size of the filter radius. Projection methods aim to achieve black and white solutions out of such topologies by eliminating the grey transition areas. Therefore, the density filter according to equation (2.16) is extended by an additional process, in which the filtered densities $\tilde{\rho}_e$ are projected to new physical densities $\overline{\tilde{\rho}}_e$ by a heaviside step. To ensure differentiability this discrete step has to be approximated by smooth

functions. Therefore, the following two approximation functions can be used:

$$\overline{\tilde{\rho}_e} = 1 - \mathrm{e}^{-\beta\tilde{\rho}_e} + \tilde{\rho}_e \mathrm{e}^{-\beta} \tag{2.21}$$

or

$$\overline{\tilde{\rho}_e} = \frac{\tanh(\beta\eta) + \tanh(\beta(\tilde{\rho}_e - \eta))}{\tanh(\beta\eta) + \tanh(\beta(1 - \eta))} \tag{2.22}$$

In both equations $\beta \geq 0$ is the function parameter determining the smoothness of the step. Moreover, η in equation (2.22) defines the element density threshold value for the step. Both Heaviside projection functions are depicted in figure 2.10. In fig. 2.10 (a) function (2.21) is plotted for different values of β. It is seen that for increasing β-values the approximation of the discrete step improves. The threshold for the approximation is in $\tilde{\rho}_e = 0$.

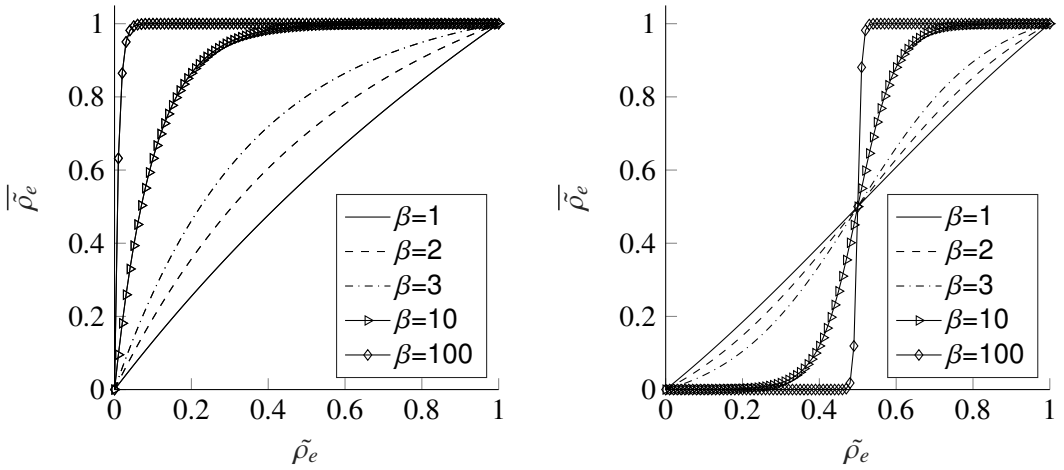

(a) Equation (2.21) **(b)** Equation (2.22), $\eta = 0.5$

Figure 2.10: Comparison of the two different Heaviside step approximations (Reinisch 2017)

In contrast to fig. 2.10 (a) the threshold value in fig. 2.10 (b) is shifted to $\tilde{\rho}_e = 0.5$ by the parameter η. Both steps are approximated equally well, fig. 2.10 (b) gives the advantage of an additional control parameter. Therefore, in this thesis the Heaviside projection defined by equation (2.22) is used.

The parameter β has also an important influence on the convergence behavior of the optimization. In order to avoid instabilities, usually a continuation scheme is applied for the parameter. At the beginning of the optimization mostly the initial value $\beta_0 = 1$ is selected, the β-parameter is then updated in each iteration until reaching a preset maximum value β_{max}. The continuation

scheme applied in this thesis writes as:

$$\beta = \min\left(\beta_{max}\,,\, \beta_0 * 2^{\frac{iter-1}{\tau}}\right) \tag{2.23}$$

Equation (2.23) causes a doubling of β after a prescribed number of iterations. This number of iterations is defined by the parameter τ.

Drawbacks of this β update scheme are that it is computationally expensive and that it causes slight convergence perturbations. In this work, in addition to the continuation scheme external move limits for the design variable changes of the optimizer are applied according to Reinisch (2017). By this means, oscillations in convergence can be reduced. This external move limits $\boldsymbol{\rho}_{min}$ and $\boldsymbol{\rho}_{max}$ are applied, starting from a β-threshold value of β_{start}. They are defined in Appendix A.5. Moreover, Guest et al. (2011) proposed a method to leave β constant on a high value. However, this method is not applied in this work.

As earlier mentioned for the density filters, also the application of the Heaviside projection method results in changed physical densities. In this case $\overline{\tilde{\rho}}_e$ becomes the governing parameter and hence in equations (2.18) and (2.19) $\tilde{\rho}_e$ has to be substituted by $\overline{\tilde{\rho}}_e$. Also, the chain rule for sensitivity analysis has to be reformulated to:

$$\frac{\partial \psi}{\partial \rho_e} = \sum_{j \in N_e} \frac{\partial \psi}{\partial \overline{\tilde{\rho}}_j} \frac{\partial \overline{\tilde{\rho}}_j}{\partial \tilde{\rho}_j} \frac{\partial \tilde{\rho}_j}{\partial \rho_e} \tag{2.24}$$

2.1.5.3 Partial Differential Equation (PDE) Based Filters

The density filter formulation described in section 2.1.5.1 needs for each element information about its neighborhood. This information is contained in the weighting factors H_{ei}, whose calculation is computationally and storage-wise very expensive. The reason for this is that the distances to the neighborhood elements centroids have to be calculated and stored for each element, which especially for large irregular FE meshes takes high computational effort. PDE-based filters allow the use of existing FE mesh information and FE solvers for the filtering operations and hence reduce computational cost. A density filtering method based on Helmholtz-type PDE's was first introduced by Lazarov & Sigmund (2011).

The filter equation in (2.16) equals to a discrete approximation of a convolution integral, which also corresponds to the solution of the Helmholtz PDE for homogeneous Neumann boundary

conditions (NBC) (Andreassen et al. 2011). This PDE is written as (Lazarov & Sigmund 2011):

$$-r^2\nabla^2\tilde{\Psi} + \tilde{\Psi} = \Psi \quad NBC: \quad \frac{\partial\tilde{\Psi}}{\partial \boldsymbol{n}} = 0 \tag{2.25}$$

where $\tilde{\Psi}$ and Ψ are the filtered and the unfiltered continuous representations of the design field respectively. The vector $\boldsymbol{n}$ in the boundary condition defines the normal to the boundary Γ of the domain Ω. r is the filter radius similar to r_{min} for the standard filter formulation. After FEM discretization and further simplification for the case of an isotropic filter (r is equal in each spatial direction) the equation writes as follows:

$$\underbrace{\sum_e \int_\Omega [r^2\, \nabla_{,\boldsymbol{x}} \boldsymbol{N}_e^{\mathbf{T}} \nabla_{,\boldsymbol{x}} \boldsymbol{N}_e + \boldsymbol{N}_e^{\mathbf{T}} \boldsymbol{N}_e] d\Omega}_{\boldsymbol{K}_F}\ \tilde{\boldsymbol{\rho}}_N = \underbrace{\sum_e \int_\Omega N_e^{\mathbf{T}} d\Omega}_{\boldsymbol{T}_F}\ \boldsymbol{\rho} \tag{2.26}$$

where $\boldsymbol{N}_e$ is the element shape function vector defined in (A.1) and $\sum_e$ in this case is the FE assembly operator. A shorter formulation of this equation is the following linear system:

$$\boldsymbol{K}_F\tilde{\boldsymbol{\rho}}_N = \boldsymbol{T}_F\boldsymbol{\rho} \tag{2.27}$$

which has to be solved in each filtering process. This can be done efficiently for example by Cholesky decomposition of $\boldsymbol{K}_F$ and subsequent forward and backward substitution or by iterative solvers.

$\tilde{\boldsymbol{\rho}}_N$ in equation (2.26) is the nodal representation of the filtered field. The element-wise representation of the filtered design variables, needed in the optimization, is obtained with the following equation:

$$\tilde{\boldsymbol{\rho}} = \frac{\boldsymbol{T}_F^{\mathbf{T}}\tilde{\boldsymbol{\rho}}_N}{\boldsymbol{v}} \tag{2.28}$$

where $\boldsymbol{T}_F$ represents the transformation matrix from element to nodal representation of the design variables and $\boldsymbol{v}$ is the element volume vector, which as for the standard density filter representation is a part of the weighting function. It is already included implicitly in the numerator of equation (2.28). For complete filtering, each solution of the linear system (2.27) is directly followed by the evaluation of equation (2.28).

The value for the PDE-based filter radius r, at which the same length scale is imposed as for the standard density based filter with radius r_{min}, can be calculated by the following equation

(Lazarov & Sigmund 2011):

$$r = \frac{r_{min}}{2\sqrt{3}} \tag{2.29}$$

The introduced PDE-based density filter can also be used together with a subsequent projection method as defined earlier in equations (2.21) and (2.22). For the sensitivity analysis the chain rule approaches according to equation (2.20) or (2.24) have to be applied.

2.2 Path-Generation Formulation

The path-generation formulation for compliant mechanism design was first introduced by Pedersen et al. (2001) and is discussed in this section. The main goal is not only to prescribe an extremal displacement of a single output node of the compliant mechanism, but to control multiple output displacement values for the output node in between the undeformed and the final deformed state. In contrast to the formulation in equation (2.7), that is only focusing on the minimization of the absolute output displacement value, in the path generation approach the deviation from the prescribed target displacement value is minimized. An objective function Φ for this optimization problem can be formulated as:

$$\Phi = \sum_{m=1}^{M} [\boldsymbol{u}_{out,m} - \boldsymbol{u}^*_{out,m}]^2 \tag{2.30}$$

which can be seen as a least square error approach. In equation (2.30) $\boldsymbol{u}_{out,m}$ are the actual and $\boldsymbol{u}^*_{out,m}$ the prescribed output displacement vectors, corresponding to the prescribed input displacement values $u_{in,m}$. The index m denotes the precision point number along the output deformation path for which the target output displacements $\boldsymbol{u}^*_{out,m}$ are prescribed. Although the results of this objective function are able to fulfil the prescribed input-output kinematic motion, they often contain large regions of semi-dense material. The reason for this is that the objective function above requires no ability of the mechanism to transfer loads. Grey areas can be avoided by applying additional counter load cases, for which the target displacement deviation must also be minimized and hence a stiff mechanism is required. Therefore, the objective function is written as follows (Pedersen et al. 2001):

$$\Phi = \sum_{i=0}^{2} \alpha_i \sum_{m=1}^{M} [\boldsymbol{u}_{out,m,i} - \boldsymbol{u}^*_{out,m}]^2 \tag{2.31}$$

In equation (2.31) the first sum includes three load cases, weighted by the factors α_i. The first load case ($i = 0$) can be interpreted as the mechanism generation load case, the other two

load cases ($i = 1, i = 2$) are the counter load cases enforcing a stiff mechanism. The counter loads are applied at the output nodes. Normally one counter load is chosen in opposite direction to the output displacement path at each precision point, the second counter load is selected perpendicular to the output path.

A general topology optimization problem including the path-generation objective function can be defined according to equation (2.7) as:

$$\begin{aligned} \underset{\boldsymbol{\rho}}{\text{minimize}} \quad & \Phi = \sum_{i=0}^{2} \alpha_i \sum_{m=1}^{M} [\boldsymbol{u}_{out,m,i} - \boldsymbol{u}^*_{out,m}]^2 \\ \text{subject to:} \quad & \boldsymbol{R}(\boldsymbol{U}) = \boldsymbol{K}(\boldsymbol{U})\,\boldsymbol{U} - \lambda \boldsymbol{F} = \boldsymbol{0} \\ & g_v = \frac{V}{v_{frac} V_\Omega} - 1 \leq 0 \\ & \boldsymbol{0} \leq \boldsymbol{\rho} \leq \boldsymbol{1} \end{aligned} \tag{2.32}$$

Pedersen also included input force constraints in this formulation. Those are not regarded here, because the input force sensitivities could not be calculated by the same procedure as the objective functions sensitivities in section 2.2.2. And in the original publication, no information regarding the input force sensitivity analysis is given.

A requirement for the implementation of the path generation objective function is the application of nonlinear FEM. In order to prescribe the input displacement steps a displacement-controlled Newton-Raphson approach is applied. This approach is shortly introduced in the following section, followed by the derivation of the objective function sensitivities.

2.2.1 Displacement-Controlled Nonlinear FEM

Nonlinear FE problems are solved by sequential linearization in incremental iterative procedures. A control parameter is incremented and for each increment the new equilibrium state $\boldsymbol{R} = \boldsymbol{0}$ is found by the Newton-Raphson method. In this manner, the systems equilibrium path is followed. The basic approach is to select the force incrementation parameter $0 \leq \lambda \leq 1$ as control parameter. Thus, external forces are sequentially increased by defining explicit λ increments, starting from a small initial value.

Because the path generation objective function formulation contains input displacement steps $u_{in,m}$, it is advantageous to select the input displacement as control parameter. By this means, the structural response for the given input displacement steps $u_{in,m}$ is directly calculated. Since the mathematical formulation of the total residuum is decisive for sensitivity analysis, a short

description of the displacement-controlled formulation of FEM is given here.

The displacement-controlled FE approach is implemented by adding an additional control equation to the system. The control equation f can be formulated as:

$$f = \Delta U_c - \Delta \hat{U}_c = 0 \tag{2.33}$$

where ΔU_c is the actual and $\Delta \hat{U}_c$ the prescribed displacement increment in the controlled degree of freedom (DOF). By setting the condition $f = 0$, the displacement step size $\Delta \hat{U}_c$ is imposed. Furthermore, the load incrementation parameter λ is here no longer given explicitly. It must be added to the state variable vector. The resulting extended equilibrium equation writes as follows:

$$\boldsymbol{R}_{ext} = \begin{bmatrix} \boldsymbol{R}(\boldsymbol{U}, \lambda) \\ f(\boldsymbol{U}, \lambda) \end{bmatrix} = \begin{bmatrix} \boldsymbol{K}(\boldsymbol{U})\boldsymbol{U} - \lambda \boldsymbol{F} \\ \Delta U_c - \Delta \hat{U}_c \end{bmatrix} = \boldsymbol{0} \tag{2.34}$$

where $\boldsymbol{R}_{ext}$ is the total residuum. This equation is linearised and solved by the Newton-Raphson method. The linearization and the overall FE solver procedure can be seen in Appendix (A.15) and A.3 respectively. Because displacement in only one degree of freedom can be prescribed by this method, also in the path-generation approach the input u_{in} can only be prescribed in one DOF.

The outlined displacement control approach allows accounting results for multiple precision points $u_{in,m}$ within one nonlinear analysis. This is done by setting the prescribed displacement step values to the precision point values $\hat{U}_{c,m} = u_{in,m}$.

In the general representation of the described method according to equation (2.34), the total load vector F is modified by the load incrementation parameter λ. In case of the path-generation formulation, input force and counter loads would be modified in the same way, in order to obtain the prescribed deformation. Hence, for different precision points $u_{in,m}$ different counter loads would be applied. Because the same counter loads have to be applied for each precision point, the displacement control formulation has to be modified. Instead of multiplying the whole load vector $\boldsymbol{F}$ with λ, only the entry corresponding to the input force can be adapted. This is done by the $\boldsymbol{\lambda}$ and $\boldsymbol{R}$ formulations in equation (A.16) and (A.17), used in this work for path-generation topology optimization.

2.2.2 Sensitivity Analysis

The derivative of the objective function for the path-generation problem formulation in (2.32) can be written as:

$$\frac{\partial \Phi}{\partial \rho_e} = \sum_{j=1}^{n_j} \sum_{i=0}^{2} \alpha_i \sum_{m=1}^{M} 2 * \frac{\partial u_{out,m,i,j}}{\partial \rho_e} (u_{out,m,i,j} - u^*_{out,m,j}) \tag{2.35}$$

where the index j denotes the j-th entry of the output displacement vector $\boldsymbol{u}_{out,m,i}$ and n_j the number of controlled output DOFs and hence the length of the vector. In this term the sensitivities $\frac{\partial u_{out,m,i,j}}{\partial \rho_e}$ are unknown. They are obtained analogue to section 2.1.3 by the adjoint method. The slight difference is that an approach for coupled systems is applied here (Michaleris et al. 1994). This is done because the residual function is extended by the control equation f for displacement control and the load increment factor λ is a variable. Therefore, also the partial derivatives with respect to λ have to be accounted for. The derivative including the added residual terms $\boldsymbol{R}$ and f in equations (2.34) and (2.33) follows as:

$$\begin{aligned} \frac{\partial u_{out,m,i,j}}{\partial \rho_e} = \cancelto{0}{\frac{\partial \boldsymbol{L}^{\mathbf{T}} \boldsymbol{U}}{\partial \rho_e}} + \frac{\partial \boldsymbol{L}^{\mathbf{T}} \boldsymbol{U}}{\partial \boldsymbol{U}} \frac{\partial \boldsymbol{U}}{\partial \rho_e} + \frac{\partial \boldsymbol{L}^{\mathbf{T}} \boldsymbol{U}}{\partial \lambda} \frac{\partial \lambda}{\partial \rho_e} + \\ + \boldsymbol{\lambda}^{\mathbf{T}}_{adj,1} \Big[\frac{\partial \boldsymbol{R}}{\partial \rho_e} + \frac{\partial \boldsymbol{R}}{\partial \boldsymbol{U}} \frac{\partial \boldsymbol{U}}{\partial \rho_e} + \frac{\partial \boldsymbol{R}}{\partial \lambda} \frac{\partial \lambda}{\partial \rho_e} \Big] + \lambda_{adj,2} \Big[\cancelto{0}{\frac{\partial f}{\partial \rho_e}} + \frac{\partial f}{\partial \boldsymbol{U}} \frac{\partial \boldsymbol{U}}{\partial \rho_e} + \cancelto{0}{\frac{\partial f}{\partial \lambda} \frac{\partial \lambda}{\partial \rho_e}} \Big] \end{aligned} \tag{2.36}$$

where $\lambda_{adj,1}$ is the adjoint vector for the residual $\boldsymbol{R}$ and $\lambda_{adj,2}$ a constant adjoint factor for the control equation f. This expression simplifies with residuum equation $\boldsymbol{R}(\boldsymbol{U}) = \boldsymbol{K}(\boldsymbol{U})\,\boldsymbol{U} - \lambda \boldsymbol{F}$ and the relation $\frac{\partial \boldsymbol{R}}{\partial \boldsymbol{U}} = \boldsymbol{K}_T$ to:

$$\frac{\partial u_{out,m,i,j}}{\partial \rho_e} = \boldsymbol{L}^{\mathbf{T}} \frac{\partial \boldsymbol{U}}{\partial \rho_e} + \boldsymbol{L}^{\mathbf{T}} \frac{\partial \boldsymbol{U}}{\partial \lambda} \frac{\partial \lambda}{\partial \rho_e} + \boldsymbol{\lambda}^{\mathbf{T}}_{adj,1} \Big[\frac{\partial \boldsymbol{R}}{\partial \rho_e} + \boldsymbol{K}_T \frac{\partial \boldsymbol{U}}{\partial \rho_e} + \boldsymbol{F} \frac{\partial \lambda}{\partial \rho_e} \Big] + \lambda_{adj,2} \frac{\partial f}{\partial \boldsymbol{U}} \frac{\partial \boldsymbol{U}}{\partial \rho_e} \tag{2.37}$$

where as in section 2.1.3 a density independent external force vector $\frac{\partial \boldsymbol{F}}{\partial \rho_e} = 0$ was assumed.

$$\frac{\partial \boldsymbol{U}}{\partial \boldsymbol{\lambda}} = \boldsymbol{K}_T^{-1} \boldsymbol{F} \tag{2.38}$$

Further using the relation (2.38), which derives from $\Delta \boldsymbol{U}_F$ in figure A.3 applying the condition $\frac{\partial}{\partial \boldsymbol{U}} = \frac{\partial}{\partial \Delta \boldsymbol{U}}$ (Pohl 2014), the first adjoint equation can be written as follows:

$$\mathbf{0} = \Big[\boldsymbol{L}^{\mathbf{T}} \boldsymbol{K}_T^{-1} \boldsymbol{F} + \boldsymbol{\lambda}^{\mathbf{T}}_{adj,1} \boldsymbol{F} \Big] \frac{\partial \lambda}{\partial \rho_e} \tag{2.39}$$

This equation then results in the adjoint problem:

$$\boldsymbol{K}_T \boldsymbol{\lambda}_{adj,1} = -\boldsymbol{L} \tag{2.40}$$

which is equal to equation (2.11). By this choice, $\frac{\partial \lambda}{\partial \rho_e}$ cancels out of equation (2.37). In order to eliminate also the $\frac{\partial \boldsymbol{U}}{\partial \rho_e}$ terms, the second adjoint equation (2.41) must also be fulfilled.

$$\mathbf{0} = \Big[\boldsymbol{L}^{\mathbf{T}} + \boldsymbol{\lambda}_{adj,1}^{\mathbf{T}} \boldsymbol{K}_T + \lambda_{adj,2} \frac{\partial f}{\partial \boldsymbol{U}}\Big] \frac{\partial \boldsymbol{U}}{\partial \rho_e} \tag{2.41}$$

This leads to the value of the second adjoint factor $\lambda_{adj,2} = 0$. The sensitivities $\frac{\partial u_{out,m,i,j}}{\partial \rho_e}$ in consequence are calculated in the same manner, as prior for the displacement objective function under load control by equation (2.13). After insertion in equation (2.35) the objective function sensitivities for the path generation approach are obtained.

The sensitivity analysis was outlined for the case of λ modification of the entire load vector $\boldsymbol{F}$. The derived sensitivities are also valid for the $\boldsymbol{\lambda}$ and $\boldsymbol{R}$ formulations according to equations (A.16) and (A.17), introduced in the previous section.

2.3 Multiresolution Topology Optimization (MTOP)

The multiresolution topology optimization scheme (MTOP) was proposed by Nguyen et al. (2010). The main concept is to employ different discretization levels for the FE analysis, for the design variables and for the densities. This is done, in order to reduce the computational cost of high-resolution topology results, especially for large problems. In this work, the method is also implemented and therefore described in this section. Whereas in the above mentioned publication different design variable and density discretizations are considered, here only the special case of equal design variable and density meshes is regarded. For information about other variants of the method the reader is referred to Nguyen et al. (2010).

The basic idea of the MTOP approach is to use already existing information from the FEA to create higher resolution topologies. Element stiffness matrices are calculated by integration over the element domain. This integration is usually done by Gauss integration, splitting the integral into a weighted sum over discrete gauss integration points. By this means, each of this integration points has its own contribution $\boldsymbol{K}_{e0,gp}$ to the element stiffness matrix $\boldsymbol{K}_e$. $\boldsymbol{K}_e$ is calculated as:

$$\boldsymbol{K}_e = (E_{min} + (E_0 - E_{min})\rho_e^k) \sum_{gp=1}^{ngp} \boldsymbol{K}_{e0,gp} \tag{2.42}$$

where ngp is the number of Gauss integration points. The SIMP method is applied here according to equation (2.6).

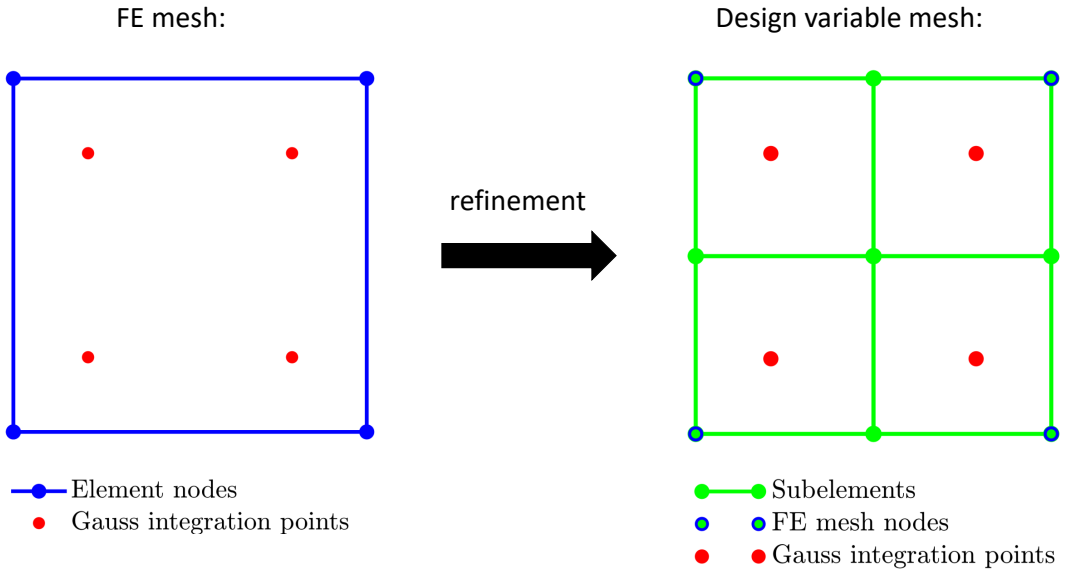

Figure 2.11: Concept of multiresolution topology optimization (MTOP)

By introducing a finer design variable mesh to each of these contributions $\boldsymbol{K}_{e,gp}$, a distinct density $\rho_{e,gp}$ can be assigned and hence the existing stiffness information is used to generate higher resolution results. Graphically this is illustrated in figure 2.11.

The refined element to the right of figure 2.11 is divided into four subelements, each of which has its own density value associated to the integration point. The basic FE discretization by four node finite elements with four Gauss points does not change, and the computational cost of the FE analysis is therefore almost the same. Only the number of design variables increases by the factor four, leading to an increase of optimization cost. The SIMP approach for the element stiffness matrix and its Gauss points contributions is defined as:

$$\boldsymbol{K}_e = \sum_{gp=1}^{ngp} (E_{min} + (E_0 - E_{min})\rho_{e,gp}^k)\boldsymbol{K}_{e0,gp} \tag{2.43}$$

Moreover, the equation for the volume V in the volume constraint formulation according to equation (2.7) is changed to the following form:

$$V = \sum_{gp}\sum_{e} \rho_{e,gp} v_{e,gp} \tag{2.44}$$

In equation (2.44) $v_{e,gp}$ is the volume of the subelement for the Gauss point gp of the element e. Also the sensitivities in equations (2.13) and (2.14) are calculated using $\rho_{e,gp}$,$v_{e,gp}$ and $\boldsymbol{K}_{e0,gp}$ instead of ρ_e and $\boldsymbol{K}_{e0}$, if the MTOP approach is applied. The subelements are assembled to a new global design variable mesh. The results of the MTOP approach are discussed in section 3.5.

2.4 Stress Constraint Formulation

A constraint formulation for a global stress measure in compliant mechanism design based on linear FEM was first introduced by De Leon et al. (2015). Stress constraints can be applied to reduce stress peaks within the topologies. This is especially useful to eliminate one-node connected hinges from the results (see section 2.1.4.4) and to obtain fatigue-resistant mechanisms. De Leon's stress constraint formulation was adopted in a previous work to geometric nonlinear topology optimization of compliant mechanisms (Reinisch 2017). The adopted implementation is also used in this work and therefore briefly introduced in this section.

The stress constraint equation is written as:

$$g_s(\boldsymbol{\rho}) = \frac{\tilde{\sigma}_{PN}}{\sigma^*} - 1 \leq 0 \tag{2.45}$$

where σ^* is the stress limit value and $\tilde{\sigma}_{PN}$ the normalized global p-norm stress measure. It approximates the maximum appearing stress value and is calculated by the normalization of the p-norm stresses σ_{PN},

$$\tilde{\sigma}_{PN} = c\sigma_{PN} \tag{2.46}$$

where c is the normalization parameter calculated in each iteration n by equation (2.47).

$$c^n = 0.5\frac{\sigma_{max}^{n-1}}{\sigma_{PN}^{n-1}} + 0.5c^{n-1} \tag{2.47}$$

With σ_{max}^{n-1} being the actual appearing maximum stress in the previous iteration. $c^0 = 1$ is selected as initial normalization value. The normalization improves the approximation of the maximum stress (De Leon et al. 2015).

The p-norm stress σ_{PN} is defined in a modified version by Le et al. (2010) with the following equation:

$$\sigma_{PN} = \Big(\underbrace{\sum_{e \in \mathbb{N}_\sigma} v_e \sigma_e^p}_{\sigma_{sum}} \Big)^{1/p} = \sigma_{sum}^{1/p} \tag{2.48}$$

where $\mathbb{N}_\sigma$ is the set of stress constraint elements, p the p-norm parameter and σ_e is the relaxed element von Mises stress. v_e is the element volume. For $p \to \infty$ the p-norm approximation approaches the maximum stress value $\max(\sigma_e)$. In this work, the p-norm parameter $p = 12$ is selected. The von Mises stresses $\sigma_{vm,e}$ are relaxed by the following equation:

$$\sigma_e = \overline{\tilde{\rho}_e}^q \sigma_{vm,e} \tag{2.49}$$

This is done in order to smooth the design space and hence alleviate the so-called singularity problem (Le et al. 2010). $\overline{\tilde{\rho}_e}$ are the physical densities and q is the relaxation parameter. A common value is $q = 0.5$. The von Mises stresses $\sigma_{vm,e}$ are calculated from the second Piola-Kirchhoff stresses and more in detail from the strain field, assuming solid material for each element $E_e = E_0$. The equations for the FE stress analysis are listed in Appendix A.3.

The sensitivities of the stress constraint function for geometric nonlinear FE are derived in Reinisch (2017) resulting in:

$$\frac{\partial g_s}{\partial \overline{\tilde{\rho}_e}} = \frac{1}{\sigma^*} c \sigma_{sum}^{\frac{1}{p}-1} v_e \boldsymbol{\sigma}_e^{p-1} q \overline{\tilde{\rho}_e}^{q-1} \sigma_{vm,e} + k(E_0 - E_{min}) \overline{\tilde{\rho}_e}^{k-1} \boldsymbol{\lambda}^{\sigma\mathbf{T}} \boldsymbol{K}_{0e}(\boldsymbol{u}_e) \boldsymbol{u}_e \tag{2.50}$$

The adjoint vector $\boldsymbol{\lambda}^{\sigma\mathbf{T}}$ is obtained from the solution of the adjoint problem:

$$\boldsymbol{K}_T^{\mathbf{T}} \boldsymbol{\lambda}^{\sigma} = -\frac{\partial g_s}{\partial \boldsymbol{U}}^{\mathbf{T}} \tag{2.51}$$

and $\frac{\partial g_s}{\partial \boldsymbol{u}_e}$ is calculated element wise according to equation (2.52).

$$\frac{\partial g_s}{\partial \boldsymbol{u}_e}^{\mathbf{T}} = \frac{c \sigma_{sum}^{\frac{1}{p}-1} v_e \sigma_e^{p-1} \overline{\tilde{\rho}_e}^q}{\sigma^* \sigma_{vm,e}} \boldsymbol{B}_L^{\mathbf{T}} \overline{\boldsymbol{F}} \boldsymbol{C}_{VK} \boldsymbol{V} \boldsymbol{\sigma}_e \tag{2.52}$$

The element terms $\frac{\partial g_s}{\partial \boldsymbol{u}_e}$ are then assembled to the global vector $\frac{\partial g_s}{\partial \boldsymbol{U}}$ needed in equation (2.51). The bold terms to the right of equation (2.52) are defined in Appendix A.3.

2.5 Method of Moving Asymptotes (MMA)

Topology optimization problems generally have a high number of design variables and only few constraint functions. For the solution of problems of this form so-called dual methods are well suited. Applying these methods design variables are expressed as a function of Lagrange multipliers. This allows a reduction of the optimization problems dimension, to the number of unknown Lagrange multipliers. For topology optimization problems this means

that the dimension of the underlying optimization problem can be reduced up to the number of constraint functions and hence the optimizations computational cost can be reduced. A precondition for the application of dual methods is that the optimization problem is separable (Harzheim 2014).

To ensure separability for general optimization problems sequential approximate optimization algorithms can be used. Those algorithms approximate the objective function and constraints locally by separable functions. In this thesis, for this purpose the Method of Moving Asymptotes (MMA) introduced by Svanberg (1987) is applied.

The MMA is a gradient-based optimization algorithm. It locally approximates the optimization problem to a convex separable subproblem and subsequently solves this subproblem by the use of dual methods. The form of the approximation is exemplarily defined for the objective function z in iteration j by the following equation:

$$z(\boldsymbol{x}) \approx z(\boldsymbol{x}^j) + \sum_{i=1}^{n} \Big(\frac{r_i}{U_i - x_i} + \frac{s_i}{x_i - L_i} \Big) \tag{2.53}$$

where x_i are the design variables. The parameters r_i and s_i are defined in dependence of the sensitivity information as:

$$\begin{aligned} &\text{if} \quad \frac{\partial z}{\partial x_i}(\boldsymbol{x}^j) > 0: \quad r_i = (U_i - x_i^j)^2 \frac{\partial z}{\partial x_i}(\boldsymbol{x}^j) \quad \text{and} \quad s_i = 0 \\ &\text{if} \quad \frac{\partial z}{\partial x_i}(\boldsymbol{x}^j) < 0: \quad s_i = -(x_i^j - L_i)^2 \frac{\partial z}{\partial x_i}(\boldsymbol{x}^j) \quad \text{and} \quad r_i = 0 \end{aligned} \tag{2.54}$$

The approximation (2.53) can be linear or reciprocal (limit cases) or a intermediate stage of both depending on the values of L_i and U_i. These parameters L_i and U_i are the lower and the upper asymptotes respectively. They limit the design variable range of the approximation and are moved during the optimization in order to improve the convergence behavior. A conservative approach for the asymptotes modification is defined in equation (2.55) (Harzheim 2014).

$$\begin{aligned} &\text{for:} \quad (x_i^j - x_i^{j-1})(x_i^{j-1} - x_i^{j-2}) < 0 \\ &\qquad L_i^j = x_i^j - \frac{1}{s^2}(x_i^{j-1} - L_i^{j-1}) \qquad \text{or} \quad U_i^j = x_i^j + \frac{1}{s^2}(U_i^{j-1} - x_i^{j-1}) \end{aligned} \tag{2.55}$$

$$\begin{aligned} &\text{for:} \quad (x_i^j - x_i^{j-1})(x_i^{j-1} - x_i^{j-2}) \geq 0 \\ &\qquad L_i^j = x_i^j - s(x_i^{j-1} - L_i^{j-1}) \qquad \text{or} \qquad U_i^j = x_i^j + s(U_i^{j-1} - x_i^{j-1}) \end{aligned}$$

By equation (2.55) the asymptotes can either widened or tightened. This depends on the directions of the optimization steps $x_i^j - x_i^{j-1}$ in iteration j and $j-1$. If both steps have the same direction the asymptotes are widened and if opposed step directions are detected a narrowing of the asymptotes occurs. By this means, convergence is stabilized in case of oscillations and in the contrary case the algorithm is accelerated. The asymptote control parameter s determines the movement of the asymptotes . Small s values lead to a conservative approximation. A frequently used value is $s = 1.07$.

One advantage of the MMA is its compatibility to multiple constraint formulations. Moreover, in contrast to the optimality criteria method, also often used in topology optimization, the algorithm must not be changed to account for other objective function formulations. Also special objective function formulations as min-max problems or minimization of sqare errors are preimplemented and can therefore easily be optimized.

2.6 *mechtop*: Original Software Implementation

In a previous work, the author (Reinisch 2017) developed a *MATLAB* code for topology optimization of compliant mechanisms, based on the 99-line and the 88-line *MATLAB* codes of the *TopOpt* group of the Technical University of Denmark (Sigmund 2001) (Andreassen et al. 2011). This code builds the basis for further function implementations and mechanism optimizations in this thesis, therefore the original state of the code and its limitations are summarized in this section.

The original version of the code allows to generate compliant mechanisms for the minimization of output displacement objective function formulation (see equation (2.7)). Therefore, either topology optimization methods based on linear FEM, or on geometric nonlinear FEM can be applied. Moreover, for both cases a stress constraint formulation is available in order to prevent local hinges. Sensitivity and density filtering methods, as well as the two Heaviside projection schemes introduced in section 2.1.5.2 are implemented, allowing the user to select the applied filter type. The total Lagrangian implementation of the geometric nonlinear FE solver is based on a *MATLAB* program for membrane analysis (Patil 2015). The formulation is defined by the use of Green-Lagrange strains and second Piola-Kirchhoff stresses. Underlying equations are listed in the Appendix A.3.1.

There are several limitations of the code. First, the designs space is restricted to two dimensional problems and must be discretized by a regular FE mesh. Moreover, only rectangular domain geometries are implemented and only bilinear quadrilateral elements under the con-

dition of plane stress can be analysed.

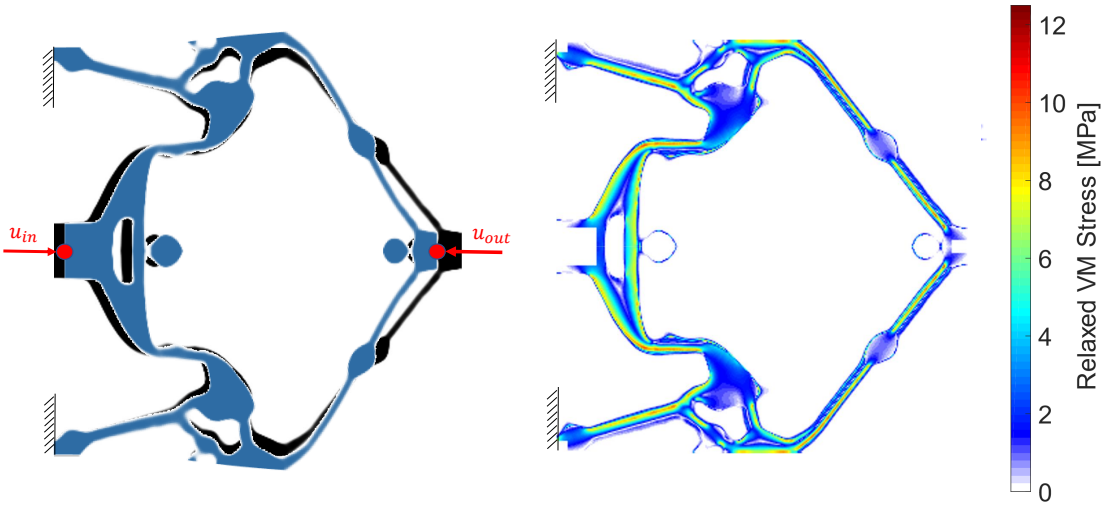

Figure 2.12: Exemplary result obtained by the original optimization code (*mechtop*) for a stress constraint compliant inverter problem (linear FEA)

The original implementation of the *mechtop* code was validated in (Reinisch 2017) by multiple optimizations of the compliant inverter benchmark problem (see fig. 2.4) and comparison to published results. A linear stress constraint example result is illustrated in figure 2.12, demonstrating the basic capability of the original optimization software. The stress limit value in figure 2.12 is set to $\sigma^* = 10\,\mathrm{MPa}$.

Observing the result in figure 2.4 it is seen that long bending members are introduced in the hinge regions. By this means, stresses are equally spread over the whole topology. It is also noticed that the underlying plane stress assumption may not be valid in these thin members, because the width of these members is in the same scale then the mechanisms thickness. Possible errors introduced by this means have to be considered. This can be done for example by a subsequent 3D analysis of the mechanisms and comparison of the results.

In this work the original *mechtop* code was drastically expanded upon. The improvements and results obtained with the extended code will be outlined in the next chapter.

3 Development of the Optimization Code

In order to synthesize compliant mechanism ribs for a droop nose application in the project MILAN, the original *mechtop* code is extended by multiple functionalities. First, the FE solver and various functions in the optimization process are modified, to allow also calculations on non-regular mesh geometries. Furthermore, for mesh generation the commercial preprocessor of *Abaqus* shall be used, necessitating also of the generation of an interface between the *mechtop* code and *Abaqus*. Then the path-generation formulation for compliant mechanism synthesis introduced in section 2.2 is implemented, in order to achieve exact output displacements.

In addition, the MTOP method (see section 2.3) and PDE-based filtering techniques (see section 2.1.5.3) are implemented. Throughout this work, the code structure is improved and an optimization input file based on an *Excel*-sheet format is introduced. By the parallelization of the inner FE stiffness matrix integration loops, the use of more efficient assembly methods and various other measures the performance of the code is drastically increased.

The program, originally written on the 64-bit R2016a *MATLAB* version for *Windows*, is updated to the newer 64-bit R2018a version. Modifications, in order to achieve also portability to *Linux* systems are made. Data management of the software development project is based on *Git* using the software *SmartGit* and the *LRZ Gitlab*.

For testing and validation of the implementations, generic example problems are introduced. In this section, no detailed description of the software implementation is given, instead the important implementation steps are outlined based on the results of these example problems.

3.1 Generic Example Problems

In order to test the codes functionalities and to validate analysis results, simple problems are calculated during implementation. This generic example problems are introduced in this section.

3.1.1 Planar Cantilever Example Problem

For FE solver validation a planar cantilever example is analysed. This example is defined such, that high displacements and rotations occur and therefore nonlinear effects have an important influence. The schematic solid cantilever example problem is illustrated in figure 3.1. To the left the cantilever is clamped by fixed supports, and to the lower right corner the input load F_{in} is applied. For displacement-controlled FEA, the input displacement u_{in} has to be prescribed. A thickness of $T = 2$ mm and the material properties of steel are selected for

the cantilever.

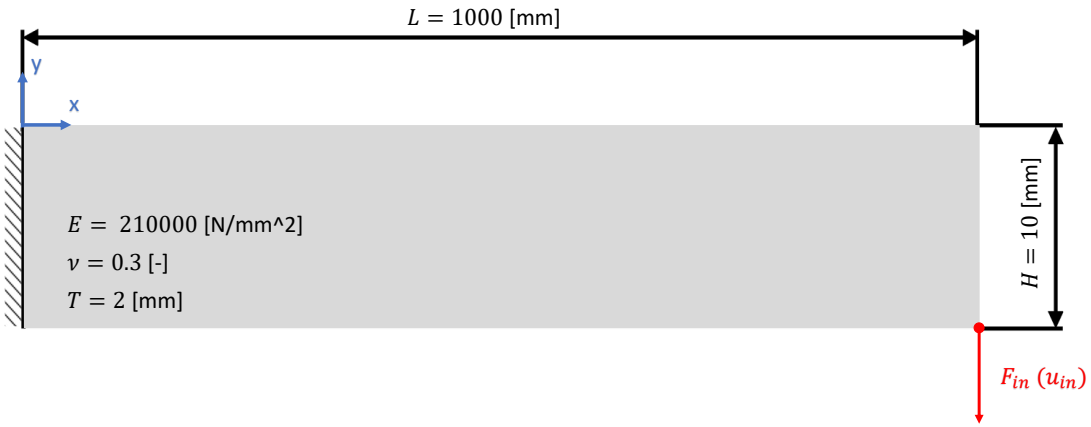

Figure 3.1: Planar cantilever example scheme

3.1.2 Path-Generation Example Problem

For the implementation of the path-generation formulation according to equation (2.32), a generic compliant mechanism synthesis problem is defined on a rectangular domain. This problem is illustrated schematically in figure 3.2. Fixed supports are provided in the lower left corner of the design space. At the input node, marked by the green dot, input displacements $u_{in,m}$ are applied in x-direction, resulting in output displacements $u_{out,m}$ at the red output node in the lower right corner.

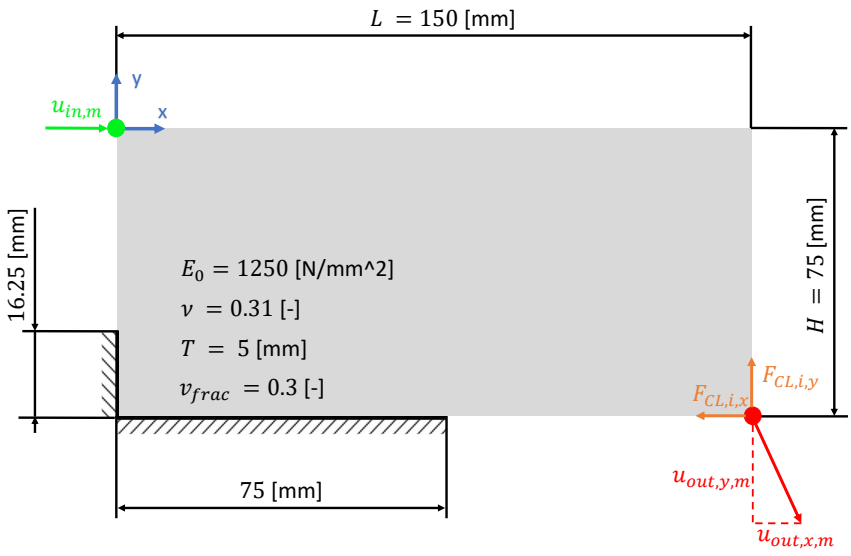

Figure 3.2: Sketch of the path-generation compliant mechanism example problem

The target kinematic has to be further defined for each precision point m, indicating the target output displacement values in x- and y-direction $u^*_{out,x,m}$ and $u^*_{out,y,m}$, corresponding to the input displacement $u_{in,m}$. The loads $F_{CL,i,x}$ and $F_{CL,i,y}$ are the nodal counter loads, applied in the load case i at the output node, in order to obtain stiff mechanisms. For $i = 0$ the counter loads are set to zero. One counter load should be applied against, the other one perpendicular to the output path. Material parameters of PA 11 are selected for this example, as indicated in figure 3.2.

In the following sections, results of the above-described example problems are presented for the new functionalities implemented to the *mechtop* code. The analysis is based on the mm-t-s unit system and its derived quantities according to table A.1.

3.2 Non Regular Mesh Modeling

The FE solver included in the original code uses isoparametric quadrilateral plane stress elements, as defined in figure A.1. By this means, all elements can be described equally in a parametric space. The real element geometry is then mapped onto the parameter space by shape functions (see equation (A.1)). In consequence, also the element stiffness matrices are integrated in the parameter space. Applying the described approach, the basic formulation of the FE solver is suited also for the analysis on non-regular meshes.

To generate complex non-regular FE meshes in 2D and 3D various software packages exist. In this work the preprocessor of the commercial FE suite *Abaqus* is used for that purpose. The main implementation effort lies in the creation of an interface between *MATLAB* and *Abaqus*. Therefore, the existing *Abaqus2Matlab* function (Papazafeiropoulos et al. 2017) that imports information contained in *Abaqus*-input-textfiles is modified. The resulting function allows not only to load the basic mesh information from *Abaqus*, but also support DOF's, loads and element sets can be defined in the *Abaqus* GUI and then imported to *MATLAB*. Limitations are that only quadrilateral elements in 2D can be imported and that only point loads and either symmetry or fixed boundary conditions can be considered. By the definition of element sets in *Abaqus* solid and void regions (eleNonDes_ active, eleNonDes_ passive), as well as regions where no stress constraints shall be applied (eleNonSConstr) can be defined. Here the names in brackets indicate the corresponding element set names.

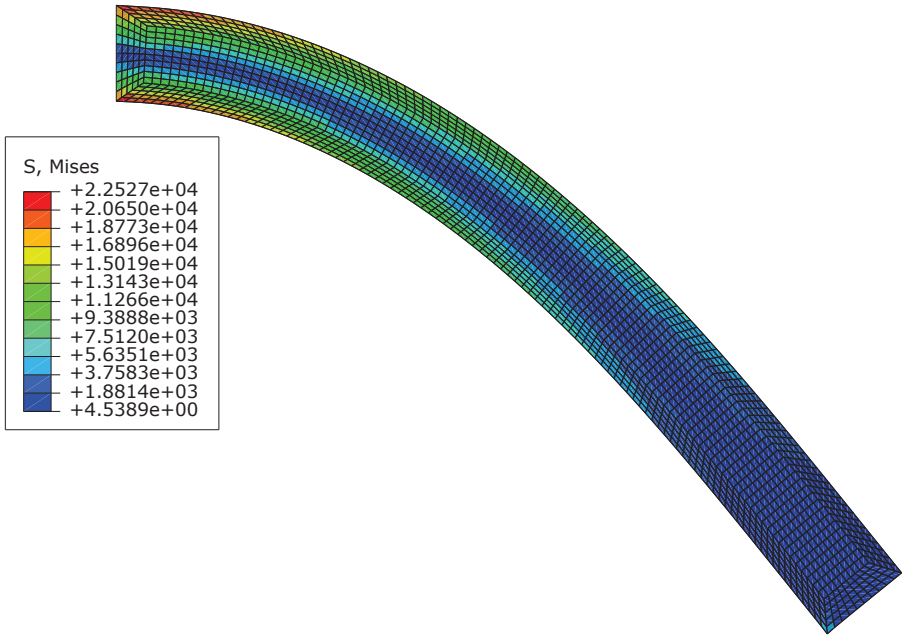

(a) *Abaqus* solution: $u_{y,min} = -592.18\,\text{mm}$, $\sigma_{vm,max} = 22527\,\text{N/mm}^2$

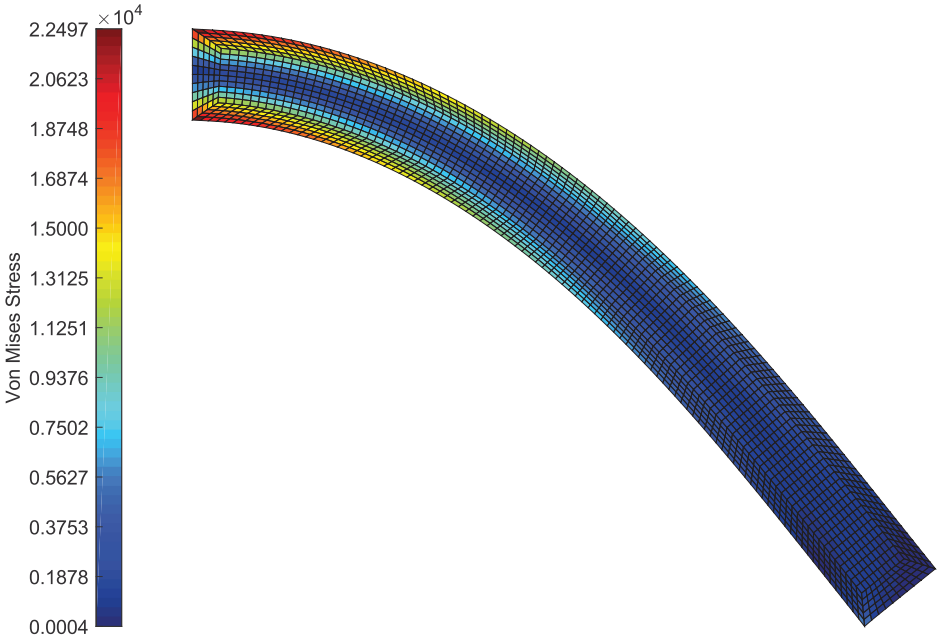

(b) *MATLAB* solution: $u_{y,min} = -592.8\,\text{mm}$, $\sigma_{vm,max} = 22497\,\text{N/mm}^2$

Figure 3.3: Comparison of geometric nonlinear cantilever example solutions with non regular FE mesh (2100 elements)

To validate the FE solver results on a non-regular mesh, the cantilever example in figure 3.1 is meshed by an o-shaped mesh and imported to *MATLAB*. Then the problem is calculated in

MATLAB and *Abaqus* for a force value of $F = 100000$ N. In *Abaqus* therefore the settings for geometric nonlinear analysis with automatic load incrementation, plane stress bilinear quadrilateral elements, a direct integration and a direct solver are chosen. Results are shown in figure 3.3. In (a) the deformation figure together with a von Mises stress contour plot for the *Abaqus*-result is illustrated, (b) shows the results of the *MATLAB* analysis. The depicted von Mises stresses are evaluated at the element centroids.

Both results deform similar in a smooth fashion although high deformations and rotations occur. The deviation for the minimum output displacement in y-direction $u_{y,min}$ is 0.1%. Also, the stress distributions match very well, with a deviation of the maximum von Mises stresses $\sigma_{vm,max}$ of 0.13%. The maximum stresses occur at the corners of the support area. The larger deviation for the stresses occurs due to the selected displacement based theory. Overall both results match well, which proves the validity of the MATLAB solver also for non-regular FE meshes.

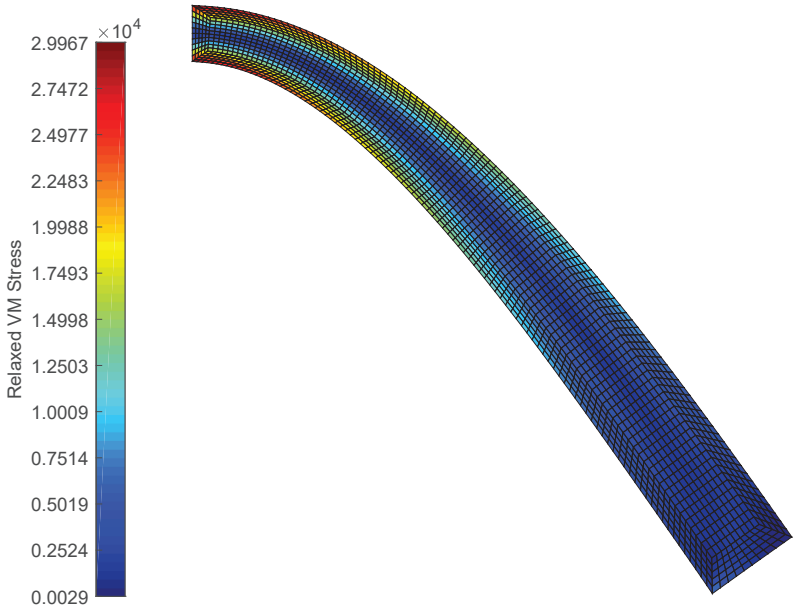

Figure 3.4: Linear *MATLAB* solution for the cantilever example with non regular FE mesh (2100 elements, $u_{y,min} = -950,413\,\mathrm{mm}$, $\sigma_{vm,max} = 29967\,\mathrm{N/mm^2}$)

To show the need for non linear FE analysis methods, the linear *MATLAB* solution for the same cantilever example is illustrated in figure 3.4. Therefore, also the linear FE solver was modified for non regular mesh modeling. One sees that in the linear solution displacements and stresses are overestimated. Furthermore, can rigid body rotations of the elements not be

modelled by the linear theory. Hence, the element volume increases in elements that undergo large rotations. By this means, high errors occur if linear analysis is used for problems with large deformations.

For topology optimization on non-regular meshes, the matrix based design variable storage used in the 88-line-code (Andreassen et al. 2011) has to be changed to a vector representation of the design variables. Furthermore, general filter expressions see section 2.1.5.1, accounting for different elements via element volume weighting and a more general weighting function H_{ei} (2.17), have to be introduced.

One of the first results of an output displacement minimizing compliant mechanism calculated on a non-regular mesh is shown in figure 3.5. The problem is calculated on an exemplary leading edge geometry, with fixed supports at the right side. The problem formulation of equation (2.7) is used. The input node is highlighted in green and the output node in red. The topology optimization leads to a discrete solid-void design on this non-regular mesh.

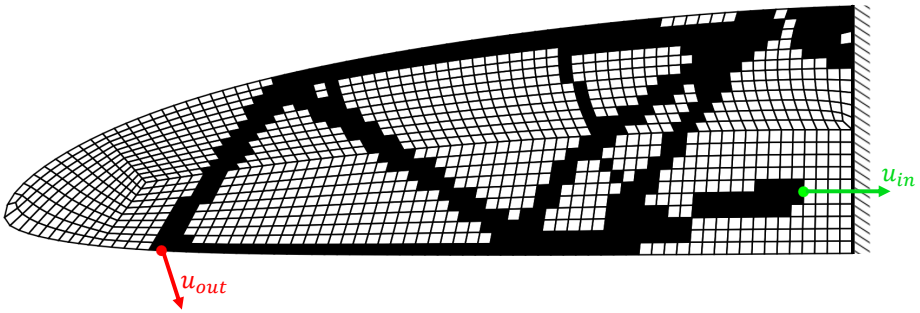

Figure 3.5: Example of an early compliant mechanism topology result on an airfoil-shaped designspace

For the further calculation of compliant mechanism ribs, the path-generation formulation is implemented in the next section.

3.3 Implementation of the Path-Generation Formulation

The theoretical background of the path-generation formulation was introduced in section 2.2. For implementation of the approach, the FE solver has to be modified first in order to use displacement control. This, in consequence, allows to perform input displacement steps and hence prescribe the mechanisms input displacement values $u_{in,m}$, corresponding to the output displacements $u_{out,m}$. Therefore, an extended residual formulation (see equation (2.34)) is introduced and solved by the implementation of the FE solver scheme illustrated in figure

A.3. Then the path generation objective function (2.31) and its sensitivity formulation derived in section 2.2.2 are implemented to the *mechtop* code. The formulation is applied to the example problem of figure 3.2. In a last step also the stress constraints introduced in section 2.4 are added to the path-generation formulation.

In the following section, results of the cantilever example (see figure 3.1) under displacement control are presented, in order to validate the implementation of the displacement-controlled FE solver. Moreover, the path-generation formulation is applied to the generic example problem of figure 3.2 for various input $u_{in,m}$ and target output displacements $u^*_{out,m}$ and for different counter load cases. At the end of this section stress constraint results of the path-generation example problem are discussed.

3.3.1 Displacement-Controlled FE Solver Validation

The displacement-controlled nonlinear FE implementation according to figure A.3 allows to choose the displacement of one DOF as control parameter. This displacement is defined by $\hat{U}_c$ in the control equation (2.33). Here the cantilever example defined in figure 3.1 is again calculated by application of the displacement u_{in} in y-direction at the lower right corner of the cantilever as control parameter. The same irregular mesh as in figure 3.3 is used.

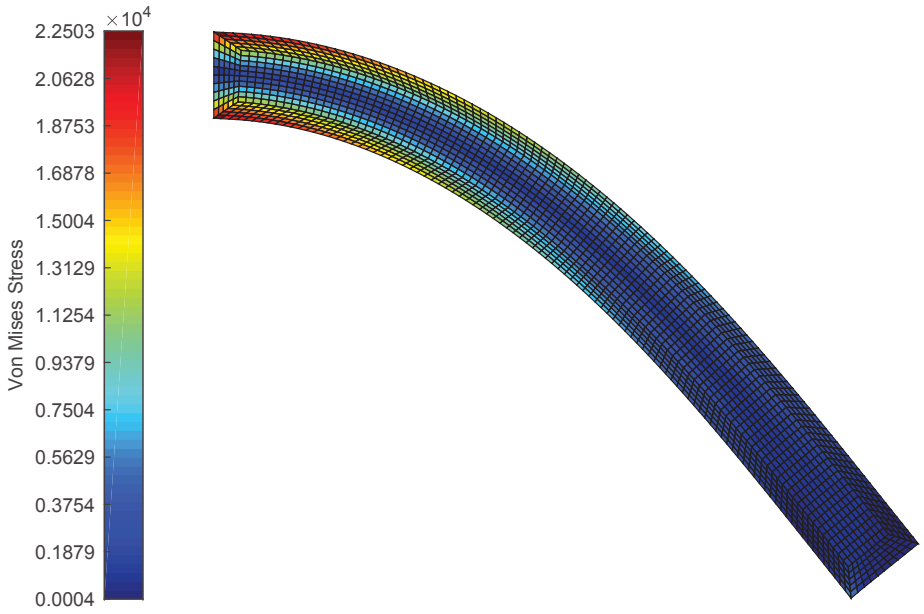

Figure 3.6: Displacement-controlled solution of the cantilever example with non-regular FE mesh (2100 elements, $\hat{U}_c = u_{in} = -556,072\,\text{mm}$, $F = 10^5\,\text{N}$)

The target displacement step value is set to $U_c = u_{in} = -556,072$ mm, corresponding to the lower right corners result of the previous load controlled example. For stability reasons a large input force $F = 10^8$ N is applied. Due to the displacement-controlled approach, the load incrementation parameter λ is then adjusted implicitly during the equilibrium iterations. This is done in order to obtain an input force $F_{in} = \lambda F$ that leads to a deformation in the controlled DOF, corresponding to the prescribed displacement step $\hat{U}_c$.

The results for the displacement-controlled FE approach are shown in figure 3.6, they match the previous load controlled result (see figure 3.3) very well. Displacement and von Mises stress fields are almost equal. The minimum output displacement is also $u_{y,min} = -592.8$ mm and the resulting load increment parameter $\lambda = 0.998\,10^{-4}$ leading again to an input force of approximately $F = 100000$ N.

3.3.2 Results of the Path-Generation Example Problem

In this section results of the generic example problem, introduced in figure 3.2, are presented. The problem is used during implementation for testing purposes and in order to gain experience about the practical behavior of the path-generation objective function formulation. Starting from the simple case of one precision point together with a single counter load case, results for different problem setups are discussed. Therefore, various input and output displacement combinations $u_{in,m}$ and $u_{out,m}$ are prescribed and also different counter load cases are applied. The results presented here, point out the capabilities of the newly implemented path-generation objective function.

All the results in this section are obtained by the use of density filtering see eq. (2.1.5.1) and the Heaviside projection method see eq. (2.22). The filter radius is selected to $r_{min} = 8\,\mathrm{mm}$ and the projection and update parameters are chosen to $\beta_0 = 1$, $\beta_{max} = 150$, $\eta = 0.3$ and $\tau = 30$. Adaptive design variable move limits according to section A.5 are applied starting from the value $\beta_{start} = 1$. Moreover, the SIMP parameter is set to $k = 3$ and the MMA asymptote control parameter is selected to $s = 1.07$. The energy interpolation scheme, defined in section A.4, is also used together with the parameters $\beta_1 = 500$, $\rho_0 = 0.01$ and $offset = 0$. For parameter studies related to these fundamental topology optimization parameters, the reader is referred to (Reinisch 2017).

As a first introductory problem, one single precision point is considered in the path-generation objective function. Material and geometry parameters are selected according to figure 3.2. The optimization target according to equation (2.32) is to find a mechanism topology, that

translates a selected input displacement of $u_{in} = 1.5\,\mathrm{mm}$ into the displacements $u^*_{out,x} = 1\,\mathrm{mm}$ and $u^*_{out,y} = -3\,\mathrm{mm}$ at the output node. Only volume constraints are applied.

(a) Solution topology

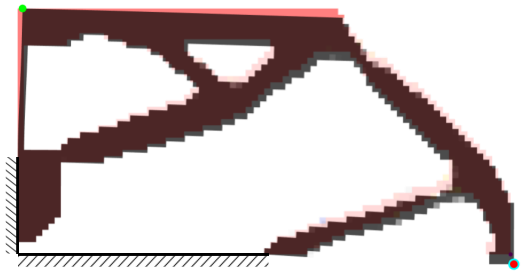

(b) Displacement figure without counter load, $u_{out,x} = 1\,\mathrm{mm}$, $u_{out,y} = -3.01\,\mathrm{mm}$

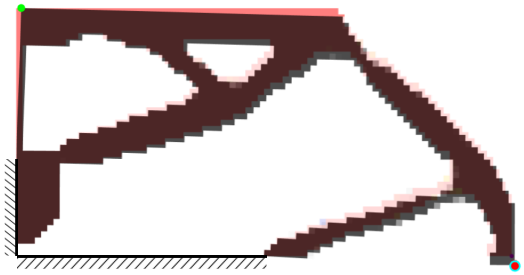

(c) Displacement figure with counter load, $u_{out,x} = 0.91\,\mathrm{mm}$, $u_{out,y} = -2.71\,\mathrm{mm}$

Figure 3.7: Solution of the path-generation example problem (80x40 elements, $u_{in} = 1.5\,\mathrm{mm}$, $u^*_{out,x} = 1\,\mathrm{mm}$, $u^*_{out,y} = -3\,\mathrm{mm}$)

In figure 3.7 the resulting topology and its displacement figures are illustrated. Due to the stiffness imposing effect of the counter load case, the resulting topology is a discrete black and white design. In fig. 3.7 (b) and (c) the displacement figures of the mechanism in comparison to the undeformed state are shown. Whereas in fig. 3.7 (b) no counter load is applied in fig. 3.7 (c) a counter load of $F_{CL,1,x} = -5\,\mathrm{N}$ and $F_{CL,1,y} = 15\,\mathrm{N}$ is acting. This also becomes evident in the displacement results. In fig. 3.7 (b) the target deformation is almost exactly reached and in fig. 3.7 (c) a maximum deviation in y-direction from the target of $0.29\,\mathrm{mm}$ occurs. The weighting factors α in equation (2.31) were selected to $\alpha_0 = 1$ for the case with no counter load and $\alpha_1 = 0.05$ for the counter load case. Corresponding to the values used by Pedersen et al. (2001). The objective function value at the end of the optimization is $\Phi = 4.9\,10^{-3}\,\mathrm{mm}^2$.

Overall the resulting mechanism in figure 3.7 satisfies the displacement requirements well. The input forces needed are $F_{in,1} = 9.8\,\mathrm{N}$ and $F_{in,2} = 43.5\,\mathrm{N}$ for fig. 3.7 (b) and (c), respec-

tively. By choosing a higher α weighting factor for the counter load case the target displacement deviation could be further reduced at cost of actuation force.

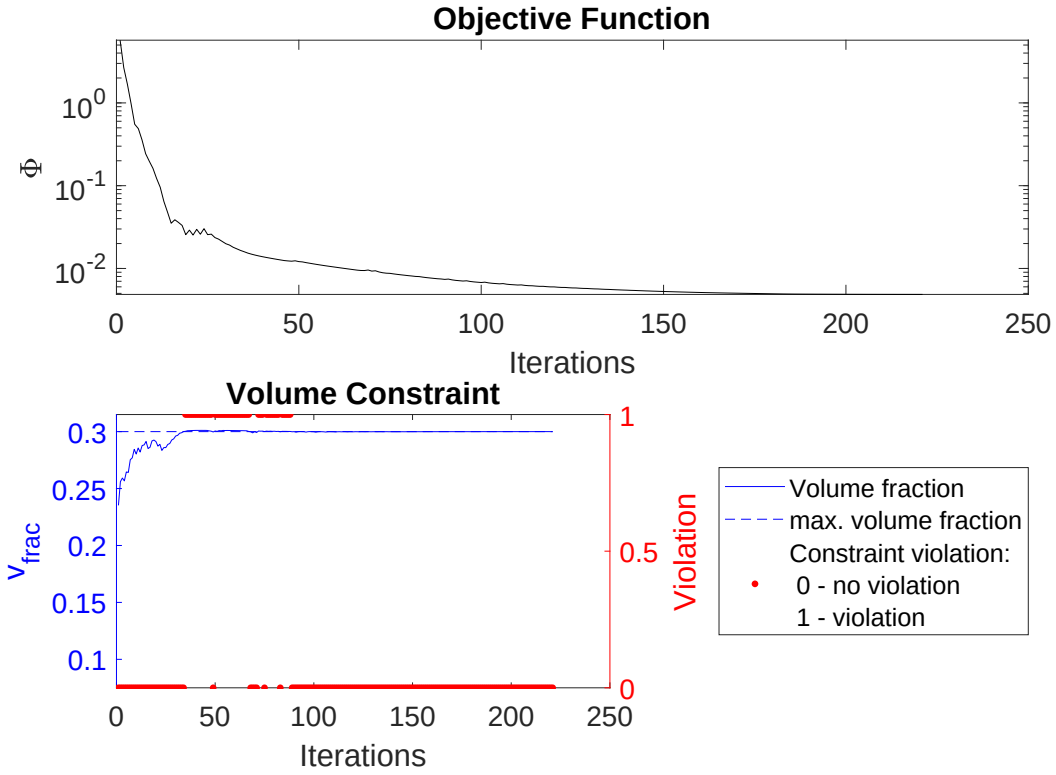

Figure 3.8: Convergence plots for the path generation example results in figure 3.7

In figure 3.8 the convergence plots for the objective function and constraints are shown. A smooth and initially steep descending convergence behavior can be observed for the objective function. Also the volume constraint converges well over the number of iterations, a feasible design with $v_{frac} = 0.3$ is obtained. The smooth convergence of the presented results proves the validity of the sensitivity formulation for displacement-controlled analysis derived in 2.2.2. Also the validity of the basic implementation of the path-generation formulation into the *mechtop* code is hereby proven.

Results of the generic example problem for different target output displacements u^*_{out} of one precision point are presented in figure 3.9. The same output displacement magnitude is applied in four different directions. In contrast to the prior example the results are obtained under consideration of two distinct counter load cases. The applied counter load cases and weighting factors are listed in table 3.1.

Table 3.1: Counter load definition for the path-generation example results in figure 3.9

Loadcase $i\,[-]$	**Weight** $\alpha\,[-]$	**x-Counterload** $F_{CL,x}\,[\mathrm{N}]$	**y-Counterload** $F_{CL,y}\,[\mathrm{N}]$
0	1	0	0
1	0.05	-5	15
2	0.05	15	-5

For the various output requirements four completely different solution topologies are obtained. All of them approximate the prescribed output displacement very closely. The topologies and their deformation figures for the case of no counter load are illustrated in figure 3.9. The result in (d) is calculated with reduced counter load weighting factors $\alpha_1 = \alpha_2 = 5\,10^{-3}$, because for the α parameter of table 3.1 no reasonable result was obtained. The problem in fig. 3.9 (d) can be understood as a double displacement inverter, representing a kinematically very complex task. This again results in high sensitivity to the optimization parameters. Although the same counter loads are used for every individual problem, all the solutions are discrete solid-void designs. In some results one node connected hinges can be observed. Their appearance could probably be avoided with an additional consideration of stress constraints.

Viewing figure 3.9, it can also be observed, that the input nodes move very differently in the various solutions. Whereas the x-displacement is equal for every solution $u_{in,x} = 4\,\mathrm{mm}$, y-displacements vary. This is because with the formulation used only one input DOF can be prescribed and therefore the displacement in y-direction of the input node is free. In order to prescribe linear input motion a support in the free input DOF could be defined. This has the same effect as a prescribed input displacement of $u_{in,y} = 0\,\mathrm{mm}$ for multiple DOF input control.

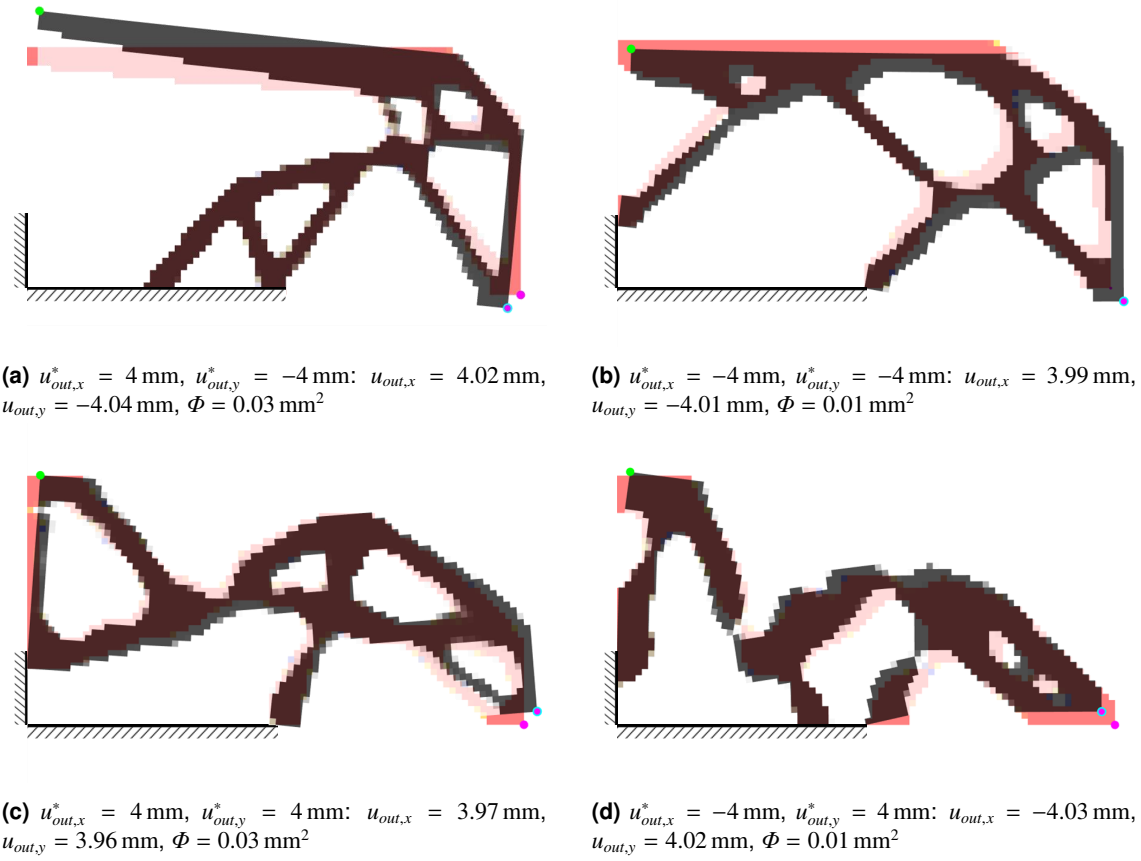

(a) $u^*_{out,x} = 4\,\text{mm}$, $u^*_{out,y} = -4\,\text{mm}$: $u_{out,x} = 4.02\,\text{mm}$, $u_{out,y} = -4.04\,\text{mm}$, $\Phi = 0.03\,\text{mm}^2$

(b) $u^*_{out,x} = -4\,\text{mm}$, $u^*_{out,y} = -4\,\text{mm}$: $u_{out,x} = 3.99\,\text{mm}$, $u_{out,y} = -4.01\,\text{mm}$, $\Phi = 0.01\,\text{mm}^2$

(c) $u^*_{out,x} = 4\,\text{mm}$, $u^*_{out,y} = 4\,\text{mm}$: $u_{out,x} = 3.97\,\text{mm}$, $u_{out,y} = 3.96\,\text{mm}$, $\Phi = 0.03\,\text{mm}^2$

(d) $u^*_{out,x} = -4\,\text{mm}$, $u^*_{out,y} = 4\,\text{mm}$: $u_{out,x} = -4.03\,\text{mm}$, $u_{out,y} = 4.02\,\text{mm}$, $\Phi = 0.01\,\text{mm}^2$

Figure 3.9: Solutions of the path-generation example problem for various target output displacements (80x40 elements, $u_{in} = 4\,\text{mm}$)

As a next step multiple precision points can be considered in the path-generation formulation. Therefore, the problem in figure 3.2 is used again. Counter loads are applied as previously according to table 3.1 and four precision points are defined in table 3.2. The output path, described by the precision points, is selected nonlinear, in order to generate a challenging path-generation topology optimization task.

Table 3.2: Precision point definition for the path-generation example in figure 3.10

Precision Point $m\,[-]$	**Input Displacement** $u_{in,x}\,[\text{mm}]$	**x-Target Output** $u^*_{out,x}\,[\text{mm}]$	**y-Target Output** $u^*_{out,y}\,[\text{mm}]$
1	2	2	-2
2	4	4	-4
3	6	6	-5
4	8	8	-5

Figure 3.10 illustrates the deformation figures for the solution topology of the four precision point problem. The final objective function value of $\Phi = 0.5$ is notably higher than for the single precision point solutions presented in figure 3.9. The mechanism has to find a compromise in order to approximate the various precision points prescribed.

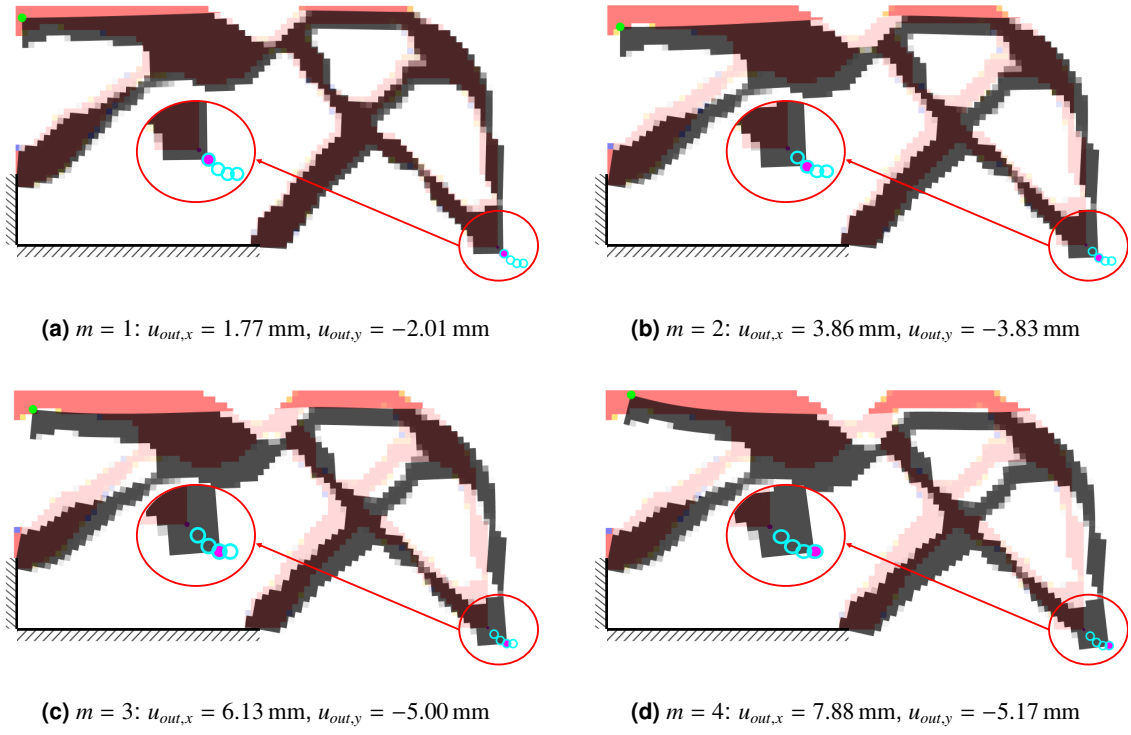

(a) $m = 1$: $u_{out,x} = 1.77\,\text{mm}$, $u_{out,y} = -2.01\,\text{mm}$

(b) $m = 2$: $u_{out,x} = 3.86\,\text{mm}$, $u_{out,y} = -3.83\,\text{mm}$

(c) $m = 3$: $u_{out,x} = 6.13\,\text{mm}$, $u_{out,y} = -5.00\,\text{mm}$

(d) $m = 4$: $u_{out,x} = 7.88\,\text{mm}$, $u_{out,y} = -5.17\,\text{mm}$

Figure 3.10: Solutions of the path-generation example problem with multiple precision points (80x40 elements, $\Phi = 0.5\,\text{mm}^2$)

From (a) to (d) in figure 3.10 it can be observed, how the mechanism output node follows the prescribed path. For the case shown with no counter load, the output displacements come really close to their target values. Looking at the input node, it is seen that in fig. 3.10 (a) and (b) a linear motion takes place. The mechanism forms a parallelogram-like structure, which tilts to produce a linear output motion. In fig. 3.10 (c) and (d) then a form of locking of the tilting motion is observed. A further increase of input load causes the member to the upper left to bend. This bending again induces a rotation of the right mechanism section, leading to an output node displacement along the second nonlinear part of the output path.

Further parameter studies for the path-generation objective function formulation with respect to the weighting factor α and the input displacement magnitude u_{in} are discussed in sections 4.3.3 and 4.3.2.

The examples presented in this section outlined different applications of the path-generation objective function. The formulation can be used for the design of single output node mechanisms under consideration of various counter load cases. By this means, single precision point mechanisms for maximum accuracy of one final output displacement, as well as path-following mechanisms can be synthesized. The results presented in this section were obtained by implementation of the path-generation objective function to the *mechtop* code, they prove the functionality of the path-generation implementation.

3.3.3 Stress Constraint Path-Generation Problem Formulation

In this section, the path-generation formulation is further extended by stress constraints introduced in section 2.4. The resulting complete optimization problem formulation is described in equation (3.1).

$$
\begin{aligned}
\underset{\boldsymbol{\rho}}{\text{minimize}} \quad & \Phi = \sum_{i=0}^{2} \alpha_i \sum_{m=1}^{M} [\boldsymbol{u}_{out,m,i} - \boldsymbol{u}^*_{out,m}]^2 \\
\text{subject to:} \quad & \boldsymbol{R}(\boldsymbol{U}) = \boldsymbol{K}(\boldsymbol{U})\,\boldsymbol{U} - \lambda \boldsymbol{F} = \boldsymbol{0} \\
& g_{s,i}(\boldsymbol{\rho}) = \frac{\tilde{\sigma}_{PN}}{\sigma^*} - 1 \leq 0 \\
& g_v = \frac{V}{v_{frac} V_\Omega} - 1 \leq 0 \\
& \boldsymbol{0} \leq \boldsymbol{\rho} \leq \boldsymbol{1}
\end{aligned}
\tag{3.1}
$$

where $g_{s,i}$ corresponds to a stress constraint for the load case i in the path-generation objective function. This problem formulation is applied to the generic path-generation example problem of figure 3.2. Only stress constraints for the first counter load case $i = 1$ are considered. The same optimization parameters and filter methods as in the example of figure 3.7 are applied.

Displacement figures and von Mises stress distributions for the unconstrained and for two stress constrained solutions are illustrated in figure 3.11. In (a) the stress distribution of the unconstrained solution is shown. The maximum occurring von Mises stress is $\sigma_{vm,max} = 7\,\mathrm{N/mm^2}$ in the localized hinge region to the lower left. In consequence, the maximum allowable stress constraint values σ^* for the solutions in fig. 3.11 (b) and (c) are chosen lower than this value.

(a) Displacement figure and stress distribution for the unconstrained solution according to figure 3.7: $\Phi = 4.9\,10^{-3}\,\mathrm{mm}^2$, $\sigma_{max} = 7\,\mathrm{N/mm}^2$

(b) Displacement figure and stress distribution for $\sigma^* = 5\,\mathrm{N/mm}^2$: $\Phi = 1.88\,10^{-2}\,\mathrm{mm}^2$, $\tilde{\sigma}_{PN,max} = 4.96\,\mathrm{N/mm}^2$

(c) Displacement figure and stress distribution for $\sigma^* = 2\,\mathrm{N/mm}^2$: $\Phi = 3.71\,\mathrm{mm}^2$, $\tilde{\sigma}_{PN,max} = 2\,\mathrm{N/mm}^2$

Figure 3.11: Stress constraint solutions of the path-generation example problem (80x40 elements)

In figure 3.11 (b) and (c) it can be observed, that the stress constraint problem formulation of equation (3.1) effectively limits the stress values. In both cases the constraint is not violated. Local hinge regions are transferred to distributed compliant flexures and by this means the stress distribution is smoothed. However, the objective function values Φ increase, with decreasing stress constraint values. This especially becomes evident in the result fig. 3.11 (c),

where even for the depicted case of zero counter load, the target displacement is only badly reached.

The results in figure 3.11 show, that also for the path-generation objective function the stress constraint formulation can be successfully applied. Multiple stress constraints can be introduced for the various load cases within path-generation problems.

3.4 Implementation of the Partial Differential Equation Based Filtering Techniques

Partial differential equation (PDE) based filtering techniques were introduced in section 2.1.5.3. Especially for topology optimization on large FE meshes filtering processes consume high amounts of storage and computational resources. PDE-based filters use the existing FE mesh discretization to generate the spatial filtering information and can thereby notably reduce the computational cost. In this work, the standard density filter as well as its combination with the Heaviside projection methods, discussed in sections 2.1.5.1 and 2.1.5.2, are modified to a PDE-based variant. Therefore, the finite element equations explained in 2.1.5.3 are implemented to the *mechtop* code, based on the regular mesh formulation used in an extension of the 88-line *MATLAB* code (Andreassen et al. 2011).

(a) Standard filter: $n_{iter} = 451$, $\Phi = 5.8\,10^{-3}\,\mathrm{mm}^2$, $t = 4790.5\,\mathrm{s}$

(b) PDE-based filter: $n_{iter} = 322$, $\Phi = 5.6\,10^{-3}\,\mathrm{mm}^2$, $t = 3331.8\,\mathrm{s}$

Figure 3.12: Comparison of solution topologies for standard and PDE-based density filter (320x160 elements, $r_{min} = 8\,\mathrm{mm} \mathrel{\hat{=}} r = 2.31\,\mathrm{mm}$)

In this section, the PDE-based filter is compared to the standard filter implementation. Therefore, the single precision point example problem of figure 3.7 is calculated on a fine FE mesh (320x160 elements). A density filter together with Heaviside-projection according to equation (2.22) is used. The optimization parameters are selected according to section 3.3.2, with exception of the MMA asymptote control parameter, which in this case is set to $s = 1.05$. The results are shown in figure 3.12.

In figure 3.12 it is seen that the use of PDE-based filtering methods only slightly influences the appearance of the solution topology. This is because the same filter radius is selected, applying equation (2.29). The method only represents an alternative way to calculate the weighting factors for the element densities in the element neighborhood $\mathbb{N}_e$. It is also observed that the solution using the PDE-based filter converges in fewer iterations n_{iter}. A reason for the faster convergence could be the different weighting factor distribution in radial direction, that results from the convolution integral. An exemplary weighting function distribution for the PDE-based filter is illustrated in figure 3.13.

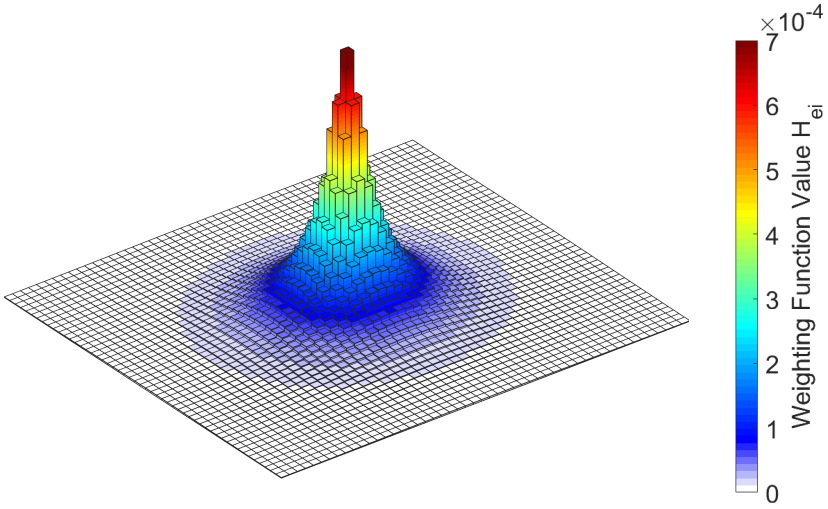

Figure 3.13: Visualization of the weighting function H_{ei} for the PDE-based filter (51x51 elements, $e = 1301$)

Whereas the standard filter in figure 2.9 has a linear cone-shaped weighting function, the weighting function of the PDE filter is bell shaped. In the presented example this steeper descending distribution is beneficial to limit density oscillations in the solid-void transition areas close to convergence. Furthermore, the thickness of this transition areas is reduced by the new distribution of the weighting factors. The objective function values Φ are almost equivalent for both results.

Looking at the time per iteration, the PDE filter with 10.35 seconds per iteration is slightly faster than the standard formulation, which takes 10.62 seconds. The difference comes on one hand from the filter initialization (generation of filtering information), which is 98% faster. And on the other hand from the time of every single filtering operation, which reduces by approximately 50% for the PDE filter. For the reason that these operations only represent a small share of the total computational cost, the absolute speed up is with a value of 2.5% relatively small. The FE

analysis and the optimization process represent the largest share of computational cost, but especially for topology optimization on larger meshes or with high filter radius values the PDE-based filtering methods also provide significant acceleration potential. All the computation times indicated are obtained on the machine configuration listed in Appendix A.2.

3.5 Implementation of the Multiresolution Topology Optimization Method (MTOP)

The basic concept of the MTOP approach is described in section 2.3. By introduction of a sub mesh for the design variables, existing FE information can be used to obtain higher resolution topologies at comparable computational cost.

In this work the method is implemented to the *mechtop* code for the case of equal design variable and density discretization. A remeshing method based on the isoparametric shape functions is introduced. Thereby, the geometric design variable element information is generated from the original FE mesh coordinates. According to figure 2.11 the introduced design variable mesh divides each FE element into subelements. The FE solvers are modified in order to save the fractions of the element stiffness matrices $\boldsymbol{K}_{e0,gp}$, related to the Gauss integration points and needed for SIMP interpolation see eq. (2.43). The FE analysis itself is still conducted on the coarse FE mesh and hence remains unchanged. The sensitivity analysis can be exemplarily defined by equation (2.1.3) with the finer design variables $\rho_{e,gp}$ replacing ρ_e and the stiffness matrices $\boldsymbol{K}_{e0,gp}$ replacing $\boldsymbol{K}_{e,gp}$. Existing filter methods are applied together with the MTOP formulation.

The benefit of the method is illustrated in figure 3.14, where three solutions of the generic path generation problem are listed. Optimization parameters and problem definition are selected according to the solution in figure 3.7 and the PDE-based variant of the density filter with Heaviside projection (see eq. (2.22)) is used.

It is seen that the resulting topologies in figure 3.14 appear similar, only to the lower left of (b) no localized hinge is introduced. In (a) a standard topology optimization on a coarse 80x40 element mesh is performed. This leads to a pixel like contour of the solution topology. In fig. 3.14 (b) the MTOP method is applied using the same FE mesh as in fig. 3.14 (a) and four subelements for the design variables. It can be observed, that the results shape appears much smoother. The objective function value in fig. 3.14 (b) is slightly smaller than in fig. 3.14 (a). Furthermore, the computation of (b) takes 70% more time as for (a). It also needs more iterations n_{iter} to converge. The difference in time per iteration is with 0.912 seconds for

(a) and 1.164 seconds for the MTOP solution only at around 28%. Figure 3.14 (c) shows a standard topology optimization result on a finer 160x80 FE mesh, in order to obtain the same resolution as the MTOP result in fig. 3.14 (b). The computational cost for the result in fig. 3.14 (c) is with 3.271 seconds per iteration, corresponding to 359% of fig. 3.14 (a), by far the highest. The indicated computational times refer to the machine configuration according to Appendix A.2.

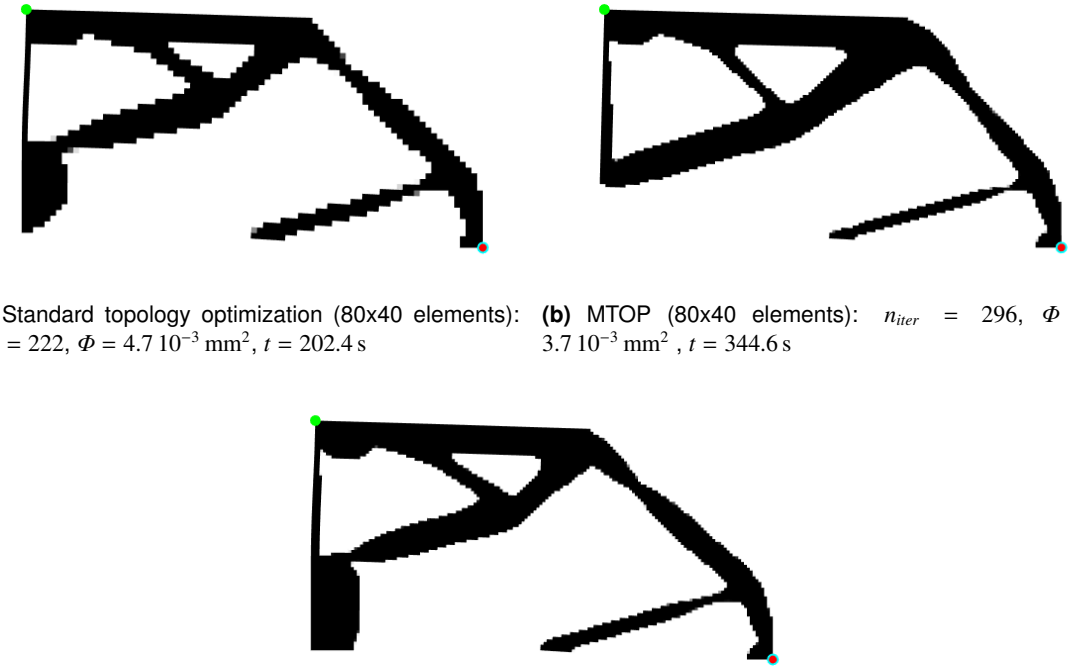

(a) Standard topology optimization (80x40 elements): $n_{iter} = 222$, $\Phi = 4.7\,10^{-3}\,\mathrm{mm}^2$, $t = 202.4\,\mathrm{s}$

(b) MTOP (80x40 elements): $n_{iter} = 296$, $\Phi = 3.7\,10^{-3}\,\mathrm{mm}^2$, $t = 344.6\,\mathrm{s}$

(c) Standard topology optimization (160x80 elements): $n_{iter} = 259$, $\Phi = 5\,10^{-3}\,\mathrm{mm}^2$, $t = 847.1\,\mathrm{s}$

Figure 3.14: Comparison of standard and multiresolution (MTOP) topology optimization results

In figure 3.14 the deformed state of the result topologies is shown. Comparing the solution times of (b) and (c), the big advantage of the MTOP scheme becomes evident. With only minor computational overhead with respect to the standard solution a high resolution topology can be synthesized, whereas the same output resolution is very expensive by means of a standard topology optimization method. Using MTOP methods one has to consider that the physics of the structure are still modelled on the underlying coarse FE mesh. Therefore, it is important to choose this mesh fine enough, in order to model the real structural behavior sufficiently accurate.

Also for stress constraint formulations the MTOP method can be applied. Therefore, stresses $\boldsymbol{\sigma}_{e,gp}$ are calculated corresponding to equation (A.14) at each Gauss integration point gp. This is done, by evaluation of the element strain vector $\boldsymbol{E}_{GL}$ at the respective Gauss point coordinates. With the stresses $\boldsymbol{\sigma}_{e,gp}$ then for each subelement the von Mises stress $\sigma_{vm,e,gp}$ and its relaxation term $\sigma_{e,gp} = \overline{\tilde{\rho}}^{q}_{e,gp}\sigma_{vm,e,gp}$ are calculated. Further the p-norm stress $\tilde{\sigma}_{PN}$ and the stress constraint function g_s can be evaluated according to their definition in section 2.4, with σ_{sum} defined by:

$$\sigma_{sum} = \sum_{e}\sum_{gp} v_{e,gp} * \sigma^{p}_{e,gp} \quad with \quad {}_{e,gp} \in \mathbb{N}_{\sigma} \tag{3.2}$$

The sensitivities of g_s are also calculated similar to section 2.4. The equations for the MTOP approach now write as follows:

$$\frac{\partial g_s}{\partial \overline{\tilde{\rho}}_{e,gp}} = \frac{1}{\sigma^*} c\sigma_{sum}^{\frac{1}{p}-1} v_{e,gp}\sigma_{e,gp}^{p-1} q\overline{\tilde{\rho}_{e,gp}}^{q-1}\sigma_{vm,e,gp} + k(E_0 - E_{min})\overline{\tilde{\rho}_{e,gp}}^{k-1} * \boldsymbol{\lambda}^{\sigma\mathbf{T}} * \boldsymbol{K}_{0e,gp}(\boldsymbol{u}_e) * \boldsymbol{u}_e \tag{3.3}$$

The adjoint vector $\lambda^{\sigma\mathbf{T}}$ is obtained as previous from the solution of the adjoint problem:

$$\boldsymbol{K}_T^{\mathbf{T}} * \boldsymbol{\lambda}^{\sigma} = -\frac{\partial g_s}{\partial \boldsymbol{U}}^{\mathbf{T}} \tag{3.4}$$

which is solved after element wise calculation of $\frac{\partial g_s}{\partial \boldsymbol{u}_e}$.

$$\frac{\partial g_s}{\partial \boldsymbol{u}_e}^{\mathbf{T}} = \sum_{gp} \frac{c\sigma_{sum}^{\frac{1}{p}-1} v_{e,gp}\sigma_{e,gp}^{p-1}\overline{\tilde{\rho}_{e,gp}}^{q}}{\sigma^*\sigma_{vm,e,gp}} * \boldsymbol{B}_{L,gp}^{\mathbf{T}} * \overline{\boldsymbol{F}}_{gp} * \boldsymbol{C}_{VK} * \boldsymbol{V} * \boldsymbol{\sigma}_{e,gp} \tag{3.5}$$

In equation (3.5) the terms $\boldsymbol{B}_{L,gp}$ and $\overline{\boldsymbol{F}}_{gp}$ are calculated for the corresponding Gauss point (gp) coordinates.

A stress constraint result obtained by the use of the MTOP approach is illustrated in figure 3.15 (b). The previous example of figure 3.14 is therefore calculated under consideration of stress constraints. Like in section 3.3.3 the stress constraints are applied to the counter load case.

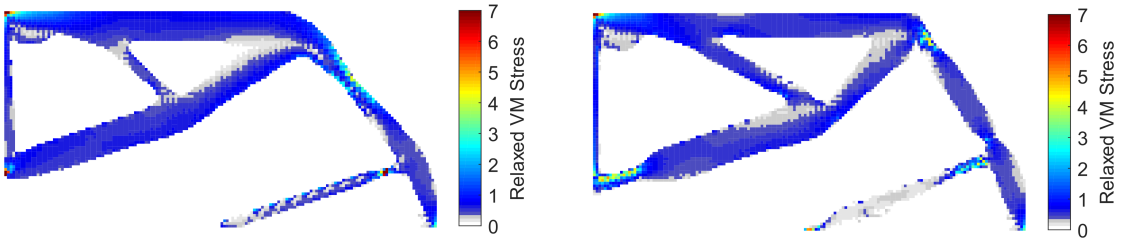

(a) Unconstrained solution: $\sigma_{max} = 11.33\,\mathrm{N/mm^2}$ $\Phi = 3.7\,10^{-3}\,\mathrm{mm^2}$

(b) Stress constrained solution $\sigma^* = 5\,\mathrm{N/mm^2}$: $\Phi = 5.4\,10^{-3}\,\mathrm{mm^2}$, $\tilde{\sigma}_{PN,max} = 5\,\mathrm{N/mm^2}$

Figure 3.15: Stress constrained multiresolution topology optimization (MTOP) (80x40 elements, 4 subelements)

In figure 3.15, long thin hinge regions can again be observed, which successfully reduce the maximum stress values. The stress constraint is active. Compared to the unconstrained solution to the left, the mechanism in (b) is slightly less performing by means of objective function Φ. The result obtained shows that the MTOP method can also be successfully applied for stress constraint topology optimization problem formulations.

4 Topology Optimization of Compliant Mechanism Ribs

The topology optimization methods introduced and implemented in the previous sections are applied in this thesis in order to generate compliant mechanism ribs for the project *MILAN*. The projects adaptive leading edge wing concept is described in figure 1.2. It consists of a highly anisotropic shell in the wings nose section, deformed by rib shaped compliant mechanisms. In contrast to prior work, geometric nonlinear FE analysis methods and also stress constraint formulations are applied for the synthesis of the mechanism ribs. The main focus of this work is to assess the suitability of the earlier introduced methods for the practical compliant mechanism rib problem. Therefore, simplified mechanisms for a new compound compliant mechanism rib concept are designed.

At the beginning of this section, the concept of stacked single input and output ribs is introduced. Then the modeling for the compliant mechanism design problem for this rib concept is described. At the end mechanisms for an exemplary wing section are generated and the results obtained are discussed.

4.1 Concept of Stacked Compliant Mechanism Ribs

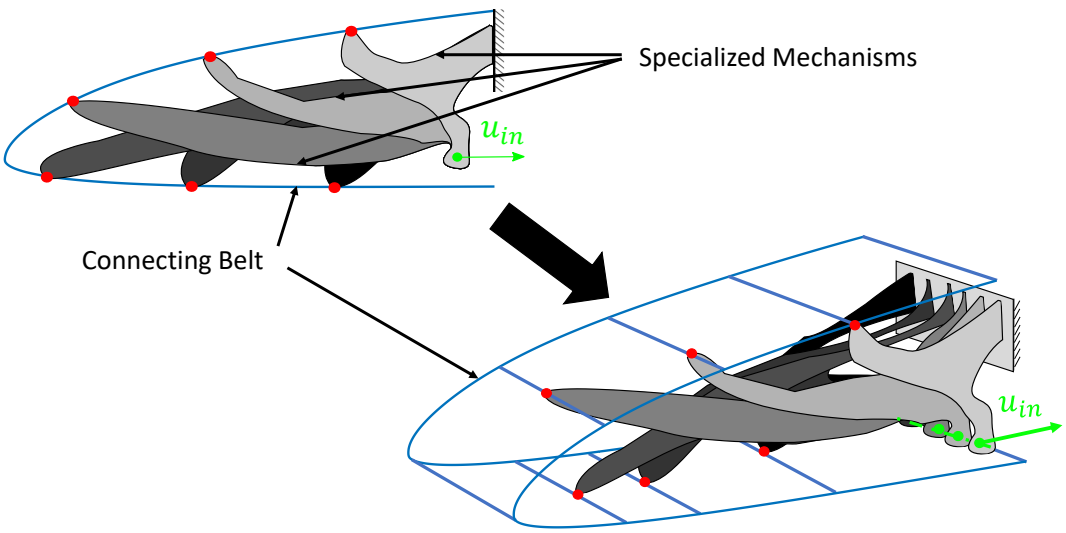

Figure 4.1: Concept of stacked compliant mechanism ribs

First demonstrators of shape morphing compliant mechanism leading edge ribs were designed in a prior work (Salehar 2015). As shown in figure 1.4, they consist of one integral mechanism, which has to satisfy all the different target deformation requirements along its

outer surface. The mechanisms were optimized by the use of linear finite element analysis. Therefore multiple control points along their outer contour were introduced and an objective function containing a least square error term was used. Apart from the error introduced by the use of small displacement analysis, it is assumed that waviness is also a result of the objective function formulation. Due to the fact that one mechanism needs to satisfy many target output displacements, only an approximative solution can be found. And with an increasing number of control points commonly the quality of this approximation deteriorates. Salehar (2015) therefore proposed another design approach using multiple specialized single input and output mechanisms for a reduced number of discrete control points. Because for the shell the shape morphing is close to its natural deformation, it is presumed that by this means the total mechanisms shape adherence could be improved.

The new concept is illustrated schematically in figure 4.1, in which six specialized mechanisms actuate six distinct control points highlighted in red. The individual mechanisms are stacked together in span direction and share a common fixed support section. All the output nodes are connected by a profile shaped belt structure, represented by the blue lines. By this means, the individual mechanisms are assembled to one rib, which again could easily be bonded on the flexible shell. Moreover it is also possible to manufacture these compound ribs within one single manufacturing process by the use of additive manufacturing techniques as for example selective laser sintering.

All the input nodes of the individual mechanisms in figure 4.1, marked by the green dots, are arranged on one axis. Therefore the mechanisms can be actuated equally by one actuator with the input displacement u_{in} and hence from an operational perspective there is no difference to the mechanisms integral counterpart. Due to the specialization less deviation of the control nodes target displacements will occur, because each mechanism has only one task and no compromise of objectives has to be found. Disturbance effects due to interaction between the single mechanisms can be partly considered by counter load cases, which impose a general robustness with respect to force disturbances. In section 4.3, various specialized mechanisms results for a stacked mechanism rib are presented.

4.2 Problem Modeling

In this work first compliant mechanisms for the stacked mechanism rib concept introduced in the previous section are optimized. These mechanisms are generated for an exemplary wing section with 550 mm chord length. According to figure 4.2, six control points are distributed

equally along the curve length of the profile nose section. The control points position is illustrated for the normal and the morphed airfoil state. For both cases the control points positions in terms of curve length on the profiles are equal. This means that no in plane stretching of the flexible shell structure occurs. Red arrows indicate the target output displacement vectors $\boldsymbol{u}^*_{out}$. For each of the control points a specialized compliant mechanism can be designed by the use of the path-generation objective function for a single precision point. The problem formulation generally equals to the generic example problem in figure 3.7.

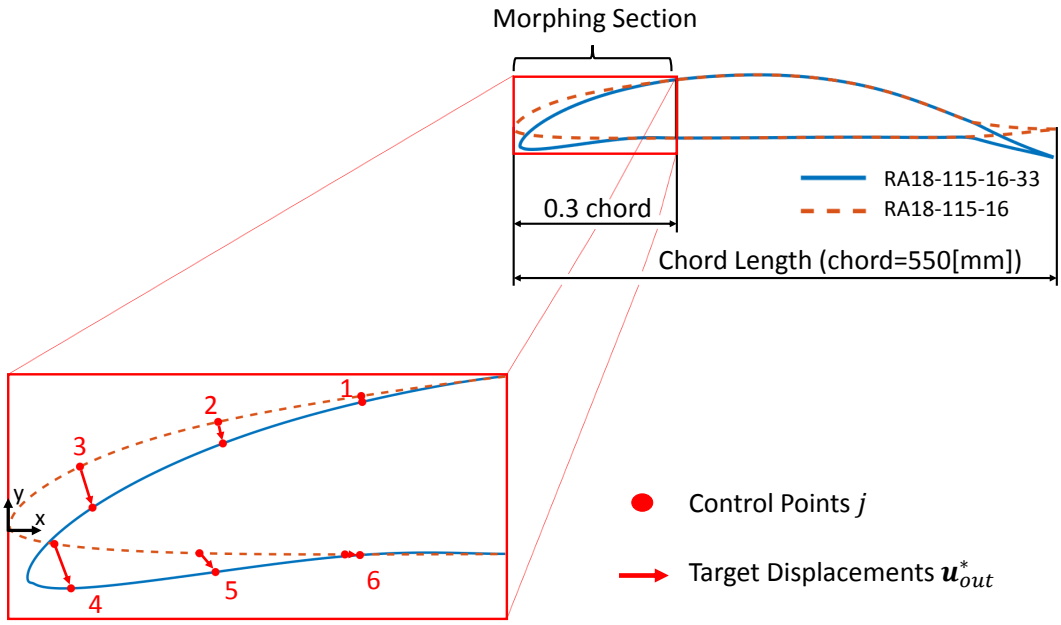

Figure 4.2: Mechanism control point distribution along the morphing profile section

In figure 4.2 the two optimized airfoil geometries for the wings high (RA18-115-16) and low speed (RA18-115-16-33) configurations are shown. The target values for the mechanism output displacements for the various control points are listed in table 4.1. By application of these displacements, the leading edge section is deformed in order to change between the two airfoil shapes.

Table 4.1: Target displacements u^*_{out} for the control points j of a stacked compliant mechanism rib according to figure 4.2

Control Point	$j\,[-]$	1	2	3	4	5	6
x-Target Output	$u^*_{out,x}\,[\mathrm{mm}]$	0.37	1.67	4.34	5.53	5.28	4.96
y-Target Output	$u^*_{out,y}\,[\mathrm{mm}]$	-2.02	-7.31	-13.80	-14.18	-5.67	0.07

The topology optimization problem is displayed schematically in figure 4.3, in which the case for control point number 4 is described. The fundamental problem setup is also equivalent for the calculation of mechanisms for other control points, therefore only the location of the output node has to be changed.

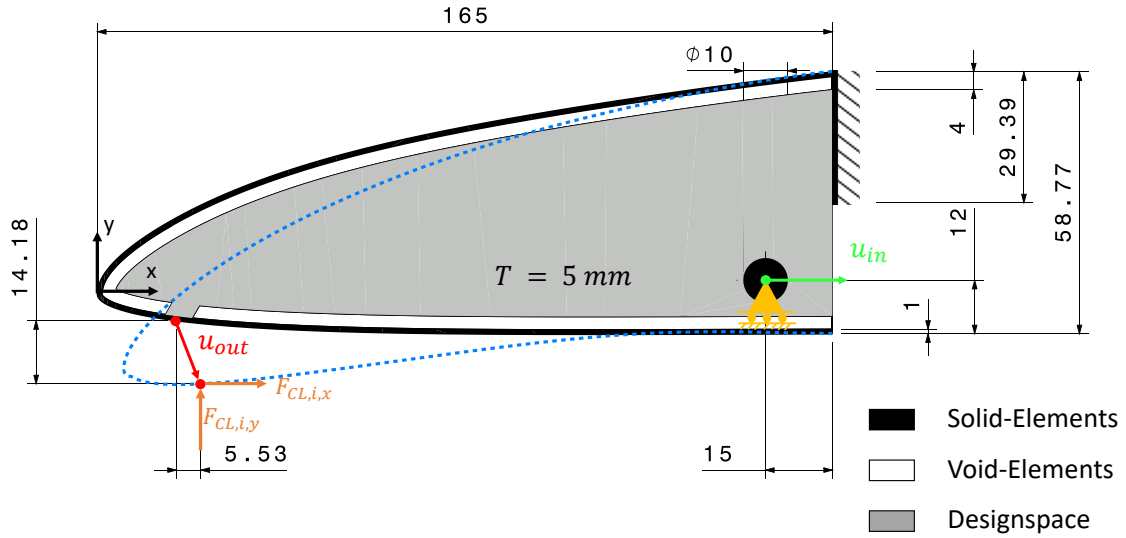

Figure 4.3: Compliant mechanism rib topology optimization problem scheme (control point $j = 4$)

In figure 4.3 the morphing nose section domain is illustrated. At the mechanisms input node, highlighted in green, an input displacement in positive x-direction is applied. At the output node, marked in red, the target output displacement u_{out} has to be reached according to table 4.1. Furthermore, counter loads F_{CL} are applied at the output node for the counter load cases of the path-generation objective function. A fixed support region for the mechanism is provided to the upper right, modeling its attachment to the spar. The y-DOF in the input node is also fixed, in order to ensure compatibility of the input node motions between the single stacked mechanisms. If this DOF would be free, different y-deflections of the individual mechanisms input nodes could result, causing a self locking effect of the assembled rib. It is assumed that the actuation can be designed stiff enough in y-direction, so that the reaction forces can be transferred without significant deformation of the actuator. A thickness of $T = 5\,\mathrm{mm}$ is selected for each individual mechanism based on prior experience gained by Salehar (2015).

The choice of the input node location and the input displacement direction is also based on the experience gained in Salehars Salehar (2015) prior work. For the integral ribs, the best results could be obtained by the application of input displacements in positive x-direction and

the input node positioned to the lower right of the design space. In contrast to the model for the integral compliant mechanism, here the fixed supports are provided only to the upper half of the right boundary. This is done in order to avoid instabilities in compressed elements. These instabilities arise, if fixed supports are positioned to close to the input node and hence the input displacement leads to a strong compression of the void or semi-dense elements in this area.

In figure 4.3 areas in three different colors can be observed. The grey section represents the design space, where material can be freely distributed during the optimization process. The black regions are regions of fixed solid material. They are located around the input node, in order to avoid instabilities and to provide a defined input section geometry, and along the outer profiles contour. The outer solid belt in this work is a first approximation of the collective behavior of the flexible shell and the connecting belt, which is connecting the single stacked mechanisms. The focus of this work is on the generation of early design phase topologies and on the testing of the newly implemented methods, no detailed modeling of this components is done.

The white areas next to the outer solid belt in figure 4.3 represent a prescribed void non design space. First optimizations showed that this non design space is necessary in order to avoid collisions between the developing topology and the outer belt. This collisions can not be considered by the model and must therefore be avoided. Furthermore without the introduction of a non design region the mechanisms connect in multiple areas to the outer belt, inhibiting the free deformation of the belt and causing kinks in the outer geometry. By this means, the single mechanisms objective is fulfilled, but the other control points solutions are disturbed. It was also observed that for too thin non design regions, single mechanism components can even cross the target profile contour, making the assembled solution worthless. The prescribed void region is interrupted close to the output node to allow the mechanism to connect to the output node.

The mechanism rib results presented in this work are all defined by the basic problem setup shown in figure 4.3. For optimization the path-generation objective function according to equation (2.31) is used. Aerodynamic loads act as counter loads. In the following subsections the used material, the calculation of the aerodynamic loads as well as the mesh discretization of the profile nose section are described.

4.2.1 Material

For the compliant mechanisms the high performance semi crystalline thermoplastic material polyether ether ketone (PEEK) is chosen. It has very good mechanical properties for a large temperature range and can be processed by additive manufacturing techniques. Material test results show a significant temperature dependency of PEEK's material properties. In this work material properties resulting from a in-house test conducted at the Institute for Lightweight Structures at TUM are used (Mahl et al. 2016). The stress-strain curves for four different temperatures are displayed in figure 4.4. A clearly nonlinear material behavior can be observed.

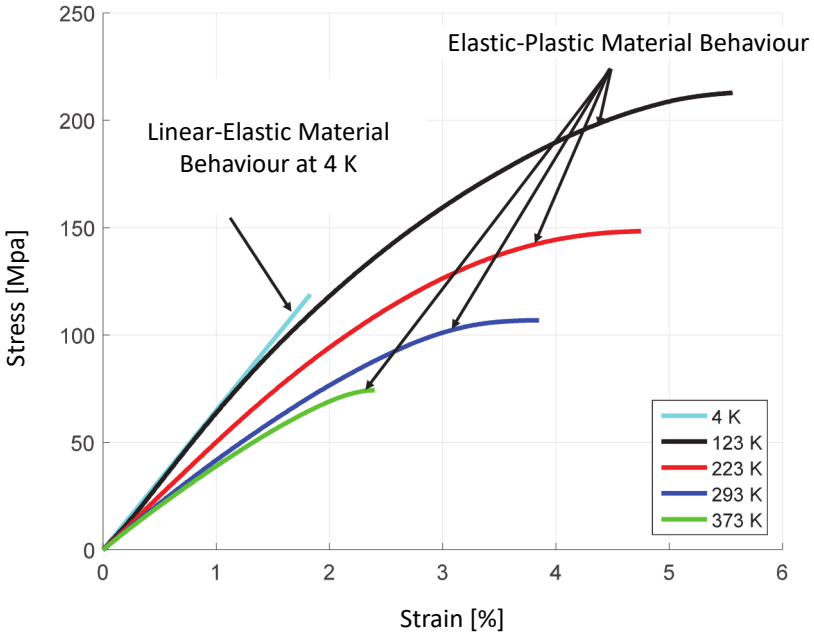

Figure 4.4: Stress-strain curves for PEEK at different temperatures (Mahl et al. 2016)

Due to the fact that nonlinear material behavior can not yet be modelled by the implemented FE solver, linear-elastic material is assumed. This simplification might be valid for very small strains but in compliant mechanism design, where also high strains occur the error should not be neglected. Hence, in future work the implementation of nonlinear material models must be considered.

Table 4.2: Material parameters for PEEK at $20\,[°\mathrm{C}]$

Young's Modulus	$E_{PEEK}\,[\mathrm{N/mm^2}]$	4232
Poisson's Ratio	$\nu_{PEEK}\,[-]$	0.36
Tensile Strength	$R_{m,PEEK}\,[\mathrm{N/mm^2}]$	100

In this thesis the material parameters for a temperature of $20\,°\mathrm{C}$ are used together with the St. Venant-Kirchhoff material model in equation (A.5). The material parameters are listed in table 4.2.

4.2.2 Aerodynamic Loads

The compliant mechanism ribs need to transfer aerodynamic loads from the flexible wings nose section to the spar. They also need to be stiff, in order to avoid high deformations and resulting deviations from the airfoils target shape. To ensure this, in topology optimization the aerodynamic loads acting on the mechanisms are applied as counter loads for the path-generation formulation.

It is planned to design the wing with a rib every half a meter of span and hence the load on one compliant mechanism rib is estimated for this reduced wing section. Two load cases, one for the morphed and one for the original airfoil, are considered. Therefore, load factors according to the manoeuvring envelope prescribed by the certification standard (*CS-22* 2008), are applied. The load factors are $n = 5.3$ at the maximum speed for extended flaps of $\mathrm{v}_{FE} = 231\,\mathrm{km/h}$ in the morphed state and $n = 4$ at the design maximum speed of $\mathrm{v}_A = 312\,\mathrm{km/h}$ for the high speed profile. With an aircraft mass of $m = 600\,\mathrm{kg}$, the wing area of $A = 8.6\,\mathrm{m^2}$ and the air density of $\rho = 1.225\,\mathrm{kg/m^3}$ given, the coefficients of lift C_L can be calculated using the following equation:

$$C_L = \frac{2\,n\,m\,g}{\rho\,\mathrm{v}^2\,A} \tag{4.1}$$

For the exemplary wing section with $chord = 550\,\mathrm{mm}$ chord length, considered in this work, the Reynolds numbers are derived as

$$Re = \frac{\mathrm{v}\,chord}{\nu} \tag{4.2}$$

where $\nu = 1.53\,10^{-5}\,\mathrm{m^2/s}$ is the assumed air viscosity. The resulting Reynolds numbers Re and coefficients of lift are listed in table 4.3.

Table 4.3: Parameters for the evaluation of the pressure distribution in *XFOIL*

Airfoil State	**Profile**	**Reynolds Number** $Re\,[-]$	**Coefficient of Lift** $C_L\,[-]$
morphed	RA18-115-16-33	$2.31\,10^6$	1.438
unmorphed	RA18-115-16	$3.12\,10^6$	0.595

This parameters are used together with the profile geometry data to calculate the pressure distribution coefficient C_p along the profile. This is done by the use of the program *XFOIL*. In the following the C_P values can be integrated along the profiles contour in order to obtain the total force acting on the airfoil.

For the stacked compliant mechanism concept each single mechanism carries a part of the aerodynamic load. It is assumed that each mechanism is loaded mainly by the aerodynamic loads acting close to its control point. Therefore, the profile nose is divided into sections, whose resulting aerodynamic loads are assigned as concentrated forces to the corresponding mechanisms.

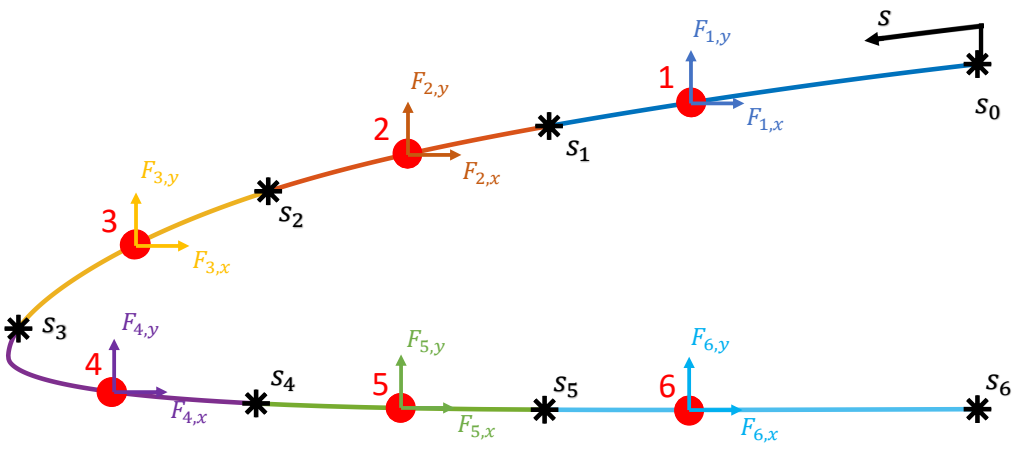

Figure 4.5: Division of the wings morphing nose section contour for aerodynamic load calculation

The division of the nose section is illustrated in figure 4.5. The control points, corresponding to the individual mechanisms output nodes, are signed by the red markers. For the load calculation in the middle between each control points black markers are introduced. At these

markers, the nose sections outer contour is divided, in order to obtain six differently colored sub parts assigned to the six control points. The pressure distribution on each of this sub parts is integrated by equation (4.3) and by this means the resulting force vectors, acting on the single mechanisms output nodes, are obtained.

$$\boldsymbol{F}_i = \frac{\rho}{2} v^2 b \int_{s_{i-1}}^{s_i} C_p(s) \boldsymbol{n}(s) ds \tag{4.3}$$

In equation (4.3) s is the curve length along the airfoil contour and $\boldsymbol{n}(s)$ the normal vector to the curve. $b = 0.5\,\mathrm{m}$ is the length of the wing section related to the compliant mechanism rib. For simplicity, it is assumed that the chord length on each mechanisms wing section remains constant.

The resulting load values are listed for both airfoil configurations in table 4.4. Although shear forces are neglected, a conservative model is obtained by the sectioning approach according to figure 4.5. This is because the shear forces are very small compared to the lift and act in the oposite direction for most of the occurring x-component loads . Especially for the first control point to the upper right the applied load is overestimated. At this position the flexible shell is attached to the rest of the wing and therefore in reality loads are also transferred trough the shell.

Table 4.4: Aerodynamic loads acting on the stacked mechanisms output nodes for the standard and the morphed configuration

Control Point		$j\,[-]$	1	2	3	4	5	6	**Sum**
Load	Standard Config.	$F_{CL,x}\,[\mathrm{N}]$	-17.7	-20.7	-32.5	14.2	0.4	0	-56.2
		$F_{CL,y}\,[\mathrm{N}]$	122.2	-88.3	66.1	32.7	19.2	23.7	352.1
	Morphed Config.	$F_{CL,x}\,[\mathrm{N}]$	-26.7	-28.5	-33	0.6	-3.7	-1.8	-93.1
		$F_{CL,y}\,[\mathrm{N}]$	130.1	75.9	49.7	27.7	27.7	44.2	355.3

Observing the loads in table 4.4 it is seen, that forces for the morphed and the standard condition load cases are very similar. Only their distribution between the single mechanisms changes slightly. The magnitudes are slightly higher for the morphed condition, which is primarily the case for the x-components. In both cases the resulting force acts in negative x-direction and in positive y-direction.

Due to the very similar loads in both load cases, in the following only the load case for the

morphed configuration is considered in topology optimization. The loads for this load case are applied to the mechanisms output nodes in one single counter load case according to equation (2.32).

4.2.3 FE Mesh Discretization

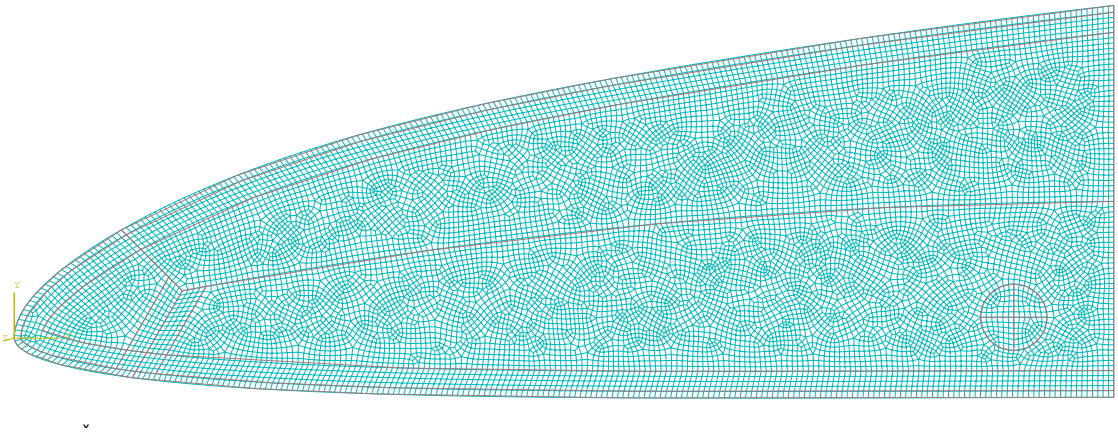

Figure 4.6: FE mesh of the wings morphing section (13017 quadrilateral elements)

In this section the used FE mesh discretization is shortly introduced. The entire morphing section of the profile is meshed by isoparametric bilinear quadrilateral finite elements (see fig. A.1). In order to obtain a homogeneous global element size distribution, an unstructured meshing approach, using various element orientations, is preferred over a structured mesh approach. Whereas for structured meshes the leading edge region is disproportionately high resolved, with unstructured meshes a similar resolution degree throughout the entire domain can be reached with fewer elements. This not only has an advantage in terms of total FE analysis cost, but also the size of the optimization problem is reduced. The drawback of the unstructured mesh approach is that higher distorted elements occur, which can be subjected to modeling errors. Figure 4.6 shows the FE mesh used for the mechanism corresponding to control point 4 in figure 4.2.

The mesh shown in figure 4.6 is with 13017 elements relatively fine. Also the segmentation of the geometry can be observed, with separate surfaces created for the distinct non design space (solid/void) areas found in figure 4.3. At the mechanisms output node a blocking separation has to be introduced, in order to create an FE node at this location, where counter loads can be applied and the nodal output displacement is defined. The mesh presented in this section and similar meshes for the mechanism ribs corresponding to other control points are used to obtain the results presented in section 4.3.

4.3 Results

In this section the results obtained for the various mechanisms of the stacked rib concept with six control points (see fig. 4.1) are presented. The results are obtained by the path-generation objective function formulation according to equation (2.31). As counter loads, the aerodynamic loads calculated in section 4.2.2 for the morphed configuration are applied. The target displacement values for the single precision points are listed for each of the six mechanisms in table 4.1. A detailed description of the modeling of the optimization problem was given in the previous section. The finite element analysis is based on the mm-t-s unit system (see table A.1).

For optimization the PDE-based density filter and the Heaviside projection approach defined in equation (2.22) are applied. The projection parameter β is updated according to equation (2.23) with $\tau = 30$, $\beta_{max} = 150$, $\beta_0 = 1$ and η selected equal to the corresponding problems volume fraction constraint value. Moreover, adaptive design variable move limits according to section A.5 are applied starting from the value $\beta_{start} = 1$. Also, the MTOP method introduced in section 2.3 is applied in order to obtain high resolution results. The filter radius is selected to $r = 1.3\,\mathrm{mm}$ and the asymptote control parameter of the MMA optimizer is set to $s = 1.07$. Furthermore, the SIMP parameter is set to $k = 3$. The energy interpolation scheme, defined in section A.4, is also used together with the parameters $\beta_1 = 500$, $\rho_0 = 0.01$ and $offset = 0.1$.

The input displacement value is initially set to $u_{in} = 5\,\mathrm{mm}$, it approximately corresponds to the total curve length difference between the standard and the morphed nose section geometry. This difference equals also to the displacement that the free end of the flexible shell to the lower right of the nose section undergoes and therefore appears to be a reasonable initial guess for the input displacement.

In the following subsection only volume constraint compliant mechanism rib results are discussed. Then in a second step the influence of the weighting factor α and the input displacement value u_{in} on these results is investigated. At the end of this section also stress constraints are considered and stress constraint compliant mechanism results are presented.

4.3.1 Only Volume Constraint Solutions

In this chapter, the path-generation topology optimization approach is applied without consideration of stress constraints. Therefore, first the mechanism for the control point number four is regarded. The optimization problem for this mechanism is illustrated schematically in figure 4.3. A volume fraction constraint of $v = 0.4$ is selected and the weighting factors α are set to

$\alpha_0 = 1$ for the case of zero counter load and to $\alpha_1 = 0.05$ for the counter load case. This choice of weighting factors α corresponds to the examples published by Pedersen et al. (2001). The displacement figure of the resulting topology together with the undeformed reference for the case of zero counter load is illustrated in figure 4.7. A stiff structure connected by thin flexible hinge regions can be observed.

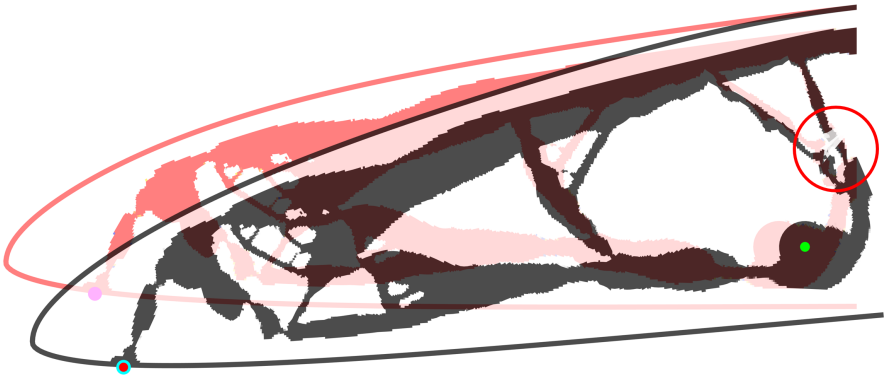

Figure 4.7: Compliant mechanism rib result for control point number four, $\Phi = 7.8\,10^{-3}\,\mathrm{mm}^2$, $u_{out,x} = 5.53\,\mathrm{mm}$, $u_{out,y} = -14.19\,\mathrm{mm}$, $F_{in} = 304.6\,\mathrm{N}$, $t = 3844.2\,\mathrm{s}$

In figure 4.7 it is also seen that the target displacement can be approximated very well, resulting also in low values for the objective function Φ. The output node represented by the red marker is almost perfectly in the middle of the blue circle, which signs the target displacement position. This is observed although the solution did not meet the convergence criteria and the maximum number of 400 iterations was reached. At the end of the optimization, small oscillations of the densities occurred, without a further change of the objective function, inhibiting the convergence. The volume constraint is active but not violated at the end of the optimization, meaning that all the available material is used. For the deformation of the mechanism, very high input forces of $F_{in} = 304.6\,\mathrm{N}$ are needed, even with the zero counter load case. The computational time t needed for this solution is a little more than one hour for 400 iterations with 13017 elements. This corresponds to a time per iteration of 9.61 seconds on the machine configuration described in section A.2. By this means, compared to the original code an acceptable time cost level for problems of this size is reached.

In figure 4.8 the relaxed von Mises stresses for the activated mechanism under the counter load case are illustrated. Looking at the stress field, it is seen that in some regions stresses well above the tensile strength of PEEK ($R_{m,PEEK} = 100\,\mathrm{N/mm}^2$) appear. The very high maximum stress value σ_{max} is caused artificially by large distortions of semi dense elements.

These elements are marked by the red circle in figure 4.7, where the distorted white elements overlay the black solid topology. By a further adjustment of the energy interpolation parameters this bad modeling of semi dense elements can be avoided. Especially the member connecting the area surrounding the input node to the supports is highly stressed. In practice the occurring stresses would cause the failure of the mechanism even before reaching the target output displacements. Similar results are also obtained for the other control points mechanisms.

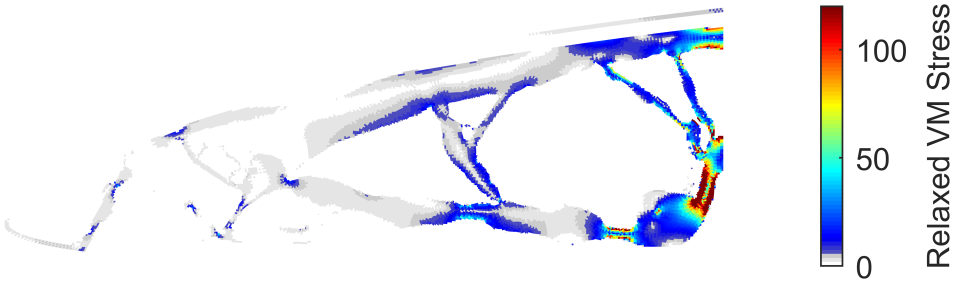

Figure 4.8: Stress distribution for the compliant mechanism rib result for control point number four $\sigma_{max} = 9688\,\mathrm{N/mm^2}$

The deformed solution topologies for all the six stacked mechanisms are listed in figure 4.9. There the target airfoil contour is also shown as reference in blue color and the control points are signed by red markers. Different volume constraint values v_{frac} are selected for the individual mechanisms. This is done because all the mechanisms are calculated in the same design space and for mechanisms related to the control points close to the support area less material is needed. Again the displacement figures are displayed for the case of zero counter load, for which all the mechanisms come close to their target displacement values.

Comparing the results in figure 4.9, it becomes evident that results (a)-(c) have higher objective function values Φ than the other results. This is caused by the higher aerodynamic loads at the suction side of the profile (see table 4.4), which lead to larger deviations from the target displacements. Furthermore, it is observed that in most of the solutions a similar bending member as previously described is introduced to the lower right. For none of the solutions the maximum stress is lower than the strength of PEEK, which means that none of the result would reach the target displacement in reality before failure. This underlines the importance of stress constraint formulations for the compliant mechanism rib application. Looking at the maximum stress values it is again seen that some of the values appear artificially high. This

is the case in fig. 4.9 (a), (d) and (f), where the stresses in semi dense elements are overestimated. But nevertheless the general stress level is still far above the strength of PEEK. In fig. 4.9 (b) this effect can not be observed, meaning that the stress are actually at this high level. The required input force level is also comparably high for most of the results, only in fig. 4.9 (f) a low value can be reached. In fig. 4.9 (a) and (f) the solutions contain still a few grey element areas. To eliminate them the energy interpolation parameters could be further adjusted.

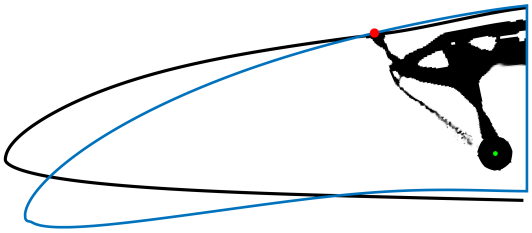

(a) Control point 1 ($v_{frac} = 0.15$): $\Phi = 3.99\,10^{-2}\,\mathrm{mm}^2$, $u_{out,x} = 0.31\,\mathrm{mm}$, $u_{out,y} = -2.05\,\mathrm{mm}$, $F_{in} = 292.6\,\mathrm{N}$, $\sigma_{max} = 7057\,\mathrm{N/mm}^2$

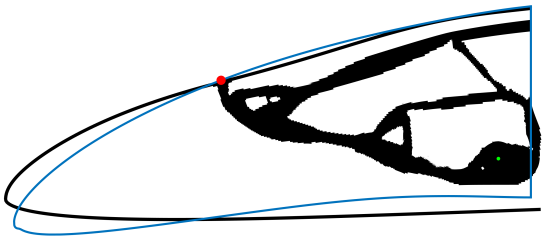

(b) Control point 2 ($v_{frac} = 0.25$): $\Phi = 1.49\,10^{-2}\,\mathrm{mm}^2$, $u_{out,x} = 1.66\,\mathrm{mm}$, $u_{out,y} = -7.34\,\mathrm{mm}$, $F_{in} = 463.5\,\mathrm{N}$, $\sigma_{max} = 1496\,\mathrm{N/mm}^2$

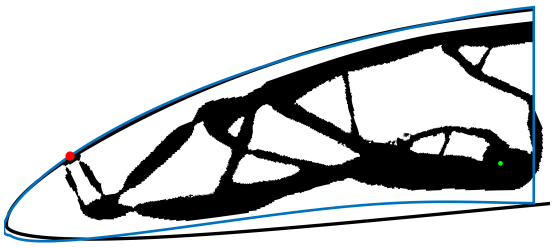

(c) Control point 3 ($v_{frac} = 0.4$): $\Phi = 2.43\,10^{-2}\,\mathrm{mm}^2$, $u_{out,x} = 4.36\,\mathrm{mm}$, $u_{out,y} = -13.84\,\mathrm{mm}$, $F_{in} = 344.6\,\mathrm{N}$, $\sigma_{max} = 686\,\mathrm{N/mm}^2$

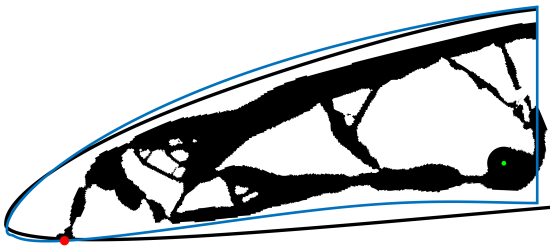

(d) Control point 4 ($v_{frac} = 0.4$): $\Phi = 7.9\,10^{-3}\,\mathrm{mm}^2$, $u_{out,x} = 5.53\,\mathrm{mm}$, $u_{out,y} = -14.19\,\mathrm{mm}$, $F_{in} = 306.9\,\mathrm{N}$, $\sigma_{max} = 9688\,\mathrm{N/mm}^2$

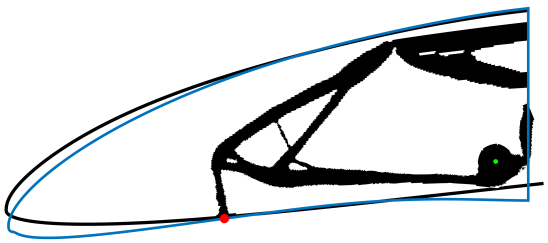

(e) Control point 5 ($v_{frac} = 0.25$): $\Phi = 3.00\,10^{-3}\,\mathrm{mm}^2$, $u_{out,x} = 5.28\,\mathrm{mm}$, $u_{out,y} = -5.69\,\mathrm{mm}$, $F_{in} = 164.2\,\mathrm{N}$, $\sigma_{max} = 719\,\mathrm{N/mm}^2$

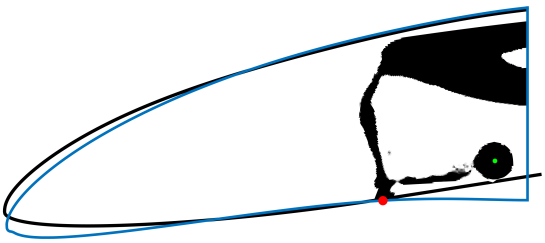

(f) Control point 6 ($v_{frac} = 0.2$): $\Phi = 5.1\,10^{-3}\,\mathrm{mm}^2$, $u_{out,x} = 4.95\,\mathrm{mm}$, $u_{out,y} = 0.01\,\mathrm{mm}$, $F_{in} = 6.2\,\mathrm{N}$, $\sigma_{max} = 1215\,\mathrm{N/mm}^2$

Figure 4.9: Solutions for the six stacked compliant mechanism ribs ($u_{in} = 5\,\mathrm{mm}$, $\alpha_0 = 1$, $\alpha_1 = 0.05$)

Observing the free belt structures in figure 4.9, it is seen that very different deformations of

the belt occur in the various results. Whereas in some solutions the belt almost deforms to the target profile shape, in others large deviations occur. The main reason for this is that the mechanisms not only apply the linear target deformations, but also transfer torque to the belt, which causes unnatural curvatures. The different belt deformations would lead to higher interaction forces between the individual solutions in the assembled rib. Furthermore, waviness of the ribs surface in the morphed state is expected as a consequence of the incompatible deformations.

There are two ways to avoid this behavior. The first one is to add the deviations of the solid element rotations close to the output node to the objective function. By this means, the deviation from the target rotation values can be minimized. Moreover, the target rotation value can easily be obtained by comparison of the normal vectors of both profile contours at the control point position. The second approach is to use conventional moment free hinges as connection between the compliant mechanisms and the belt structure. By doing so, no torque can be transferred to the belt, which in consequence leads to a natural smooth deformation of the shell. This deformation should be close to the target shape. For both approaches the optimization problem formulation, as well as the modeling have to be modified.

The results presented in this section generally show that the path-generation formulation can be used to generate also compliant mechanisms for the morphing leading edge application. In theory all the results obtained reach the target displacement values very well, but the stresses reached are far beyond the strength of PEEK. Also the input forces needed are far to high, for a reasonable application. Furthermore, it is seen that rotations imposed to the belt structure lead to compatibility problems in the stacked single output mechanism concept. Although each single mechanism reaches its target deformation, waviness is expected to occur due to wrong rotations imposed to the belt at the control points positions. Two solution concepts for this problem were proposed.

In the following sections the influence of the input displacement parameter u_{in} and the objective function weighting factor α on the volume constraint results is discussed. Then in section 4.3.4 stress constraints are added to the optimization problem formulation, in order to reduce the stresses to an acceptable level.

4.3.2 Influence of the Input Displacement Value

To examine the influence of the input displacement magnitude to the solution topologies of the optimization problem at hand, in this section results for different input displacement values u_{in}

are compared. Therefore, again solution topologies for the compliant mechanism rib number four according to figure 4.3 are generated under consideration of only volume constraints. The various result displacement figures and reference configurations obtained for the case of no counter load are illustrated in figure 4.10, where the input displacement is varied from $u_{in} = 3\,\mathrm{mm}$ in fig. 4.10 (a) to $u_{in} = 6\,\mathrm{mm}$ in fig. 4.10 (d). The resulting force and displacement values listed in figure 4.10 have the indices zero or one related to the zero counter load case and the counter load case respectively.

Observing the objective function values Φ in figure 4.10 it is seen that the solutions fig. 4.10 (a), (b) and (c) perform comparably well, with $u_{in} = 5\,\mathrm{mm}$ leading to the best objective function value. The result in fig. 4.10 (d) performs one order of magnitude worse than the other results. In terms of input force F_{in} solutions fig. 4.10 (a) and (b) are better than fig. 4.10 (c) and (d). Overall the solutions fig. 4.10 (a) and (b) represent the best combination between low input forces and good objective function values.

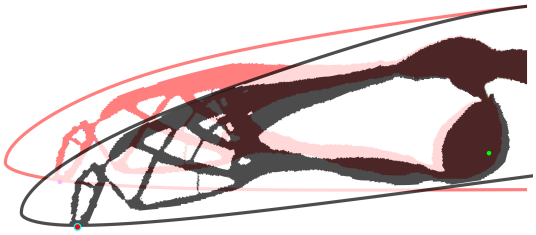

(a) $u_{in} = 3\,\mathrm{mm}$: $\Phi = 9.1\,10^{-3}\,\mathrm{mm}^2$, $u_{out,x,0} = 5.53\,\mathrm{mm}$, $u_{out,y,0} = -14.19\,\mathrm{mm}$, $F_{in,0} = 126.6\,\mathrm{N}$, $F_{in,1} = 249.4\,\mathrm{N}$, $\sigma_{max} = 196.3\,\mathrm{N/mm^2}$

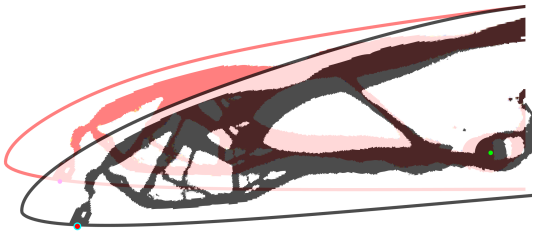

(b) $u_{in} = 4\,\mathrm{mm}$: $\Phi = 9.0\,10^{-3}\,\mathrm{mm}^2$, $u_{out,x,0} = 5.54\,\mathrm{mm}$, $u_{out,y,0} = -14.19\,\mathrm{mm}$, $F_{in,0} = 101.3\,\mathrm{N}$, $F_{in,1} = 195.8\,\mathrm{N}$, $\sigma_{max} = 716.1\,\mathrm{N/mm^2}$

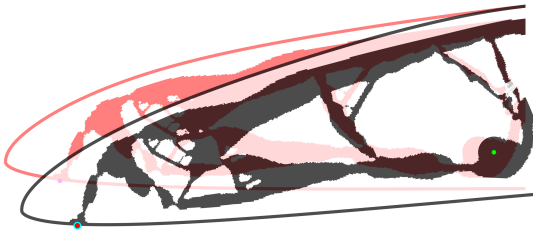

(c) $u_{in} = 5\,\mathrm{mm}$: $\Phi = 7.8\,10^{-3}\,\mathrm{mm}^2$, $u_{out,x,0} = 5.53\,\mathrm{mm}$, $u_{out,y,0} = -14.19\,\mathrm{mm}$, $F_{in,0} = 304.56\,\mathrm{N}$, $F_{in,1} = 386.8\,\mathrm{N}$, $\sigma_{max} = 9688.0\,\mathrm{N/mm^2}$

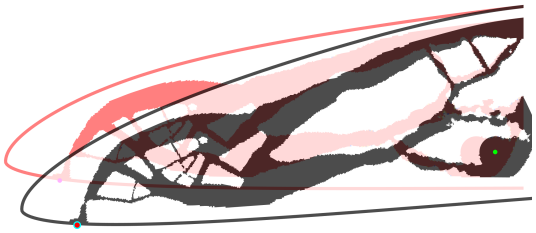

(d) $u_{in} = 6\,\mathrm{mm}$: $\Phi = 2.2\,10^{-2}\,\mathrm{mm}^2$, $u_{out,x,0} = 5.53\,\mathrm{mm}$, $u_{out,y,0} = -13.82\,\mathrm{mm}$, $F_{in,0} = 209.1\,\mathrm{N}$, $F_{in,1} = 283.5\,\mathrm{N}$, $\sigma_{max} = 724.2\,\mathrm{N/mm^2}$

Figure 4.10: Solutions of rib number four for different input displacement values u_{in} ($u^*_{out,x} = 5.53\,\mathrm{mm}$, $u^*_{out,y} = -14.18\,\mathrm{mm}$, $v_{frac} = 0.4$, $\alpha_0 = 1$, $\alpha_1 = 0.05$)

The values for the maximum relaxed von Mises stresses σ_{max} evaluated for the counter load case are also listed in figure 4.10, where in (c) as previously mentioned in section 4.3.1 artificially high stresses occur due to high distortions in semi-dense elements. For the lowest input

displacement in fig. 4.10 (a) also the lowest stresses appear.

In contrast to conventional rigid mechanisms, it is observed that increasing input displacements do not necessarily lead to decreasing input forces. This is because for compliant mechanisms the input work corresponds to the sum of output work and elastic work stored in the mechanism. Depending on the topology and the input displacement value this amount of elastic work is changing. Comparing the input forces $F_{in,0}$ for the zero counter load case and $F_{in,1}$ for the counter load case for the various solutions in figure 4.10, it is seen that the dominant share of the input force is needed for the elastic deformation of the mechanism. This is especially the case for high input displacement values, which result in mechanisms that store high amounts of elastic energy. It is also observed, that for higher input displacements the input load share transformed in output work diminishes, which corresponds to the classical rigid mechanism transmission behavior.

Figure 4.10 shows that the solutions are very sensitive to the prescribed input displacement value u_{in}, but no direct relation between this value and the quality of the solutions can be observed. It is only seen that $u_{in} = 4\,\mathrm{mm}$ appears to be a good choice for the problem formulation at hand, combining a low objective function value with low required input forces.

4.3.3 Influence of the Counter Load Weighting Factor

Apart from the input displacement magnitude u_{in}, other important influencing parameters for the path-generation problem formulation (see eq. (2.32)) are the weighting factors α. In this section a parameter study with respect to these parameters is carried out. Therefore, for the compliant mechanism rib problem the counter load case weighting factor α_1 is varied. Figure 4.11 illustrates different results obtained for the rib number four. The displacement figures and the result parameters with index one correspond to the counter load case, whereas the indicated result values with index zero are related to the zero counter load case.

As in the previous section for the input displacements the resulting topologies act also very sensitive to the counter load weighting parameter α_1. In figure 4.11, it is seen that according to the objective function definition (2.31) the values Φ increases with increasing α_1 value. The input forces are very similar for all the results except for the solution in fig. 4.11 (c), where a notably higher input force is needed. Looking at the maximum relaxed von Mises stress values $\sigma_{max,1}$, no relation between the maximum occurring stress and the weighting factor α_1 can be observed.

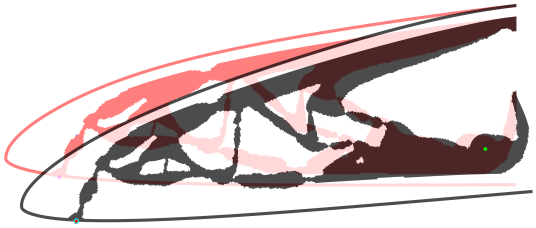

(a) $\alpha_0 = 1$, $\alpha_1 = 1$: $\Phi = 6.58\,10^{-2}\,\mathrm{mm}^2$, $u_{out,x,0} = 5.47\,\mathrm{mm}$, $u_{out,x,1} = 5.60\,\mathrm{mm}$, $u_{out,y,0} = -14.34\,\mathrm{mm}$, $u_{out,y,1} = -14.01\,\mathrm{mm}$, $F_{in,1} = 360.3\,\mathrm{N}$, $\sigma_{max,1} = 654.2\,\mathrm{N/mm}^2$

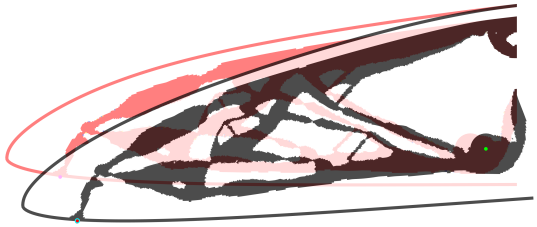

(b) $\alpha_0 = 1$, $\alpha_1 = 0.5$: $\Phi = 4.47\,10^{-2}\,\mathrm{mm}^2$, $u_{out,x,0} = 5.49\,\mathrm{mm}$, $u_{out,x,1} = 5.63\,\mathrm{mm}$, $u_{out,y,0} = -14.29\,\mathrm{mm}$, $u_{out,y,1} = -13.95\,\mathrm{mm}$, $F_{in,1} = 348.3\,\mathrm{N}$, $\sigma_{max,1} = 850.7\,\mathrm{N/mm}^2$

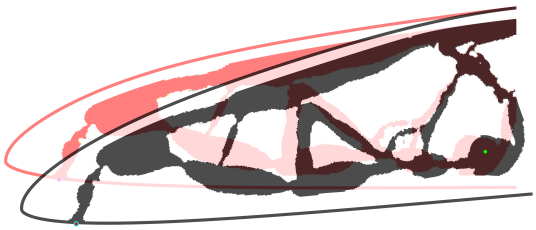

(c) $\alpha_0 = 1$, $\alpha_1 = 0.2$: $\Phi = 2.73\,10^{-2}\,\mathrm{mm}^2$, $u_{out,x,0} = 5.52\,\mathrm{mm}$, $u_{out,x,1} = 5.67\,\mathrm{mm}$, $u_{out,y,0} = -14.24\,\mathrm{mm}$, $u_{out,y,1} = -13.86\,\mathrm{mm}$, $F_{in,1} = 462.9\,\mathrm{N}$, $\sigma_{max,1} = 569.8\,\mathrm{N/mm}^2$

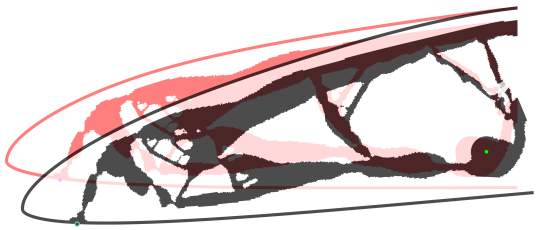

(d) $\alpha_0 = 1$, $\alpha_1 = 0.05$: $\Phi = 7.8\,10^{-3}\,\mathrm{mm}^2$, $u_{out,x,0} = 5.53\,\mathrm{mm}$, $u_{out,x,1} = 5.67\,\mathrm{mm}$, $u_{out,y,0} = -14.19\,\mathrm{mm}$, $u_{out,y,1} = -13.82\,\mathrm{mm}$, $F_{in,1} = 386.8\,\mathrm{N}$, $\sigma_{max,1} = 9688\,\mathrm{N/mm}^2$

Figure 4.11: Solutions of rib number four for different counter load weighting factors α_1 ($u^*_{out,x} = 5.53\,\mathrm{mm}$, $u^*_{out,y} = -14.18\,\mathrm{mm}$, $u_{in} = 5\,\mathrm{mm}$, $v_{frac} = 0.4$)

The result in fig. 4.11 (d) with the lowest α_1 value is very accurate for the zero counter load case. In contrast to fig. 4.11 (d) the solution in fig. 4.11 (a) has equal weighting factors for both load cases and therefore tries to find the best design compromise satisfying both requirements equally well. Comparing the absolute displacement values in fig. 4.11 (d) the largest deviations to the target displacements are $\Delta u_{out,x,1} = +0.14\,\mathrm{mm}$ and $\Delta u_{out,y,1} = +0.36\,\mathrm{mm}$. For the solution in fig. 4.11 (a) these values are $\Delta u_{out,x,1} = +0.07\,\mathrm{mm}$ and $\Delta u_{out,y,1} = +0.16\,\mathrm{mm}$, meaning that the target for zero counter load is still better approximated. The other results in fig. 4.11 (b) and fig. 4.11 (c) are somewhere in between this values.

Based on the results discussed in this section higher weighting parameters α_1 appear reasonable for further calculations of the compliant mechanism rib problem. This is because in reality the zero counter load case only occurring at the ground is of low importance for the mechanisms. In flight, where an accurate profile geometry is required aerodynamic loads act. These loads are considered by the counter load case, which in consequence must be weighted higher.

4.3.4 Stress Constraint Solutions

In this section, the stress constraint path-generation problem formulation according to equation (3.1) is applied to the compliant mechanism rib problem. One single stress constraint for the counter load case is considered. By application of this formulation to the problems in figure 4.9 with an input displacement of $u_{in} = 5\text{mm}$ only one feasible result could be obtained. For most of the solution topologies the stresses were still to high and the topologies degenerated. Solutions for the same problem setup with a reduced input displacement of $u_{in} = 4\text{mm}$ showed more promising results in combination with stress constraints. Therefore, in the following the results for the reduced input displacement value are discussed.

First for the rib number four the only volume constraint result is compared to the stress constrained result. For this reason, displacement figures and stress distributions for both cases are illustrated in figure 4.12. The displacement figures and values as well as the input force value are shown for the case of no counter load. The stress field refers to the actuated rib state with counter loads applied. In all the figures the input and output nodes are signed by green and red markers respectively.

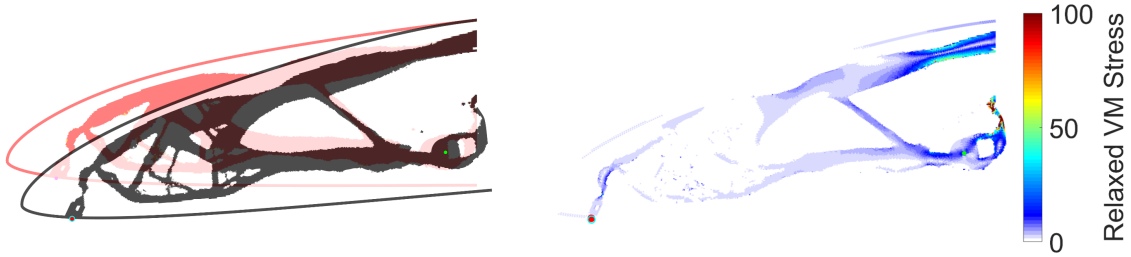

(a) Only volume constraint: $\sigma_{max} = 716.1\,\text{N/mm}^2$, $\Phi = 9\,10^{-3}\,\text{mm}^2$, $u_{out,x} = 5.54\,\text{mm}$, $u_{out,y} = -14.19\,\text{mm}$, $F_{in} = 101.3.2\,\text{N}$

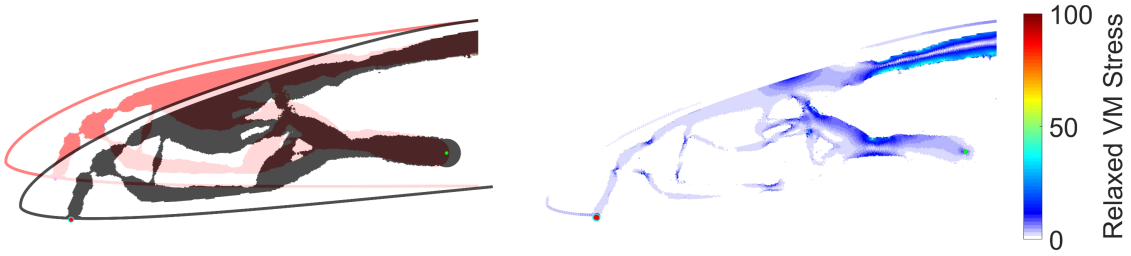

(b) Stress constraint $\sigma^* = 50\,\text{N/mm}^2$: $\overline{\sigma}_{PN,max} = 29.8\,\text{N/mm}^2$, $\Phi = 7.3\,10^{-3}\,\text{mm}^2$, $u_{out,x} = 5.53\,\text{mm}$, $u_{out,y} = -14.19\,\text{mm}$, $F_{in} = 39.9\,\text{N}$

Figure 4.12: Comparison of only volume constrained and stress constrained solutions for rib number four ($u_{in} = 4\,\text{mm}$, $v_{frac} = 0.4$, $\alpha_0 = 1$, $\alpha_1 = 0.05$)

In figure 4.12 (b), it is seen that for this example the stress constraints successfully reduce the

maximum stress level. Both the only volume constraint solution in fig. 4.12 (a) as well as the stress constraint solution in fig. 4.12 (b) come very close to the target displacement values. In fig. 4.12 (b) the maximum stress is even below the constraint value of $\sigma^* = 50\,\mathrm{N/mm^2}$, whereas in fig. 4.12 (a) the stresses are far above the material strength $R_{m,PEEK}$. Moreover, in fig. 4.12 (b) longer hinge regions appear. The main difference between the results is that in fig. 4.12 (b) there is no connecting member to the lower right. Hence, by the stress constraint formulation the area of highest stresses in fig. 4.12 (a) is simply omitted from the topology in fig. 4.12 (b). Surprisingly for this example even a better optimum is found applying the stress constraint formulation. Also the input force needed can notably be reduced by the stress constraint.

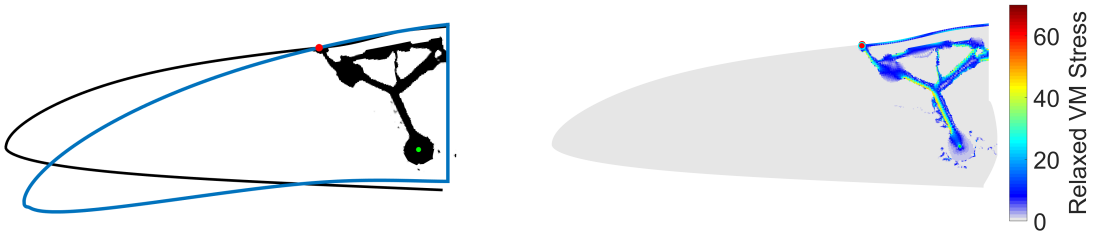

(a) Control point 1 ($v_{frac} = 0.15$, $\sigma^* = 50\,\mathrm{N/mm^2}$): $\overline{\tilde{\sigma}}_{PN,max} = 51.9\,\mathrm{N/mm^2}$, $\Phi = 2.49\,10^{-2}\,\mathrm{mm^2}$, $u_{out,x} = 0.31\,\mathrm{mm}$, $u_{out,y} = -2.11\,\mathrm{mm}$, $F_{in} = 23.2\,\mathrm{N}$

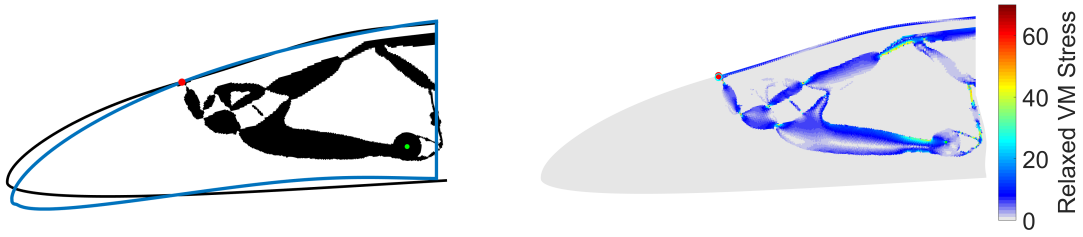

(b) Control point 2 ($v_{frac} = 0.25$, $\sigma^* = 50\,\mathrm{N/mm^2}$): $\overline{\tilde{\sigma}}_{PN,max} = 49.7\,\mathrm{N/mm^2}$, $\Phi = 1.82\,10^{-2}\,\mathrm{mm^2}$, $u_{out,x} = 1.66\,\mathrm{mm}$, $u_{out,y} = -7.34\,\mathrm{mm}$, $F_{in} = 19.5\,\mathrm{N}$

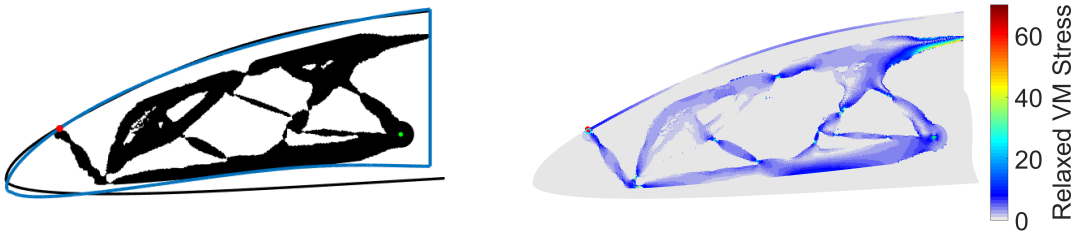

(c) Control point 3 ($v_{frac} = 0.4$, $\sigma^* = 50\,\mathrm{N/mm^2}$): $\overline{\tilde{\sigma}}_{PN,max} = 50.0\,\mathrm{N/mm^2}$, $\Phi = 3.79\,10^{-2}\,\mathrm{mm^2}$, $u_{out,x} = 4.35\,\mathrm{mm}$, $u_{out,y} = -13.84\,\mathrm{mm}$, $F_{in} = 9.1\,\mathrm{N}$

Figure 4.13: Stress constrained solutions for the stacked compliant mechanism ribs 1-3 ($u_{in} = 4\,\mathrm{mm}$, $\alpha_0 = 1$, $\alpha_1 = 0.05$)

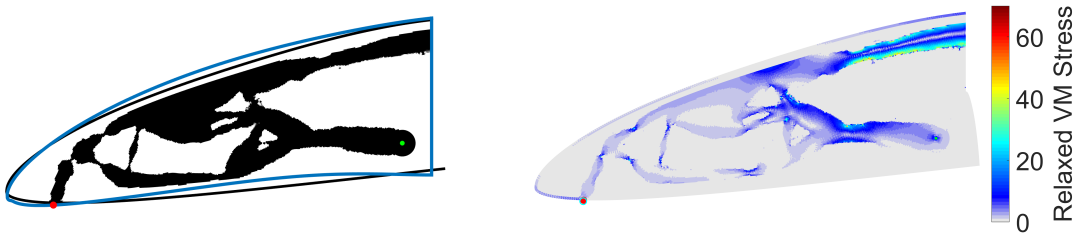

(a) Control point 4 ($v_{frac} = 0.4$, $\sigma^* = 50\,\mathrm{N/mm^2}$): $\overline{\tilde{\sigma}}_{PN,max} = 29.8\,\mathrm{N/mm^2}$, $\Phi = 7.3\,10^{-3}\,\mathrm{mm^2}$, $u_{out,x} = 5.53\,\mathrm{mm}$, $u_{out,y} = -14.19\,\mathrm{mm}$, $F_{in} = 39.9\,\mathrm{N}$

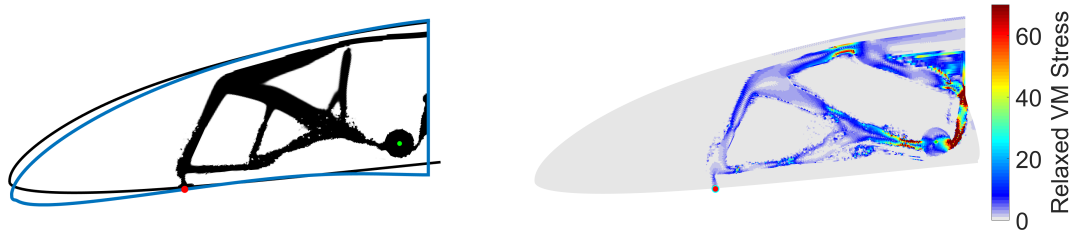

(b) Control point 5 ($v_{frac} = 0.25$, $\sigma^* = 50\,\mathrm{N/mm^2}$): $\overline{\tilde{\sigma}}_{PN,max} = 64.4\,\mathrm{N/mm^2}$, $\Phi = 4.70\,10^{-3}\,\mathrm{mm^2}$, $u_{out,x} = 5.28\,\mathrm{mm}$, $u_{out,y} = -5.69\,\mathrm{mm}$, $F_{in} = 60.6\,\mathrm{N}$

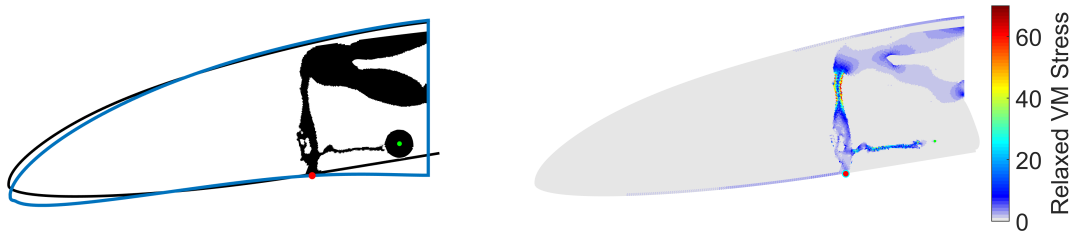

(c) Control point 6 ($v_{frac} = 0.2$, $\sigma^* = 50\,\mathrm{N/mm^2}$): $\overline{\tilde{\sigma}}_{PN,max} = 49.9\,\mathrm{N/mm^2}$, $\Phi = 8\,10^{-4}\,\mathrm{mm^2}$, $u_{out,x} = 4.96\,\mathrm{mm}$, $u_{out,y} = 0.03\,\mathrm{mm}$, $F_{in} = 16.1\,\mathrm{N}$

Figure 4.14: Stress constrained solutions for the stacked compliant mechanism ribs 4-6 ($u_{in} = 4\,\mathrm{mm}$, $\alpha_0 = 1$, $\alpha_1 = 0.05$)

The same stress constraint formulation is now applied to the other five mechanisms of the stacked rib. The resulting topologies and relaxed von Mises stress fields for all the different mechanisms are displayed for the counter loaded case in figures 4.13 and 4.14. For fig. 4.13 (b) and (c) and fig. 4.14 (a) and (c) feasible solutions could be obtained. In fig. 4.13 (a) the stress constraint is only slightly violated, whereas in fig. 4.14 (b) higher stress peaks occur.

Observing the results in both figures, it is seen that in all the topologies except for fig. 4.14 (b) the highly stressed connecting member between the input section and the fixed supports is omitted. The hinge areas are smeared out to larger areas in order to achieve distributed compliance and hence reduce local stress peaks. Looking closer to the stress distributions in fig. 4.14 (b) and (c) it is seen that stresses higher then the p-norm stress occur, meaning that the p-norm approximation for this examples gives to low stress values. For the solution in

fig. 4.13 (a) the opposite effect is observed. There the p-norm gives to high stress values. In consequence in reality the solution in fig. 4.13 (a) is a feasible design, whereas the result in fig. 4.14 (c) is infeasible. The p-norm formulation introduced in section 2.4 should therefore be reviewed and eventually modified in future work in order to achieve better approximations of the maximum stress.

The indicated displacement and force values in fig. 4.13 and fig. 4.14 are again referred to the case of zero counter load. The input forces are still high but could be reduced approximately by the factor of 10 compared to the results in figure 4.9. Furthermore, the objective function values Φ are comparable to the only volume constraint results in figure 4.9, meaning that the stress constrained solutions perform similarly good.

The results presented in this section show that by the introduction of stress constraints the compliant mechanisms could be significantly improved. Whereas the prior results in figure 4.9 in reality could not even reach the target displacement without failure, all of the results in figures 4.13 and 4.13 except for fig. 4.14 (b) are able to do so. Moreover, for several topologies the stress level could be even reduced below $\sigma^* = 50\,\mathrm{N/mm^2}$, which results in a first form of fatigue-resistant design. The mechanisms still reach good objective function values and the required input force was also reduced. The fact that for an input displacement of $u_{in} = 5\,\mathrm{mm}$ only one feasible stress constraint solution could be obtained underlines the importance of the prescribed input displacement magnitude.

5 Conclusion and Outlook

In this thesis, the compliant mechanism topology optimization code *mechtop* (Reinisch 2017), developed in previous work, was extended by multiple functionalities. The new implementations were first tested on generic example problems. Then they were applied, in order to optimize first compliant mechanism ribs for a wing concept with morphing forward section under consideration of geometric nonlinear FEM.

5.1 Code Extension

At the beginning of this work, the FE solver and the entire optimization loop were adapted in order to consider also non-regular FE meshes. An interface to the commercial *Abaqus* preprocessor was provided, allowing the import of complex geometry meshes. Moreover, a displacement-controlled FE solver was introduced. In the following the path-generation objective function formulation according to Pedersen et al. (2001) was implemented, allowing the generation of exact output displacement or output path following mechanisms. The stress constraint formulation for nonlinear compliant mechanism synthesis introduced in prior work (Reinisch 2017) was then combined with this path-generation formulation. In addition other methods, as the PDE-based filtering techniques (Lazarov & Sigmund 2011) and the multiresolution topology optimization scheme (MTOP) (Nguyen et al. 2010), were implemented. Various other changes, as for example the parallelization of the inner FE loops, were introduced in order to accelerate the code. Furthermore, the code was restructured to an input file format, based on an *Excel*-sheet containing the entire parameter set defining the optimization problem.

Two example problems were introduced to test the implementations. The different nonlinear FE solver formulations were tested on a planar cantilever example and validated by comparison to the solution obtained in *Abaqus*. In the following the newly implemented topology optimization methods were applied to a generic path-generation example problem. The obtained results proved the validity of the implementations. A powerful tool for topology optimization of 2D compliant mechanisms is the result of this work.

5.2 Compliant Mechanism Rib Optimization

The expanded code was applied in order to generate compliant mechanism ribs for the morphing wing application. A new concept of stacked single input and single output ribs has therefore been introduced and the optimization problem modeling for this concept was outlined. By application of the path-generation formulation in combination with a PDE-based density filter

and the MTOP approach first high resolution results based on geometric nonlinear FEM could be obtained for the compliant mechanism ribs.

Most of the resulting topologies closely approximate the prescribed target output displacement values. However, in the results obtained under consideration of only volume constraints very high stresses appear, exceeding the strength of PEEK. Therefore, in reality these mechanisms would break even before reaching the target output displacements. Furthermore, for most of the solutions very high input forces are needed in order to deform the mechanisms. By the addition of stress constraints to the problem formulation the results could be improved. The maximum stress level as well as the required input forces could be significantly reduced for most of the mechanisms.

Despite of the improvements the results obtained are still some steps away form a real world application. Especially for the counter load case, the actuation forces are still high and observing the solution topologies also other drawbacks are noticed. One of these is that most of the mechanisms also apply torque to the outer belt structure. The resulting twist of the belt structure is not taken in to account in the optimization problem formulation and can lead to wrong curvatures along the profile contour in the assembled rib. Two possible solution approaches for this problem were discussed in section 4.3.1.

5.3 Recommendations for Further Work

The results obtained in this work represent a drastic improvement in the development of the compliant mechanism ribs in the project MILAN. Topology optimization methods based on nonlinear analysis could be used for the first time to synthesize compliant mechanism ribs. Nevertheless many further improvements have to be made towards a real world application of the mechanisms. The extended *mechtop* code builds a good basis for the necessary further development. Some simplifications made, as the modeling of the flexible shell by the mechanisms material and the neglection of the interaction between the single mechanisms for the stacked concept need to be considered more in detail. In general a consideration of both the integral and the stacked mechanism concept is recommended for the future development. In the following multiple ideas for future work are shortly outlined:

***Python* Script for Mesh Generation** Especially for the stacked mechanism concept, where multiple different mechanisms for one rib have to be generated, mesh generation represents a large share of work. By the creation of a *Python* script for mesh generation in *Abaqus* the process could be automatized.

Multiple Output Problem Formulation In order to use the path generation objective function formulation also for the synthesis of integral compliant mechanism ribs, the problem formulation can be extended for multiple output nodes. This can be done either by a min-max approach or by an extension of the path-generation objective function, which can be written as follows:

$$\Phi = \sum_{j=1}^{J} \sum_{i=0}^{2} \alpha_i \sum_{m=1}^{M} [\boldsymbol{u}_{out,m,i,j} - \boldsymbol{u}^*_{out,m,j}]^2 \tag{5.1}$$

where the index j describes the control point number and J the total number of control points along the profile contour. For this formulation global counter load cases valid for all the control points have to be applied. These could be for example some of the distributed aerodynamic load cases acting along the profiles contour. Moreover, the number of FE analyses needed per iteration does not change using this approach, only additional adjoint load cases for sensitivity analysis have to be solved.

Target Element Rotations Wrong curvatures are applied to the outer belt structure in solutions of the stacked compliant mechanism rib concept. In order to avoid this, also a squared error approach regarding the elements rigid body rotations close to the output node could be added to the path-generation objective function.

Nonlinear Material Law In future work a nonlinear material law should be added to the FE solver. This allows an accurate modeling of the highly nonlinear material behavior of PEEK.

Compliance Constraint In order to further reduce the input loads a constraint to the compliance could be added. The compliance in the linear case corresponds to the double of the external work applied to the mechanism, which equals to the double of the strain energy. By this means, the compliance is also a measure for the elastic energy stored in the mechanism. As a result, because the input displacement is prescribed the input force can be constrained by constraining the compliance to a maximum value. For this reason a compliance constraint should be introduced for the zero counter load case.

Code Acceleration An integration of the parallel MMA implementation used in the *Petsc* topology optimization code of the TopOpt research group at DTU (TopOpt 2018) via mex files could lead to further speed improvements. Moreover, could the FE assembly cost be reduced by the change to a classical residuum formulation and hence the omission of the $\boldsymbol{K}(\boldsymbol{U})$ terms. Therefore, the expressions $\boldsymbol{K}(\boldsymbol{U})\boldsymbol{U}$ or $\boldsymbol{K}_e(\boldsymbol{u}_e)\boldsymbol{u}_e$ in the optimization formulations have to be replaced with the global or local internal force vectors respectively. For the FE solver a version

with this change was already added to the *mechtop* code.

Stress Constraint Update Scheme Similar to the β continuation scheme in equation (2.23) an update scheme to the stress constraint value σ^* could be introduced. The value σ^* could thereby be reduced from a large initial value to the target end value over the number of iterations. Another idea is to artificially reduce the element stresses at the beginning of the optimization and to update the stress reduction parameter such that at the end of the optimization the real stresses are obtained. By this means the stress constraint value σ^* could stay constant. The outlined approaches could improve the convergence behavior of stress constrained optimizations.

Flexible Shell Modelling For a more accurate modeling of the flexible shell structure other material properties and thickness values than the mechanisms base materials values could be assigned to the solid belt elements.

Coupled Optimization of Multiple Ribs In order to account for interaction effects between the individual mechanisms, the mechanisms optimization could be coupled. This could be done by an exchange of stiffness information in each single iteration and a contemporary optimization of all the ribs.

Parameter Variation Due to the fact that a highly sensitive behavior of the result topologies with respect to most of the optimization and modeling parameters is observed, further parameter studies should be conducted. By this means, apart from the optimization parameters modeling parameters as the input node location and the support area should also be varied. Another idea is to investigate the impact of the relation between single optimization parameters on the solutions. Therefore, in section A.6 related optimization terms and their influence over the density are exemplarily shown. Furthermore, solutions on finer FE meshes should be obtained.

Bibliography

Achleitner, J. & Baier, H. (2016), Cellskin - a new flexible shell structure for a morphing wing aircraft, *in* 'International Conference on Composite Structures (19th, Porto, 2016)', Porto.

Ananthasuresh, G., Kota, S. & Gianchandani, Y. (1994), A methodical approach to the design of compliant micromechanisms, *in* 'Solid-state sensor and actuator workshop', Vol. 1994, SC: IEEE, pp. 189–192.

Andreassen, E., Clausen, A., Schevenels, M., Lazarov, B. S. & Sigmund, O. (2011), 'Efficient topology optimization in matlab using 88 lines of code', *Structural and Multidisciplinary Optimization* **43**(1), 1–16.

Bendsøe, M. P. & Kikuchi, N. (1988), 'Generating optimal topologies in structural design using a homogenization method', *Computer Methods in Applied Mechanics and Engineering* **71**(2), 197–224.

Bendsøe, M. P. & Sigmund, O. (2004), *Topology optimization: Theory, methods, and applications*, Engineering online library, 2. ed., corr. printing edn, Springer, Berlin.

Bruns, T. E. & Tortorelli, D. A. (2001), 'Topology optimization of non-linear elastic structures and compliant mechanisms', *Computer Methods in Applied Mechanics and Engineering* **190**(26-27), 3443–3459.

Bruns, T. E. & Tortorelli, D. A. (2003), 'An element removal and reintroduction strategy for the topology optimization of structures and compliant mechanisms', *International Journal for Numerical Methods in Engineering* **57**(10), 1413–1430.

Buhl, T., Pedersen, C. B. W. & Sigmund, O. (2000), 'Stiffness design of geometrically nonlinear structures using topology optimization', *Structural and Multidisciplinary Optimization* **19**(2), 93–104.

CS-22 (2008), Sailplanes and powered sailplanes, certification standard, EASA.

De Leon, D. M., Alexandersen, J., O. Fonseca, J. S. & Sigmund, O. (2015), 'Stress-constrained

topology optimization for compliant mechanism design', *Structural and Multidisciplinary Optimization* **52**(5), 929–943.

Guest, J. K., Asadpoure, A. & Ha, S.-. (2011), 'Eliminating beta-continuation from heaviside projection and density filter algorithms', *Structural and Multidisciplinary Optimization* **44**(4), 443–453.

Guest, J. K., Prevost, J. H. & Belytschko, T. (2004), 'Achieving minimum length scale in topology optimization using nodal design variables and projection functions', *International Journal for Numerical Methods in Engineering* **61**(2), 238–254.

Harzheim, L. (2014), *Strukturoptimierung: Grundlagen und Anwendungen*, Edition Harry Deutsch, Europa Lehrmittel Verlag.

Kota, S., Lu, K. ., Kreiner, Z., Trease, B., Arenas, J. & Geiger, J. (2005), 'Design and application of compliant mechanisms for surgical tools', *Journal of Biomechanical Engineering* **127**(6), 981–989.

Lazarov, B. S. & Sigmund, O. (2011), 'Filters in topology optimization based on helmholtz-type differential equations', *International Journal for Numerical Methods in Engineering* **86**(6), 765–781.

Le, C., Norato, J., Bruns, T., Ha, C. & Tortorelli, D. (2010), 'Stress-based topology optimization for continua', *Structural and Multidisciplinary Optimization* **41**(4), 605–620.

Lumpe, T. (2015), Untersuchung von einflussnahmemöglichkeiten auf die ergebnistopologie in der strukturoptimierung unter berücksichtigung von fertigungsrestriktionen, Term thesis, TUM LLB.

Mahl, M., Klaproth, T. & Baier, H. (2016), Thermo-mechanische untersuchungen von hochleistungskunststoffen für kryogene wasserstoffdrucktanks, TUM LLB.

Michaleris, P., Tortorelli, D. A. & Vidal, C. A. (1994), 'Tangent operators and design sensitivity formulations for transient non-linear coupled problems with applications to elastoplasticity', *International Journal for Numerical Methods in Engineering* **37**(14), 2471–2499.

Nguyen, T. H., Paulino, G. H., Song, J. & Le, C. H. (2010), 'A computational paradigm for multiresolution topology optimization (mtop)', *Structural and Multidisciplinary Optimization* **41**(4), 525–539.

Papazafeiropoulos, G., Muniz-Calvente, M. & Martinez-Paneda, E. (2017), 'Abaqus2matlab: A suitable tool for finite element post-processing', *Advances in Engineering Software* **105**, 9 – 16.

Patil, A. (2015), Fem matlab code for linear and nonlinear bending analysis of plates.
URL: *https://tinyurl.com/yct9xrw2*

Pedersen, C. B. W., Buhl, T. & Sigmund, O. (2001), 'Topology synthesis of large-displacement compliant mechanisms', *International Journal for Numerical Methods in Engineering* **50**(12), 2683–2705.

Pohl, T. (2014), Adaptive Methoden zur Pfadverfolgung bei Entfestigung, PhD thesis, Universität Stuttgart.

Poulsen, T. A. (2002), 'A simple scheme to prevent checkerboard patterns and one-node connected hinges in topology optimization', *Structural and Multidisciplinary Optimization* **24**(5), 396–399.

Poulsen, T. A. (2003), 'A new scheme for imposing a minimum length scale in topology optimization', *International Journal for Numerical Methods in Engineering* **57**(6), 741–760.

Reinisch, J. (2017), Topologieoptimierung von compliant mechanisms mit nichtlinearer fem und spannungsrestriktionen, Term thesis, TUM LLB.

Salehar, L. (2015), Preliminary design of a compliant mechanism for a morphing wing leading edge, Term thesis, TUM LLB.

Salehar, L. (2017), Synthesis of compliant mechanisms using topology optimization based on nonlinear finite element method, Diploma thesis, TUM LLB.

Sigmund, O. (1994), Design of Material Structures Using Topology Optimization, PhD thesis, Technical University of Denmark.

Sigmund, O. (1997), 'On the design of compliant mechanisms using topology optimization', *Mechanics of Structures and Machines* **25**(4), 493–524.

Sigmund, O. (2001), 'A 99 line topology optimization code written in matlab', *Structural and Multidisciplinary Optimization* **21**(2), 120–127.

Sigmund, O. (2007), 'Morphology-based black and white filters for topology optimization', *Structural and Multidisciplinary Optimization* **33**(4-5), 401–424.

Svanberg, K. (1987), 'The method of moving asymptotes—a new method for structural optimization', *International Journal for Numerical Methods in Engineering* **24**(2), 359–373.

TopOpt (2018), Research group, technical university of denmark.
URL: *http://www.topopt.dtu.dk/*

Wall, W. (2017), *Nichtlineare Finite-Element-Methoden*, Lecture notes, TUM LNM.

Wang, F., Lazarov, B. S., Sigmund, O. & Jensen, J. S. (2014), 'Interpolation scheme for fictitious domain techniques and topology optimization of finite strain elastic problems', *Computer Methods in Applied Mechanics and Engineering* **276**, 453–472.

Wiessmeier, M. (2011), Konzept einer formvariablen tragfluegelvorderkante bei einem segel flugzeug mit innenliegender ansteuerung über ein rotary drive system (rds), Term thesis, LLS TUM.

Declaration of Authorship

I declare that this thesis and the work presented in it are my own and have been generated by me as the result of my own original research.

I confirm that:

1. No part of this thesis has been previously submitted for a degree or any other qualification at any other University or institution, other than the Technische Universität München;

2. Where I have consulted the published work of others, this is always clearly attributed and where I have quoted from the work of others, the source is always given. With the exception of such quotations, this thesis is entirely my own work;

....

City, Date Signature

A Appendix

A.1 Units

Finite element analysis in this work is performed based on the mm-t-s unit system. The units and their SI system conversion are listed in table A.1.

Table A.1: Unit system for FE analysis

	Quantity	Unit	SI Conversions
Base Units	Length	mm	$10^{-3}\,\mathrm{m}$
	Mass	t	$10^{3}\,\mathrm{kg}$
	Time	s	$1\,\mathrm{s}$
Derived Units	Force	N	$1\,\mathrm{kgm/s^2}$
	Density	$\mathrm{t/mm^3}$	$10^{12}\,\mathrm{kg/m^3}$
	Stress	$\mathrm{N/mm^2}$	$10^{6}\,\mathrm{kg/ms^2}$

A.2 Computer Hardware Configuration

For the optimization of all the results presented in this work a virtual machine on a *Linux* cluster with the hardware resources according to table A.2 was used. All computational times indicated are referred to this system configuration.

Table A.2: Hardware resources of the virtual machine used for analysis

Processor	8xIntel(R) Xeon(R) Gold 6134 CPU @ 3.20GHz
Memory	19.1GB 2666MHz DDR4
Operating System	Linux Mint 18.3 Sylvia 64 bit

A.3 Finite Element Theory

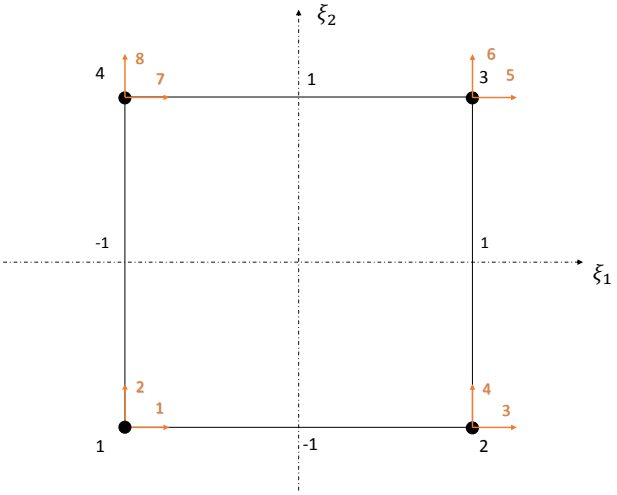

Figure A.1: Definition of the isoparametric bilinear quadrilateral finite elements used in this work (Reinisch 2017)

Isoparametric shapefunctions:

$$\boldsymbol{N}(\boldsymbol{\xi}) = \begin{bmatrix} N^1(\boldsymbol{\xi}) \\ N^2(\boldsymbol{\xi}) \\ N^3(\boldsymbol{\xi}) \\ N^4(\boldsymbol{\xi}) \end{bmatrix} = \begin{bmatrix} \frac{1}{4}(1-\xi_1)(1-\xi_2) \\ \frac{1}{4}(1+\xi_1)(1-\xi_2) \\ \frac{1}{4}(1+\xi_1)(1+\xi_2) \\ \frac{1}{4}(1-\xi_1)(1+\xi_2) \end{bmatrix} \tag{A.1}$$

Element stress vector:

$$\boldsymbol{\sigma}_e = \boldsymbol{\sigma}_{PK,e} = [\sigma_{11}, \sigma_{22}, \sigma_{12}]^{\mathbf{T}} \tag{A.2}$$

Von Mises stresses:

$$\boldsymbol{\sigma}_{vm,e} = \sqrt{\boldsymbol{\sigma}_e^{\mathbf{T}} \boldsymbol{V} \boldsymbol{\sigma}_e} \tag{A.3}$$

$\boldsymbol{V}$ operator matrix according to De Leon et al. (2015):

$$\boldsymbol{V} = \begin{bmatrix} 1 & -\frac{1}{2} & 0 \\ -\frac{1}{2} & 1 & 0 \\ 0 & 0 & 3 \end{bmatrix} \tag{A.4}$$

St. Venant-Kirchhoff constitutive matrix for plane stress:

$$\boldsymbol{C}_{VK} = \frac{E}{1-\nu^2}\begin{bmatrix} 1 & \nu & 0 \\ \nu & 1 & 0 \\ 0 & 0 & \frac{1-\nu}{2} \end{bmatrix} \tag{A.5}$$

A.3.1 Geometric Nonlinear FEM

Green-Lagrange strain vector:

$$\boldsymbol{E}_{GL} = \begin{bmatrix} E_1^1 \\ E_2^2 \\ 2E_2^1 \end{bmatrix} = \begin{bmatrix} u^1_{,1} + \frac{1}{2}((u^1_{,1})^2 + (u^2_{,1})^2) \\ u^2_{,2} + \frac{1}{2}((u^2_{,2})^2 + (u^1_{,2})^2) \\ u^1_{,2} + u^2_{,1} + u^1_{,1}u^1_{,2} + u^2_{,1}u^2_{,2} \end{bmatrix} \tag{A.6}$$

$$\boldsymbol{E}_{GL} = (\overline{\mathbf{1}}^{\mathbf{T}} + \frac{1}{2}\overline{\boldsymbol{H}}^{\mathbf{T}})\boldsymbol{B}_L\boldsymbol{u}_e \tag{A.7}$$

$\boldsymbol{B}_L$ matrix:

$$\boldsymbol{B}_L = \begin{bmatrix} N^1_{,x} & 0 & N^2_{,x} & \cdots & N^4_{,x} & 0 \\ 0 & N^1_{,y} & 0 & \cdots & 0 & N^4_{,y} \\ N^1_{,y} & 0 & N^2_{,y} & \cdots & N^4_{,y} & 0 \\ 0 & N^1_{,x} & 0 & \cdots & 0 & N^4_{,x} \end{bmatrix} \tag{A.8}$$

Alternative matrix notation for the deformation Gradient $\overline{\boldsymbol{F}}$ according to Wall (2017):

$$\overline{\boldsymbol{F}} = \underbrace{\begin{bmatrix} 1 & 0 & 0 \\ 0 & 1 & 0 \\ 0 & 0 & 1 \\ 0 & 0 & 1 \end{bmatrix}}_{\overline{\mathbf{1}}} + \underbrace{\begin{bmatrix} H_1^1 & 0 & H_2^1 \\ 0 & H_2^2 & H_1^2 \\ 0 & H_2^1 & H_1^1 \\ H_1^2 & 0 & H_2^2 \end{bmatrix}}_{\overline{\boldsymbol{H}}} \tag{A.9}$$

$$\tilde{\boldsymbol{H}} = \begin{bmatrix} H_1^1 \\ H_2^2 \\ H_2^1 \\ H_1^2 \end{bmatrix} = \boldsymbol{B}_L * \boldsymbol{u}_e \tag{A.10}$$

Definition of the nonlinear stiffness matrix $\boldsymbol{K}(\boldsymbol{U})$ according to Patil (2015):

$$\boldsymbol{K}_e(\boldsymbol{u}_e) = \int_{\Omega_e} \boldsymbol{B}_L^{\mathbf{T}} \overline{\boldsymbol{F}} \boldsymbol{C}_{VK} (\overline{\mathbf{1}}^{\mathbf{T}} + \frac{1}{2} \overline{\boldsymbol{H}}^{\mathbf{T}}) \boldsymbol{B}_L dV \tag{A.11}$$

Definition of the tangent stiffness matrix $\boldsymbol{K}_T$:

$$\boldsymbol{K}_{Te}(\boldsymbol{u}_e) = \int_{\Omega_e} \boldsymbol{B}_L^{\mathbf{T}} \overline{\boldsymbol{F}} \boldsymbol{C}_{VK} \overline{\boldsymbol{F}}^{\mathbf{T}} \boldsymbol{B}_L dV \tag{A.12}$$

Residuum:

$$\boldsymbol{R}(\boldsymbol{U}) = \boldsymbol{K}(\boldsymbol{U})\,\boldsymbol{U} - \lambda \boldsymbol{F} \tag{A.13}$$

Second Piola-Kirchhoff stresses:

$$\boldsymbol{\sigma}_{PK,e} = \boldsymbol{C}_{VK} \boldsymbol{E}_{GL} \tag{A.14}$$

Linearization of the extended residual $\boldsymbol{R}_{ext}$:

$$\boldsymbol{R}_{ext,lin} = \begin{bmatrix} \boldsymbol{R}(\boldsymbol{U}, \lambda) \\ f(\boldsymbol{U}, \lambda) \end{bmatrix}^i + \begin{bmatrix} \frac{\partial \boldsymbol{R}}{\partial \boldsymbol{U}} & \frac{\partial \boldsymbol{R}}{\partial \lambda} \\ \frac{\partial f}{\partial \boldsymbol{U}} & \frac{\partial f}{\partial \lambda} \end{bmatrix}^i \begin{bmatrix} \Delta \boldsymbol{U} \\ \Delta \lambda \end{bmatrix}^{i+1} \tag{A.15}$$

Modified load incrementation formulation for path-generation:

$$\boldsymbol{\lambda} = \begin{bmatrix} 1 & 0 & \dots & \dots & \dots & \dots & 0 \\ 0 & \ddots & 0 & \dots & \dots & \dots & 0 \\ \vdots & 0 & 1 & \dots & \dots & \dots & 0 \\ \vdots & \vdots & 0 & \lambda_c & 0 & \dots & 0 \\ \vdots & \vdots & \vdots & 0 & 1 & 0 & 0 \\ \vdots & \vdots & \vdots & \vdots & 0 & \ddots & 0 \\ 0 & 0 & 0 & 0 & 0 & 0 & 1 \end{bmatrix} \tag{A.16}$$

$$\boldsymbol{R}(\boldsymbol{U}) = \boldsymbol{K}(\boldsymbol{U})\,\boldsymbol{U} - \boldsymbol{\lambda} \boldsymbol{F} \tag{A.17}$$

A.3.2 FE Solver Flowcharts

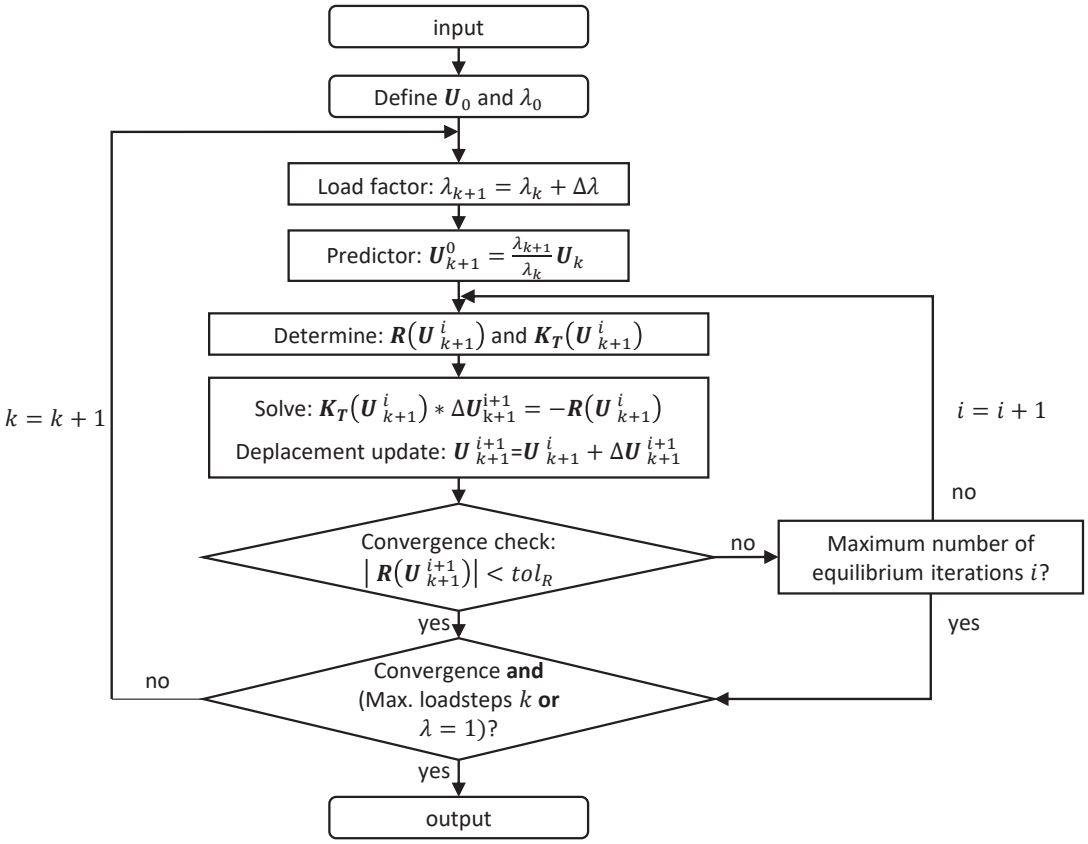

Figure A.2: Flowchart of force controlled geometric nonlinear FE solver based on (Wall 2017)

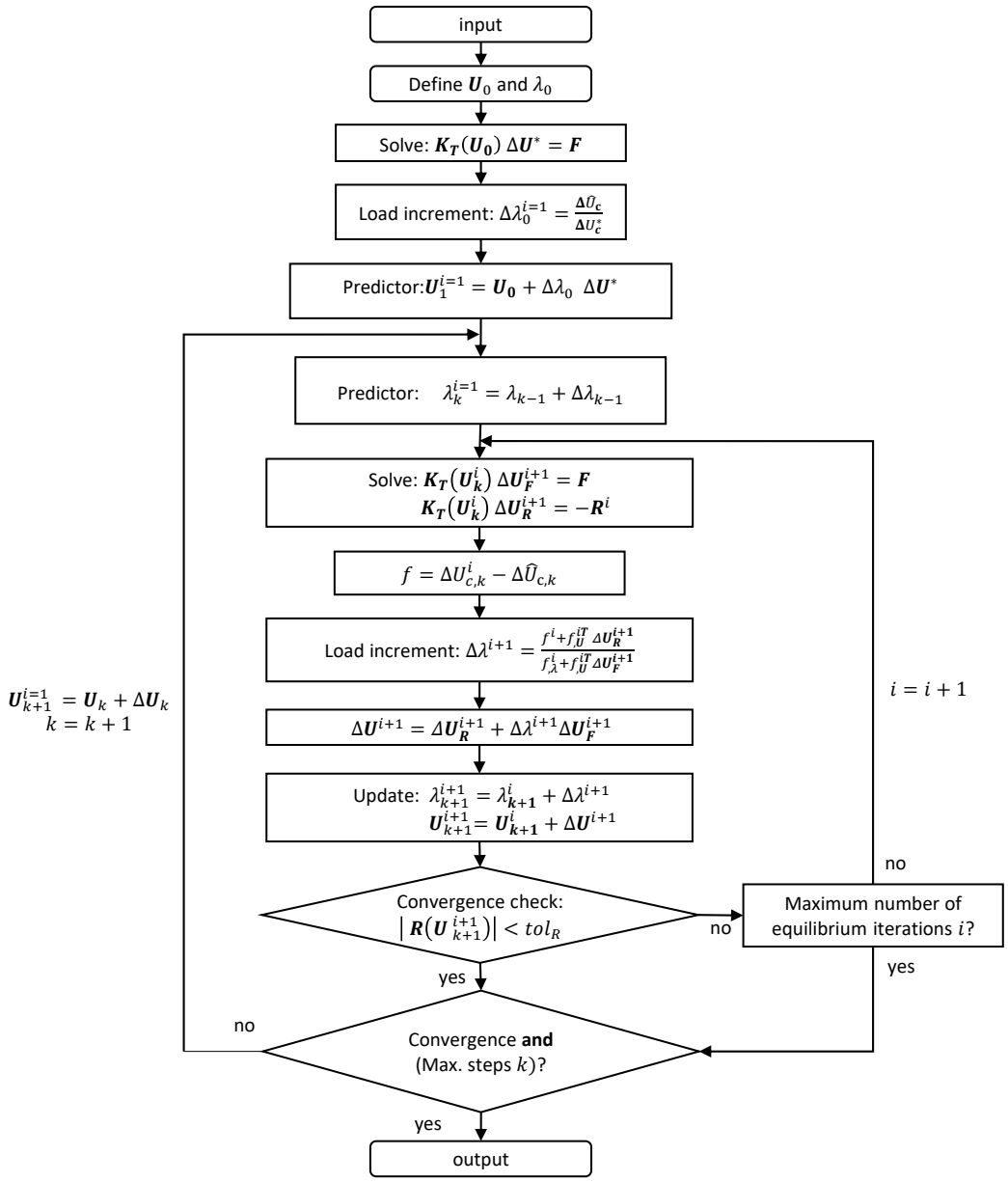

Figure A.3: Flowchart of displacement-controlled geometric nonlinear FE solver based on (Wall 2017)

A.4 Energy Interpolation Scheme

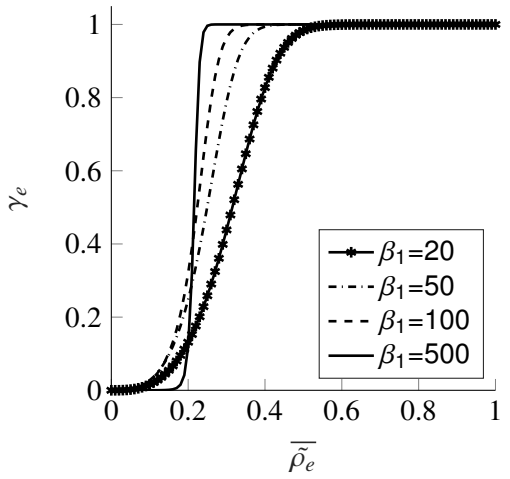

(a) Variation of β_1 ($\rho 1 = 0.01$, $offset = 0$)

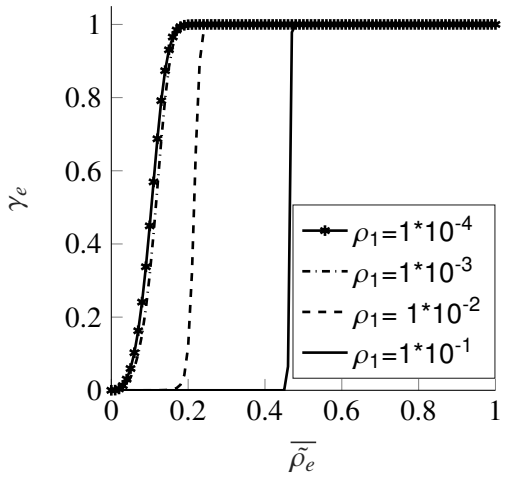

(b) Variation of $\rho 1$ ($\beta_1 = 500$, $offset = 0$)

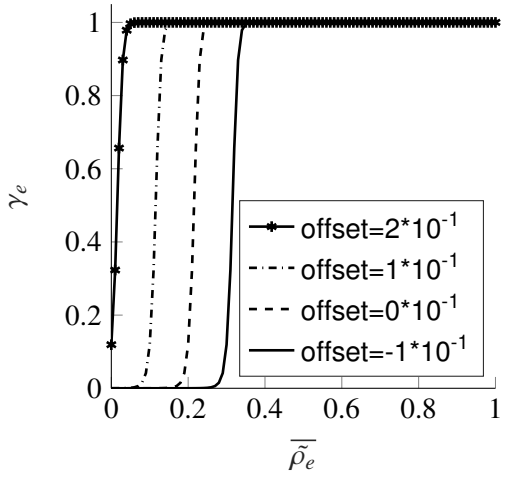

(c) Variation of $offset$ ($\beta_1 = 500$, $\rho 1 = 0.01$)

Figure A.4: Relation between the energy interpolation factor γ_e and the densities $\overline{\tilde{\rho}}_e$ (Reinisch 2017)

Element residuum for the energy interpolation scheme:

$$\boldsymbol{R}_e(\boldsymbol{u}_e) = \boldsymbol{K}_e(\gamma_e \boldsymbol{u}_e)\, \boldsymbol{u}_e - \lambda \boldsymbol{f} \tag{A.18}$$

Energy interpolation factor γ_e:

$$\gamma_e = \frac{\tanh(\beta_1 \rho_1) + \tanh(\beta_1((\overline{\tilde{\rho}_e} - offset)^k - \rho_1))}{\tanh(\beta_1 \rho_1) + \tanh(\beta_1(1 - \rho_1))} \tag{A.19}$$

$\beta 1$, $\rho 1$ and $offset$ are variable optimization parameters, which have to be defined in the opti-

mization input file.

Chain rule for sensitivity analysis for the energy interpolation scheme:

$$\frac{\partial \boldsymbol{R}}{\partial \rho_e} = \sum_{j \in \mathbb{N}_e} \Big(\frac{\partial \boldsymbol{K}(\boldsymbol{U})}{\partial \overline{\tilde{\rho}_j}} \boldsymbol{u}_j + \frac{\partial \boldsymbol{K}(\boldsymbol{U})}{\partial \gamma_j} \frac{\partial \gamma_j}{\partial \overline{\tilde{\rho}_j}} \boldsymbol{u}_e \Big) \frac{\partial \overline{\tilde{\rho}_j}}{\partial \tilde{\rho}_j} \frac{\partial \tilde{\rho}_j}{\partial \rho_e} \tag{A.20}$$

A.5 External Design Variable Move Limits

If projection methods are used projection-dependent external design variable move limits $\boldsymbol{\rho}_{min}$ and $\boldsymbol{\rho}_{max}$ are applied for each iteration i. They are defined as follows (Reinisch 2017):

$$\boldsymbol{\rho}_{min}(\rho) \leq \boldsymbol{\rho}_{i+1} \leq \boldsymbol{\rho}_{max}(\rho) \tag{A.21}$$

with $\boldsymbol{\rho}_{min}$ and $\boldsymbol{\rho}_{max}$ resulting for the projection method according to equation (2.1.5.2) in each iteration as:

$$\boldsymbol{\rho}_{min/max} = \begin{cases} \boldsymbol{\rho}_i \pm \frac{1}{2\beta} \ln(1 - 0.999) & \beta > \beta_{start} \\ 0/1 & \beta \leq \beta_{start} \end{cases} \tag{A.22}$$

a nd for the method defined in equation (2.22) as:

$$\boldsymbol{\rho}_{min/max} = \begin{cases} \boldsymbol{\rho}_i \pm \frac{1}{4\beta} \operatorname{atanh}\Big[0.999\Big(\tanh(\beta\eta) + \tanh(\beta(1-\eta))\Big) - \tanh(\beta\eta)\Big] & \beta > \beta_{start} \\ 0/1 & \beta \leq \beta_{start} \end{cases} \tag{A.23}$$

Both move limits are applied starting form the value β_{start}.

A.6 Density Behavior of Optimization Terms

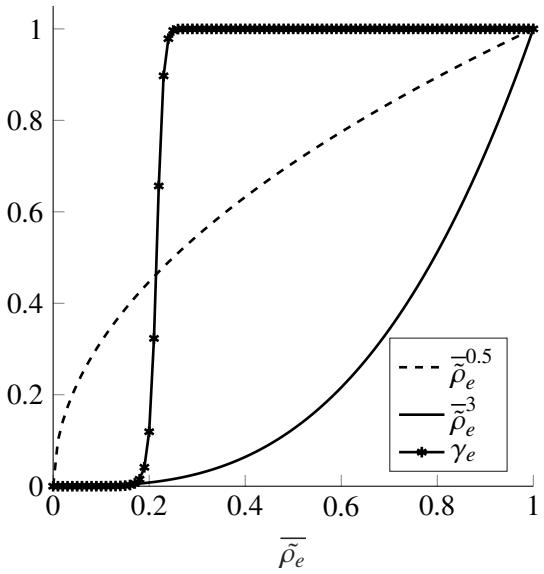

Figure A.5: Distributions of γ_e, $\overline{\tilde{\rho}}_e^3$ and $\overline{\tilde{\rho}}_e^{0.5}$ over the densities $\overline{\tilde{\rho}}_e$

The SIMP term $\overline{\tilde{\rho}}_e^3$, the step of the energy interpolation parameter γ_e and the term $\overline{\tilde{\rho}}_e^{0.5}$ representing the stress relaxation parameter all have different behaviors with respect to the element densities. Figure A.5 illustrates this. Strong interaction effects between the relation among these distributions and the optimization results are observed.